



NAVAL POSTGRADUATE SCHOOL

MONTEREY, CALIFORNIA

THESIS

**ANALYSIS OF TROPICAL CYCLONE INITIALIZATION
IN COAMPS-TC FOR HURRICANE PATRICIA (2015)
UTILIZING TCI EXPERIMENT DATASETS**

by

Kevin I. Breach

June 2017

Thesis Advisor:
Second Reader:

Eric Hendricks
Russell Elsberry

Approved for public release. Distribution is unlimited.

THIS PAGE INTENTIONALLY LEFT BLANK

REPORT DOCUMENTATION PAGE			<i>Form Approved OMB No. 0704-0188</i>	
Public reporting burden for this collection of information is estimated to average 1 hour per response, including the time for reviewing instruction, searching existing data sources, gathering and maintaining the data needed, and completing and reviewing the collection of information. Send comments regarding this burden estimate or any other aspect of this collection of information, including suggestions for reducing this burden, to Washington headquarters Services, Directorate for Information Operations and Reports, 1215 Jefferson Davis Highway, Suite 1204, Arlington, VA 22202-4302, and to the Office of Management and Budget, Paperwork Reduction Project (0704-0188) Washington DC 20503.				
1. AGENCY USE ONLY (Leave blank)		2. REPORT DATE June 2017		3. REPORT TYPE AND DATES COVERED Master's thesis
4. TITLE AND SUBTITLE ANALYSIS OF TROPICAL CYCLONE INITIALIZATION IN COAMPS-TC FOR HURRICANE PATRICIA (2015) UTILIZING TCI EXPERIMENT DATASETS			5. FUNDING NUMBERS	
6. AUTHOR(S) Kevin I. Breach				
7. PERFORMING ORGANIZATION NAME(S) AND ADDRESS(ES) Naval Postgraduate School Monterey, CA 93943-5000			8. PERFORMING ORGANIZATION REPORT NUMBER	
9. SPONSORING /MONITORING AGENCY NAME(S) AND ADDRESS(ES) N/A			10. SPONSORING / MONITORING AGENCY REPORT NUMBER	
11. SUPPLEMENTARY NOTES The views expressed in this thesis are those of the author and do not reflect the official policy or position of the Department of Defense or the U.S. Government. IRB number ____N/A____.				
12a. DISTRIBUTION / AVAILABILITY STATEMENT Approved for public release. Distribution is unlimited.			12b. DISTRIBUTION CODE A	
13. ABSTRACT (maximum 200 words) <p>From 21 to 23 October 2015, Eastern Pacific Hurricane Patricia underwent a period of extreme rapid intensification that both hurricane specialists and numerical weather prediction (NWP) models failed to predict, including the Navy operational model for hurricane prediction, the Coupled Ocean/Atmosphere Mesoscale Prediction System for Tropical Cyclones (COAMPS-TC). Fortunately, the Office of Naval Research (ONR)-funded Tropical Cyclone Intensity (TCI) initiative collected high spatial resolution in-situ and remotely sensed data during Patricia's rapid intensification.</p> <p>In order to understand the relationship between initial conditions and subsequent intensity forecast errors, this study utilizes these datasets to validate the initial conditions in the multiply-nested COAMPS-TC model at three synoptic times and finds three main conclusions. First, the structure of the outflow layer in the COAMPS-TC initial conditions at 1800 UTC 22 and 23 October did not include an observed equatorward outflow jet. Second, the maximum winds of the COAMPS-TC model vortex at 1800 UTC 21 October were too weak. Finally, the initial vortex in the COAMPS-TC model at 1800 UTC 22 October had a radius of maximum winds that was too large, a warm core too low in elevation, and an outer circulation where the winds were too strong. While other factors may have contributed to the intensity forecast errors for Patricia, this study indicates it is likely that the initial condition errors contributed significantly, and illustrates the need for sophisticated data assimilation systems that can ingest high-density observations in order to improve TC intensity forecasting.</p>				
14. SUBJECT TERMS tropical cyclone, hurricane, Patricia, Eastern Pacific, TCI, COAMPS-TC, CTCX, initialization, NHC, National Hurricane Center, HDSS, dropsonde			15. NUMBER OF PAGES 143	
			16. PRICE CODE	
17. SECURITY CLASSIFICATION OF REPORT Unclassified	18. SECURITY CLASSIFICATION OF THIS PAGE Unclassified	19. SECURITY CLASSIFICATION OF ABSTRACT Unclassified	20. LIMITATION OF ABSTRACT UU	

THIS PAGE INTENTIONALLY LEFT BLANK

Approved for public release. Distribution is unlimited.

**ANALYSIS OF TROPICAL CYCLONE INITIALIZATION IN COAMPS-TC
FOR HURRICANE PATRICIA (2015) UTILIZING TCI EXPERIMENT
DATASETS**

Kevin I. Breach
Lieutenant, United States Navy
B.S., United States Naval Academy, 2008

Submitted in partial fulfillment of the
requirements for the degree of

**MASTER OF SCIENCE IN METEOROLOGY AND
PHYSICAL OCEANOGRAPHY**

from the

**NAVAL POSTGRADUATE SCHOOL
June 2017**

Approved by: Eric Hendricks
Thesis Advisor

Russell Elsberry
Second Reader

Wendell A. Nuss
Chair, Department of Meteorology

THIS PAGE INTENTIONALLY LEFT BLANK

ABSTRACT

From 21 to 23 October 2015, Eastern Pacific Hurricane Patricia underwent a period of extreme rapid intensification that both hurricane specialists and numerical weather prediction (NWP) models failed to predict, including the Navy operational model for hurricane prediction, the Coupled Ocean/Atmosphere Mesoscale Prediction System for Tropical Cyclones (COAMPS-TC). Fortunately, the Office of Naval Research (ONR)–funded Tropical Cyclone Intensity (TCI) initiative collected high spatial resolution in-situ and remotely sensed data during Patricia’s rapid intensification.

In order to understand the relationship between initial conditions and subsequent intensity forecast errors, this study utilizes these datasets to validate the initial conditions in the multiply-nested COAMPS-TC model at three synoptic times and finds three main conclusions. First, the structure of the outflow layer in the COAMPS-TC initial conditions at 1800 UTC 22 and 23 October did not include an observed equatorward outflow jet. Second, the maximum winds of the COAMPS-TC model vortex at 1800 UTC 21 October were too weak. Finally, the initial vortex in the COAMPS-TC model at 1800 UTC 22 October had a radius of maximum winds that was too large, a warm core too low in elevation, and an outer circulation where the winds were too strong. While other factors may have contributed to the intensity forecast errors for Patricia, this study indicates it is likely that the initial condition errors contributed significantly, and illustrates the need for sophisticated data assimilation systems that can ingest high-density observations in order to improve TC intensity forecasting.

THIS PAGE INTENTIONALLY LEFT BLANK

TABLE OF CONTENTS

I.	INTRODUCTION.....	1
A.	LACK OF OBSERVATIONAL DATA FOR MIDDLE AND UPPER LEVELS OF TROPICAL CYCLONES.....	2
B.	COAMPS-TC MODEL INITIALIZATION TECHNIQUE.....	3
C.	THESIS OUTLINE.....	4
II.	BACKGROUND	5
A.	SYNOPTIC EVOLUTION OF HURRICANE PATRICIA	5
B.	OBSERVED TRACK AND INTENSITY	9
C.	DEVELOPMENT OF OUTFLOW JETS	10
D.	COAMPS-TC MODEL PERFORMANCE DURING INTENSIFICATION	15
III.	DATA AND METHODOLOGY	19
A.	DATASETS	19
1.	COAMPS-TC (CTCX) Model Data	19
2.	Office of Naval Research (ONR) Tropical Cyclone Intensity (TCI) Initiative	19
3.	Satellite Data.....	22
4.	Aircraft Reconnaissance Data	22
B.	METHODOLOGY	22
1.	Zero-Wind Center (ZWC) Method for Acquiring Wind Vectors in Storm-Relative Coordinate System.....	22
2.	Determining Differences in TC Structure between COAMPS-TC Initial Conditions and Observations	24
IV.	RESULTS	27
A.	HDSS DROPSONDE DRIFT	27
B.	WIND SPEED COMPARISONS	31
1.	Near-surface Wind Field Structure.....	31
2.	Outflow Wind Field Structure.....	34
3.	Storm-Relative Wind	37
C.	GEOPOTENTIAL HEIGHT	61
1.	21 October 2015.....	63
2.	22 October 2015.....	70
3.	23 October 2015.....	76
D.	POTENTIAL TEMPERATURE AND WARM CORE STRUCTURE.....	82

1.	21 October 2015.....	82
2.	22 October 2015.....	89
3.	23 October 2015.....	97
E.	ERROR SUMMARY AND ANALYSIS	104
1.	Inner Core Region.....	104
2.	Outer Region	106
V.	SUMMARY AND RECOMMENDATIONS.....	109
A.	SUMMARY OF HURRICANE PATRICIA AS OBSERVED BY HDSS	109
B.	CONCLUSIONS AND RECOMMENDATIONS.....	109
C.	AREAS FOR FUTURE RESEARCH.....	111
	LIST OF REFERENCES	113
	INITIAL DISTRIBUTION LIST	117

LIST OF FIGURES

Figure 1.	Equation for the modified Rankine wind profile. Source: Stern and Nolan (2011), Liou and Sashegyi (2012).....	4
Figure 2.	Composite infrared satellite image of Tropical Storm Patricia (20E) at 1145 UTC 21 Oct 2015. Source: Naval Research Laboratory (NRL; 2017).....	6
Figure 3.	Combination of a 85GHz microwave satellite image (K, color scale at bottom) at 0850 UTC 22 October on the left side and an infrared satellite image at 0830 UTC 22 October on the right side. Source: NRL (2017).....	7
Figure 4.	Visible satellite image of Hurricane Patricia at 1500 UTC 23 October near time of maximum intensity. Source: NRL (2017).	8
Figure 5.	Track of Hurricane Patricia. Source: Kimberlain et al. (2016).....	9
Figure 6.	Various sources for intensity estimates (see inset) for Hurricane Patricia between 20–24 October 2015 and the NHC best track intensities (black line). Source: Kimberlain et al. (2016).	10
Figure 7.	Schematic of the streamlines (thin lines) and outflow jets (thick lines) for intensifying TCs (top) and non-intensifying TCs (bottom). Source: Merrill (1988).	11
Figure 8.	Infrared satellite imagery and AMVs at 1800 UTC 21 October 2015. Source: Cooperative Institute for Meteorological Satellite Studies (CIMSS; 2017).....	12
Figure 9.	Infrared satellite imagery and AMVs as in Figure 7, except for 1800 UTC 22 October 2015. Source: CIMSS (2017).....	13
Figure 10.	Infrared satellite imagery and AMVs as in Figure 7, except for 1800 UTC 23 October 2015. Source: CIMSS (2017).....	14
Figure 11.	Validation of the intensity forecasts from 1800 UTC 21 October for Patricia by various intensity products (inset) versus the NHC best track intensity (thin black line). Source: Fleet Numerical Meteorology and Oceanography Center (FNMOC; courtesy of Raymond Lee).....	15
Figure 12.	Validation of intensity forecasts as in Figure 10, except for 1800 UTC 22 October. Source: FNMOC (courtesy of Raymond Lee).	16

Figure 13.	Validation of intensity forecasts as in Figure 10 and 11, except for 1800 UTC 23 October. Source: FNMOC (courtesy of Raymond Lee)	17
Figure 14.	View of the Automated Dropsonde Dispenser (ADD) aboard the NASA WB-57 aircraft flying over outflow region of Tropical Storm Patricia. Source: Doyle et al. (2017).....	21
Figure 15.	Schematic of the Willoughby and Chelmow (1982) technique for locating a TC center from the changing flight-level wind directions as the aircraft flies near the center. Source: Creasey and Elsberry (2017).....	23
Figure 16.	Vortex tilt of Hurricane Joaquin (2015) based on ZWCs each kilometer from 9.5 km to 1.5 km (large red dots) derived from HDSS wind vector directions. Source: Creasey and Elsberry (2017).....	24
Figure 17.	Example of HDSS storm-relative correction at 500 mb for 1800 UTC 23 October 2015.....	25
Figure 18.	Error equations used in this study	26
Figure 19.	Southwest to northwest flight track of the NASA WB-57 through the center of Hurricane Patricia at approximately 1800 UTC 23 October	28
Figure 20.	HDSS-observed wind speeds (color scale on right) as a function of distance from Patricia's zero-wind center (ZWC) at approximately 1800 UTC 23 October.....	29
Figure 21.	NASA WB-57 flight path (yellow line) overlaid on GOES enhanced infrared image of Patricia at 1830 UTC 21 October. Source: TCI; Doyle et al. (2017).	30
Figure 22.	NASA WB-57 flight path as in Figure 19, except at 1815 UTC 22 October.....	30
Figure 23.	NASA WB-57 flight path as in Figure 19, except at 2015 UTC 23 October.....	31
Figure 24.	Wind speed at 10 m elevation in the CTCX initial conditions at 1800 UTC 21 October and surface wind speed from the HIRAD analysis of Patricia at 1945 UTC 21 October	32
Figure 25.	Wind speed at 10 m elevation in the CTCX initial conditions at 1800 UTC 22 October and surface wind speed from the HIRAD analysis of Patricia at 1924 UTC 21 October	33

Figure 26.	Wind speed at 10 m elevation in the CTCX initial conditions at 1800 UTC 23 October and surface wind speed from the HIRAD analysis of Patricia at 2025 UTC 23 October	34
Figure 27.	CTCX wind (kt) at 250 mb (left) and upper-level Atmospheric Motion Vectors (AMVs, kt) overlaid on an infrared satellite image (right) at 1800 UTC 21 October. Right panel source: CIMSS (2017).....	35
Figure 28.	CTCX wind at 250 mb (left) and AMVs (right) at 1800 UTC 22 October. Right panel source: CIMSS (2017).....	36
Figure 29.	CTCX wind at 250 mb (left) and AMVs (right) at 1800 UTC 23 October. Right pane source: CIMSS (2017).....	37
Figure 30.	Storm-relative wind speeds from HDSS (blue dots) and CTCX initial conditions (red dots) as a function of distance to Patricia’s zero-wind center (ZWC) at 200 mb for 1800 UTC 21 October.....	39
Figure 31.	CTCX mean wind speed bias relative to the HDSS wind speeds averaged in 10 km radial bands at 200 mb for 1800 UTC 21 October	39
Figure 32.	Storm-relative wind speeds as in Figure 30 except at 300 mb for 1800 UTC 21 October.....	40
Figure 33.	CTCX mean wind speed bias as in Figure 31 except at 300mb for 1800 UTC 21 October.....	40
Figure 34.	Storm-relative wind speeds as in Figure 30 except at 500 mb for 1800 UTC 21 October.....	41
Figure 35.	CTCX mean wind speed bias as in Figure 31 except at 500 mb for 1800 UTC 21 October.....	41
Figure 36.	Storm-relative wind speeds as in Figure 30 except at 700 mb for 1800 UTC 21 October.....	42
Figure 37.	CTCX mean wind speed bias as in Figure 31 except at 700 mb for 1800 UTC 21 October.....	42
Figure 38.	Storm-relative wind speeds as in Figure 30 except at 850 mb for 1800 UTC 21 October.....	43
Figure 39.	CTCX mean wind speed bias as in Figure 31 except at 850 mb for 1800 UTC 21 October.....	43
Figure 40.	Storm-relative wind speeds as in Figure 30 except at 200 mb for 1800 UTC 22 October.....	45

Figure 41.	CTCX mean wind speed bias as in Figure 31 except at 200 mb for 1800 UTC 22 October.....	45
Figure 42.	Storm-relative wind speeds as in Figure 30 except at 300 mb for 1800 UTC 22 October.....	46
Figure 43.	CTCX mean wind speed bias as in Figure 31 except at 300 mb for 1800 UTC 22 October.....	46
Figure 44.	Storm-relative wind speeds as in Figure 30 except at 500 mb for 1800 UTC 22 October.....	47
Figure 45.	CTCX mean wind speed bias as in Figure 31 except at 500 mb for 1800 UTC 22 October.....	47
Figure 46.	Storm-relative wind speeds as in Figure 30 except at 700 mb for 1800 UTC 22 October.....	48
Figure 47.	CTCX mean wind speed bias as in Figure 31 except at 700 mb for 1800 UTC 22 October.....	48
Figure 48.	Storm-relative wind speeds as in Figure 30 except at 700 mb for 1800 UTC 22 October (zoomed to display only the inner 90 km)	49
Figure 49.	Storm-relative wind speeds as in Figure 30 except at 850 mb for 1800 UTC 22 October.....	50
Figure 50.	CTCX mean wind speed bias as in Figure 31 except at 850 mb for 1800 UTC 22 October.....	50
Figure 51.	CTCX (left panel) storm-relative winds at 1800 UTC 22 October and HDSS (right panel) storm-relative winds from 1815–1828 UTC 22 October.....	52
Figure 52.	Storm-relative wind speeds as in Figure 30 except at 200 mb for 1800 UTC 23 October.....	54
Figure 53.	CTCX mean wind speed bias as in Figure 31 except at 200 mb for 1800 UTC 23 October.....	54
Figure 54.	Storm-relative wind speeds as in Figure 30 except at 300 mb for 1800 UTC 23 October.....	55
Figure 55.	CTCX mean wind speed bias as in Figure 31 except at 300 mb for 1800 UTC 23 October.....	55

Figure 56.	Storm-relative wind speeds as in Figure 30 except at 500 mb for 1800 UTC 23 October.....	56
Figure 57.	CTCX mean wind speed bias as in Figure 31 except at 500 mb for 1800 UTC 23 October.....	56
Figure 58.	Storm-relative wind speeds as in Figure 30 except at 700 mb for 1800 UTC 23 October.....	57
Figure 59.	CTCX mean wind speed bias as in Figure 31 except at 700 mb for 1800 UTC 23 October.....	57
Figure 60.	Storm-relative wind speeds as in Figure 30 except at 700 mb for 1800 UTC 23 October (zoomed to display only the inner 90 km)	58
Figure 61.	Storm-relative wind speeds as in Figure 30 except at 850 mb for 1800 UTC 23 October.....	59
Figure 62.	CTCX mean wind speed bias as in Figure 31 except at 850 mb for 1800 UTC 23 October.....	59
Figure 63.	Equations used in the geopotential height and potential temperature balance studies. Source: Hendricks and Peng (2012).	62
Figure 64.	Geopotential heights from HDSS (blue dots) and CTCX initial conditions (red dots) as a function of distance to Patricia’s zero-wind center (ZWC) at 200 mb for 1800 UTC 21 October.....	64
Figure 65.	CTCX mean geopotential height bias relative to HDSS observations averaged in 10 km radial bands at 200 mb for 1800 UTC 21 October	64
Figure 66.	Geopotential heights as in Figure 64 except at 300 mb for 1800 UTC 21 October.....	65
Figure 67.	CTCX mean geopotential height bias as in Figure 65 except at 300 mb for 1800 UTC 21 October.....	65
Figure 68.	Geopotential heights as in Figure 64 except at 500 mb for 1800 UTC 21 October.....	66
Figure 69.	CTCX mean geopotential height bias as in Figure 65 except at 500 mb for 1800 UTC 21 October.....	66
Figure 70.	Geopotential heights as in Figure 64 except at 700 mb for 1800 UTC 21 October.....	67

Figure 71.	CTCX mean geopotential height bias as in Figure 65 except at 700 mb for 1800 UTC 21 October.....	67
Figure 72.	Geopotential heights as in Figure 64 except at 850 mb for 1800 UTC 21 October.....	68
Figure 73.	CTCX mean geopotential height bias as in Figure 65 except at 850 mb for 1800 UTC 21 October.....	68
Figure 74.	Geopotential heights as in Figure 64 except at 200 mb for 1800 UTC 22 October.....	71
Figure 75.	CTCX mean geopotential height bias as in Figure 65 except at 200 mb for 1800 UTC 22 October.....	71
Figure 76.	Geopotential heights as in Figure 64 except at 300 mb for 1800 UTC 22 October.....	72
Figure 77.	CTCX mean geopotential height bias as in Figure 65 except at 300 mb for 1800 UTC 22 October.....	72
Figure 78.	Geopotential heights as in Figure 64 except at 500 mb for 1800 UTC 22 October.....	73
Figure 79.	CTCX mean geopotential height bias as in Figure 65 except at 500 mb for 1800 UTC 22 October.....	73
Figure 80.	Geopotential heights as in Figure 64 except at 700 mb for 1800 UTC 22 October.....	74
Figure 81.	CTCX mean geopotential height bias as in Figure 65 except at 700 mb for 1800 UTC 22 October.....	74
Figure 82.	Geopotential heights as in Figure 64 except at 850 mb for 1800 UTC 22 October.....	75
Figure 83.	CTCX mean geopotential height bias as in Figure 65 except at 850 mb for 1800 UTC 22 October.....	75
Figure 84.	Geopotential heights as in Figure 64 except at 200 mb for 1800 UTC 23 October.....	77
Figure 85.	CTCX mean geopotential height bias as in Figure 65 except at 200 mb for 1800 UTC 23 October.....	77
Figure 86.	Geopotential heights as in Figure 64 except at 300 mb for 1800 UTC 23 October.....	78

Figure 87.	CTCX mean geopotential height bias as in Figure 65 except at 300 mb for 1800 UTC 23 October.....	78
Figure 88.	Geopotential heights as in Figure 64 except at 500 mb for 1800 UTC 23 October.....	79
Figure 89.	CTCX mean geopotential height bias as in Figure 65 except at 500 mb for 1800 UTC 23 October.....	79
Figure 90.	Geopotential heights as in Figure 64 except at 700 mb for 1800 UTC 23 October.....	80
Figure 91.	CTCX mean geopotential height bias as in Figure 65 except at 700 mb for 1800 UTC 23 October.....	80
Figure 92.	Geopotential heights as in Figure 64 except at 850 mb for 1800 UTC 23 October.....	81
Figure 93.	CTCX mean geopotential height bias as in Figure 65 except at 850 mb for 1800 UTC 23 October.....	81
Figure 94.	Standard Poisson equation for potential temperature $\theta(z)$ in K. Source: University of Washington (www.atmos.washington.edu).....	82
Figure 95.	Potential temperatures (K) from HDSS (blue dots) and CTCX initial conditions (red dots) as a function of distance from the zero-wind center (ZWC) at 200 mb for 1800 UTC 21 October.....	83
Figure 96.	CTCX mean potential temperature bias relative to HDSS observations averaged in 10 km radial bands at 200 mb for 1800 UTC 21 October.....	83
Figure 97.	Potential temperatures as in Figure 95 except at 300 mb for 1800 UTC 21 October.....	84
Figure 98.	CTCX mean potential temperature bias as in Figure 96 except at 300 mb for 1800 UTC 21 October.....	84
Figure 99.	Potential temperatures as in Figure 95 except at 500 mb for 1800 UTC 21 October.....	85
Figure 100.	CTCX mean potential temperature bias as in Figure 96 except at 500 mb for 1800 UTC 21 October.....	85
Figure 101.	Potential temperatures as in Figure 95 except at 700 mb for 1800 UTC 21 October.....	86

Figure 102.	CTCX mean potential temperature bias as in Figure 96 except at 700 mb for 1800 UTC 21 October.....	86
Figure 103.	Potential temperatures as in Figure 95 except at 850 mb for 1800 UTC 21 October.....	87
Figure 104.	CTCX mean potential temperature bias as in Figure 96 except at 850 mb for 1800 UTC 21 October.....	87
Figure 105.	Potential temperatures as in Figure 95 except at 200 mb for 1800 UTC 22 October.....	90
Figure 106.	CTCX mean potential temperature bias as in Figure 96 except at 200 mb for 1800 UTC 22 October.....	90
Figure 107.	Potential temperatures as in Figure 95 except at 300 mb for 1800 UTC 22 October.....	91
Figure 108.	CTCX mean potential temperature bias as in Figure 96 except at 300 mb for 1800 UTC 22 October.....	91
Figure 109.	Potential temperatures as in Figure 95 except at 500 mb for 1800 UTC 22 October.....	92
Figure 110.	CTCX mean potential temperature bias as in Figure 96 except at 500 mb for 1800 UTC 22 October.....	92
Figure 111.	Potential temperatures as in Figure 95 except at 700 mb for 1800 UTC 22 October.....	93
Figure 112.	CTCX mean potential temperature bias as in Figure 96 except at 700 mb for 1800 UTC 22 October.....	93
Figure 113.	Potential temperatures in Figure 95 except at 700 mb for 1800 UTC 22 October (zoomed to display only the inner 90 km)	94
Figure 114.	Potential temperatures as in Figure 95 except at 850 mb for 1800 UTC 22 October.....	95
Figure 115.	CTCX mean potential temperature bias as in Figure 96 except at 850 mb for 1800 UTC 22 October.....	95
Figure 116.	Potential temperatures as in Figure 95 except at 200 mb for 1800 UTC 23 October.....	98
Figure 117.	CTCX mean potential temperature bias as in Figure 96 except at 200 mb for 1800 UTC 23 October.....	98

Figure 118.	Potential temperatures as in Figure 95 except at 300 mb for 1800 UTC 23 October.....	99
Figure 119.	CTCX mean potential temperature bias as in Figure 96 except at 300 mb for 1800 UTC 23 October.....	99
Figure 120.	Potential temperatures as in Figure 95 except at 500 mb for 1800 UTC 23 October.....	100
Figure 121.	CTCX mean potential temperature bias as in Figure 96 except at 500 mb for 1800 UTC 23 October.....	100
Figure 122.	Potential temperatures as in Figure 95 except at 700 mb for 1800 UTC 23 October.....	101
Figure 123.	CTCX mean potential temperature bias as in Figure 96 except at 700 mb for 1800 UTC 23 October.....	101
Figure 124.	Potential temperatures as in Figure 95 except at 700 mb for 1800 UTC 23 October (zoomed to display only the inner 90 km)	102
Figure 125.	Potential temperatures as in Figure 95 except at 850 mb for 1800 UTC 23 October.....	102
Figure 126.	CTCX mean potential temperature bias as in Figure 96 except at 850 mb for 1800 UTC 23 October.....	103

THIS PAGE INTENTIONALLY LEFT BLANK

LIST OF TABLES

Table 1.	Expendable Digital Dropsonde (XDD) sensor specifications, including range, accuracy, and resolution. Adapted from Black et al. (2017).....	21
Table 2.	Inner 160 km CTCX error summary for 1800 UTC 21 October	104
Table 3.	Inner 60 km CTCX error summary for 1800 UTC 22 October	105
Table 4.	Inner 30 km CTCX error summary for 1800 UTC 23 October	105
Table 5.	CTCX error summary outside of a 160 km radius for 1800 UTC 21 October.....	106
Table 6.	CTCX error summary outside of a 60 km radius for 1800 UTC 22 October.....	106
Table 7.	CTCX error summary outside of a 30 km radius for 1800 UTC 23 October.....	106

THIS PAGE INTENTIONALLY LEFT BLANK

LIST OF ACRONYMS AND ABBREVIATIONS

ADD	Automated Dropsonde Dispenser
AMV	Atmospheric Motion Vector
COAMPS-TC	Coupled Ocean/Atmosphere Mesoscale Prediction System for Tropical Cyclones (also referred to as CTCX when initialized using the GFS)
FNMOC	Fleet Numerical Meteorology and Oceanography Center
GFS	Global Forecasting System
GOES	Geostationary Operational Environmental Satellite
GPS	Global Positioning System
HDSS	High Definition Sounding System
HIRAD	Hurricane Imaging Radiometer
HS3	Hurricane and Severe Storm Sentinel
JTWC	Joint Typhoon Warning Center
MAE	Mean Absolute Error
ME	Mean Error
MEMS	Microelectromechanical System
MJO	Madden-Julian Oscillation
MSFC	Marshall Space Flight Center
NASA	National Aeronautics and Space Administration
NAVGEN	Navy Global Environmental Model
NCEP	National Centers for Environmental Prediction
NHC	National Hurricane Center
NOAA	National Oceanic and Atmospheric Association
NRL	Naval Research Laboratory
NWP	Numerical Weather Prediction
ONR	Office of Naval Research
RMSE	Root Mean Square Error
RMW	Radius of Maximum Winds
SFMR	Stepped Frequency Microwave Radiometer
SST	Sea Surface Temperature

TC	Tropical Cyclone
TCI	Tropical Cyclone Intensity
USDOC	United States Department Of Commerce
USN	United States Navy
UTC	Coordinated Universal Time, also referred to as Zulu Time (Z)
XDD	Expendable Digital Dropsondes
ZWC	Zero-Wind Center

ACKNOWLEDGMENTS

First, I acknowledge Dr. Eric Hendricks and Dr. Russell Elsberry for their guidance and valuable insight during this effort. Additionally, this study would not have been possible without the considerable amount of data preparation performed by Robert Creasey and Mary S. Jordan. I also acknowledge the NASA WB-57 and NOAA reconnaissance mission flight crews, James Doyle and Richard Hodur of NRL for providing the CTCX datasets, Raymond Lee of FNMOC for providing Figures 11–13, and the ONR-funded TCI project for providing the HDSS and HIRAD data.

THIS PAGE INTENTIONALLY LEFT BLANK

I. INTRODUCTION

Tropical cyclone (TC) intensification has been a challenge for researchers, forecasters, and numerical weather prediction (NWP) models for decades. Advances in observations, model physics, computing power and model resolution have led to a marked improvement in TC track forecasts, but significantly less improvement in TC intensity forecasts (Rogers et al., 2006). This lack of improvement is due to limited observations and understanding of internal small-scale dynamical processes (Hendricks et al., 2010), as well as limited understanding of the interaction of TCs with their environment (Halverson et al., 2007). Many of the internal processes such as cloud microphysics and air-sea interactions are represented in NWP models by empirically-derived parameterizations (Wang, 2002). Furthermore, there are even competing theories as to the mechanisms by which a TC intensifies (Montgomery and Smith, 2014). Consequently, more observations and more research are necessary to advance TC intensity understanding and forecasting.

Eastern Pacific Hurricane Patricia (2015) was the most intense TC ever recorded in the Western Hemisphere in terms of both minimum central pressure and maximum sustained surface winds (Rogers et al., 2017). Patricia underwent a period of extreme rapid intensification from the morning of 21 October until the morning of 23 October, where the maximum sustained surface winds increased a total of 150 kt (77.2 m/s) from 35 kt (18.0 m/s) to 185 kt (95.2 m/s) over a two-day period (Kimberlain et al., 2016, Rogers et al., 2017). This vastly exceeds the rapid intensification definition of 30 kt (15.4 m/s) in a 24-hr period by Kaplan and DeMaria (2003). During this period every major operational deterministic NWP model severely under-forecast the storm's strengthening winds (Kimberlain et al., 2016). Accurate TC intensity prediction by NWP models depends on many factors, including accurate model initialization, high horizontal and vertical resolution, and physical parameterizations that accurately represent reality. While any of these and other factors could have contributed to an under-forecast of Patricia's intensity, this thesis will explore the contribution of initial condition errors to the Patricia intensity forecast errors.

A. LACK OF OBSERVATIONAL DATA FOR MIDDLE AND UPPER LEVELS OF TROPICAL CYCLONES

The observational system for TCs consists of satellite imagery, land-based radar systems, ocean buoys, and aircraft reconnaissance including flight-level measurements, Doppler radar, and dropsondes (United States Department of Commerce [USDOC], 2017). Reconnaissance aircraft can also measure rain rate and extrapolate surface winds using a stepped frequency microwave radiometer (SFMR; Uhlhorn et al., 2007). According to the USDOC, all of the current observing methods other than satellite imagery are only observing at or below flight level, and even the flight-level requirement for dropsonde deployment is as low as 19,000 ft (5,791.2 m). While satellite microwave imagery at certain frequencies has proven useful in determining the upper-level structure of a TC, it is limited by signal attenuation due to precipitation, and these polar-orbiting satellites provide a limited number of observations compared to geostationary satellites (Brueske and Velden, 2002). Therefore, information about the middle and upper layers of TCs is extremely scarce compared to the amount of data available in the lower levels. Efforts have been made in recent years to rectify the disparity, such as the National Oceanic and Atmospheric Association's (NOAA) Gulfstream-IV high altitude missions up to 13–14 km (Rogers et al., 2001) and the National Aeronautics and Space Administration (NASA) Hurricane and Severe Storm Sentinel (HS3) field campaign using the unmanned Global Hawk aircraft to deploy up to eight dropsondes at a time from the lower stratosphere (Braun et al., 2016; Komaromi and Doyle, 2016). The NASA WB-57 aircraft equipped with the High Definition Sounding System (HDSS) dropsondes flew over Hurricane Patricia and other TCs as part of the Office of Naval Research (ONR) Tropical Cyclone Intensity (TCI) experiment in 2015 (Doyle et al., 2017). The advantage of the HDSS over the dropsonde system used in HS3 is the ability to have forty dropsondes in the air at one time instead of only eight, which allowed for high spatial density (every 4 km) observations (Black et al., 2015) during center over-passes through Patricia. These HDSS datasets collected in Hurricane Patricia are essential for examining the accuracy of model initialization for this historic storm.

B. COAMPS-TC MODEL INITIALIZATION TECHNIQUE

Due to the insufficient reconnaissance or research aircraft observations for many TCs, adding a bogus vortex from the official analysis to a background initial NWP model field is a common practice for initializing regional tropical models. The United States Navy (USN) operational model for TC prediction is the Coupled Ocean/Atmosphere Mesoscale Prediction System – Tropical Cyclones (COAMPS-TC, Doyle et al., 2014). The COAMPS-TC version used here is the real-time experimental version CTCX, which uses the National Centers for Environmental Prediction (NCEP) Global Forecasting System (GFS) initial and lateral boundary conditions for its initial conditions before adding a bogus vortex which is based on the official National Hurricane Center (NHC) or Joint Typhoon Warning Center (JTWC) TC analysis (e.g., www.nhc.noaa.gov/modelsummary.shtml for NHC). This is contrasted with the operational version COTC which uses the Navy Global Environmental Model (NAVGEM) initial and lateral boundary conditions. For Hurricane Patricia, NHC provided the storm center position, estimated minimum central pressure, storm motion, maximum surface winds, extent of 12 ft (3.66 m) seas, and wind radii (www.nhc.gov/tcm_example.shtml). A balanced bogus vortex derived from the NHC-analyzed storm motion, maximum winds, and radius of 34 kt (17.5 m/s) winds is directly inserted at the TC center position (Doyle et al., 2015). In order to assemble the bogus vortex, first the tangential wind field is constructed based upon a modified Rankine vortex (Figure 1) fit to the NHC-analyzed storm parameters. Next, the vertical structure is prescribed. Here the winds increase from 20% to 40% from the surface to 1 km height, then linearly decrease to 0.0 at 8 km for storms with maximum winds less than 45 kt (23.15 m/s) and up to 13.5 km for storms stronger than 100 kt (51.44 m/s). For storms between 45 and 100 kt, the height of the storm increases linearly from 8 km to 13.5 km (Richard Hodur, personal communication, 2017).

$$v = \begin{cases} \varphi v_{max} \left(\frac{r}{R_{v\ max}} \right), & r \leq R_{v\ max} \\ \varphi v_{max} \left(\frac{R_{v\ max}}{r} \right)^\alpha, & r > R_{v\ max} \end{cases}$$

v is the wind speed at radius r , φ is the vertical wind shear factor, v_{max} is the maximum wind speed, $R_{v\ max}$ is the radius of maximum wind (RMW), and α is the wind speed attenuation rate outside the RMW.

Figure 1. Equation for the modified Rankine wind profile. Source: Stern and Nolan (2011), Liou and Sashegyi (2012).

Then the mass field is obtained by solving the nonlinear and hydrostatic balance equations. (Doyle et al., 2014). Finally this vortex is inserted into the environment on the three nested COAMPS-TC grids at the warning center estimate of the TC position.

C. THESIS OUTLINE

The hypothesis for this study is that disparities between reality and the structure of the bogus vortex inserted into CTCX for Hurricane Patricia had a substantial impact on the model's ability to predict the extreme rapid intensification that occurred. Leroux et al. (2012) found even small differences in TC structure may contribute to large variations in TC intensity. The rest of this thesis is organized as follows.

The synoptic background on Hurricane Patricia and the challenge for predicting its extremely rapid intensification are described in Chapter II. The data and methodology for comparing the CTCX initial model structure with the TCI observations will be presented in Chapter III. The validation of the CTCX initial conditions with the TCI datasets is given in Chapter IV and the main conclusions and recommendations are given in Chapter V.

II. BACKGROUND

A. SYNOPTIC EVOLUTION OF HURRICANE PATRICIA

From 15 to 17 October 2015, multiple synoptic events came together to generate an area of deep convection south of the Gulf of Tehuantepec in the eastern North Pacific, which included two minor easterly waves crossing Central America into the Pacific and converging, a Tehuantepec gap wind event, and the passage of a strong Madden-Julian Oscillation (MJO). A second gap wind event occurred on 18 October, which initially weakened the deep convection in the system. However, the system reformed on the cyclonic shear side of the gap winds on 19 October, which actually assisted in organizing the system into a more well-defined circulation. The system was officially designated as Tropical Depression 20E at 1500 UTC 20 October, and at the time was forecast to reach an intensity of 85 kt (43.7 m/s) three days later. Since 20E was located south of a mid-level ridge that extended into the eastern Pacific from the Gulf of Mexico, the depression drifted west-southwest over slightly cooler water and into an environment of slightly drier air, which slowed its development. Early on 21 October (Figure 2) the system began to move around the periphery of the ridge on a more west-northwest trajectory into an area of higher moisture and smaller vertical wind shear. An abrupt increase in cloud organization was noted from satellite imagery and a U.S. Air Force aircraft reconnaissance mission confirmed that winds had strengthened to 50 kt (25.7 m/s). Depression 20E was then designated Tropical Storm Patricia.

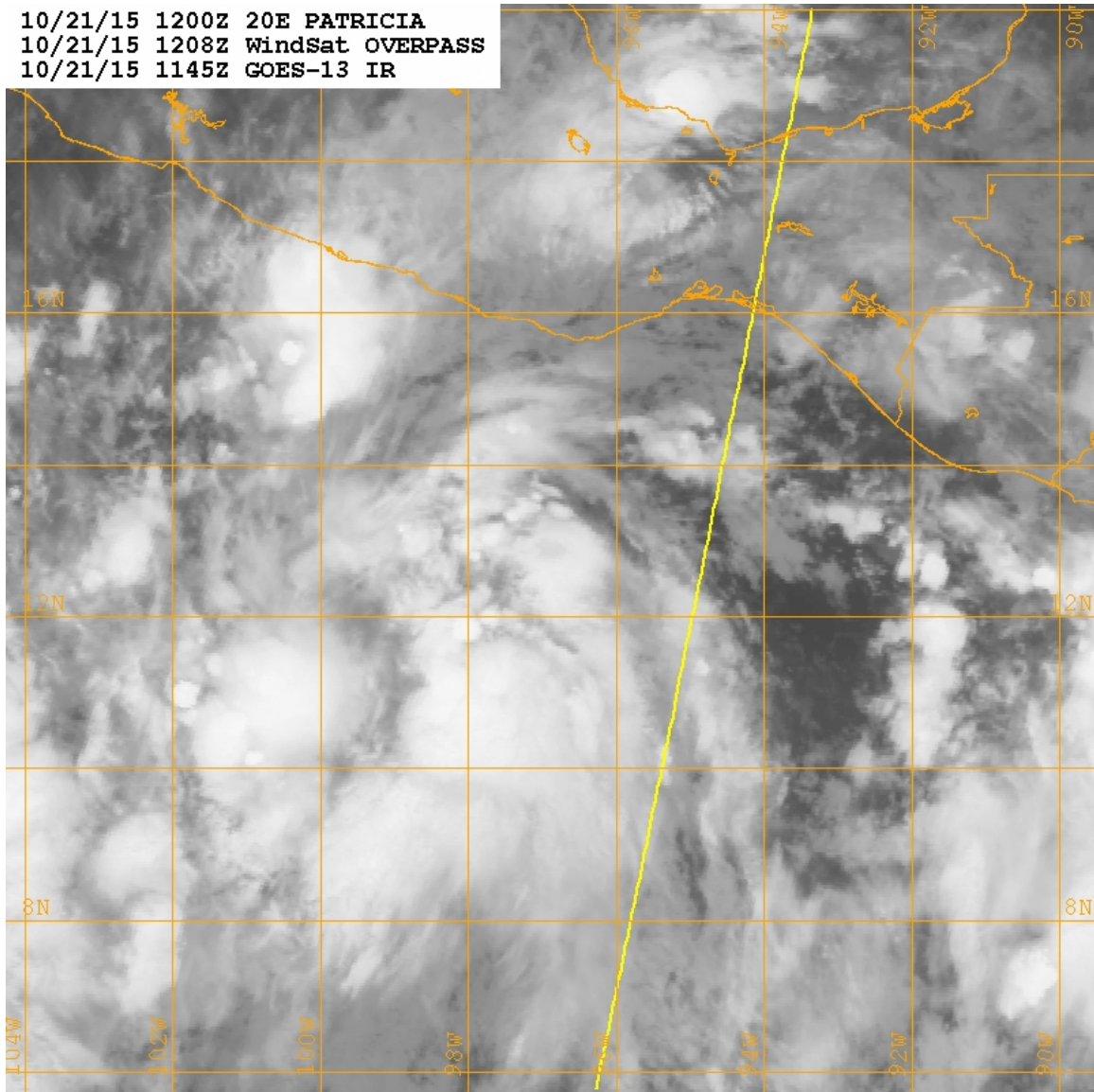


Figure 2. Composite infrared satellite image of Tropical Storm Patricia (20E) at 1145 UTC 21 Oct 2015. Source: Naval Research Laboratory (NRL, 2017).

Patricia then moved over abnormally warm water and began a period of extremely rapid intensification. The Tropical Storm was upgraded to Hurricane status at 0000 UTC 22 October (Figure 3) after having quickly organized into a nearly symmetric system around a very small and clearly defined eye.

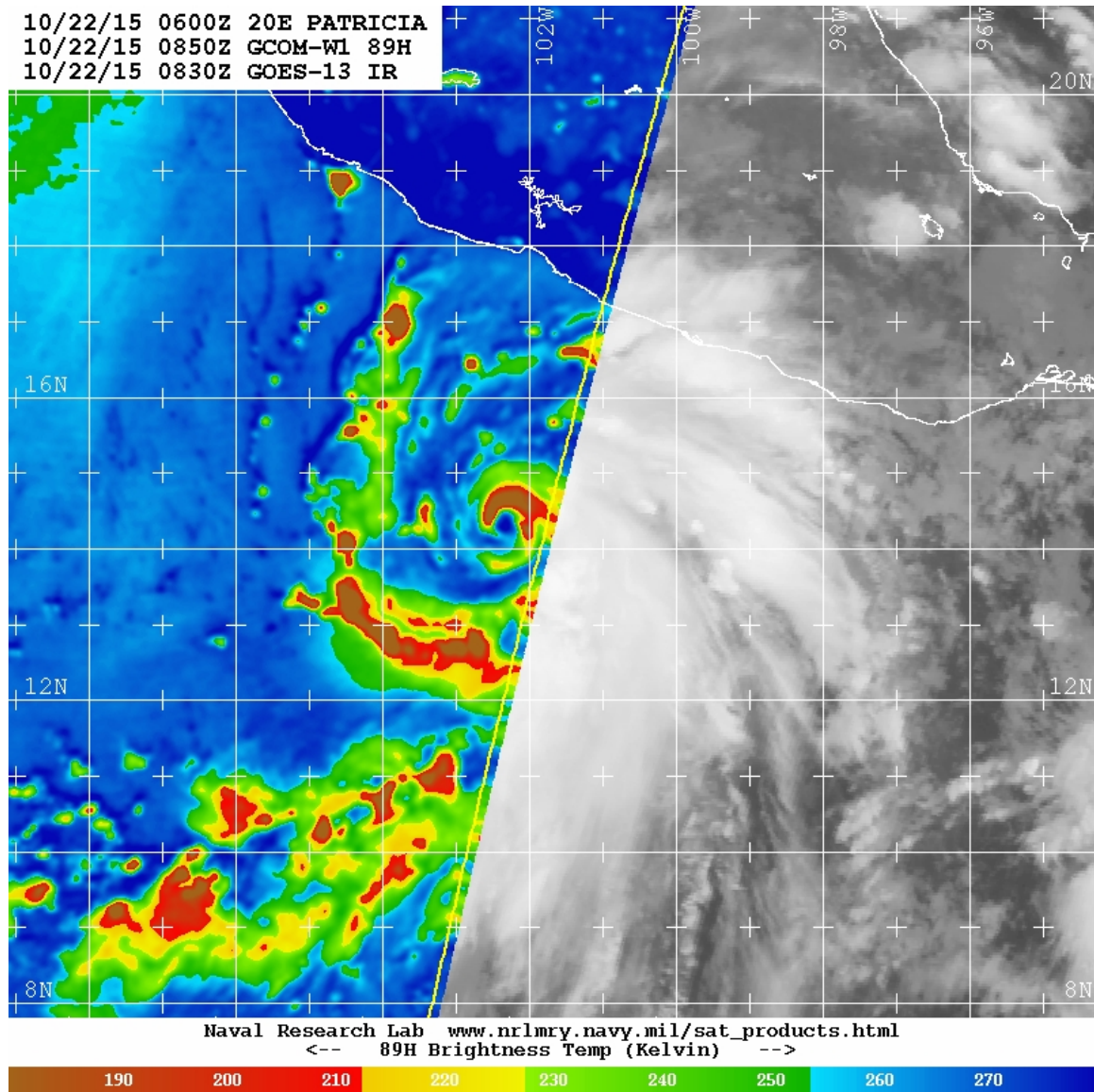


Figure 3. Combination of a 85GHz microwave satellite image (K, color scale at bottom) at 0850 UTC 22 October on the left side and an infrared satellite image at 0830 UTC 22 October on the right side.
Source: NRL (2017).

When the next aircraft reconnaissance mission reached the TC around 1800 UTC 22 October, it observed maximum winds of 115 kt (59.2 m/s) and a central pressure of 957 mb. During this continuing period of extreme intensification, NWP models predicted the intensity would reach 160 kt (82.3 m/s) just 18 hours later. Patricia finally exceeded even the strongest expectations with intensity of 185 kt (95.2 m/s) around 1200 UTC 23 October (Figure 4) before reaching the western edge of the mid-level ridge and turning northeast toward landfall on the west coast of Mexico.

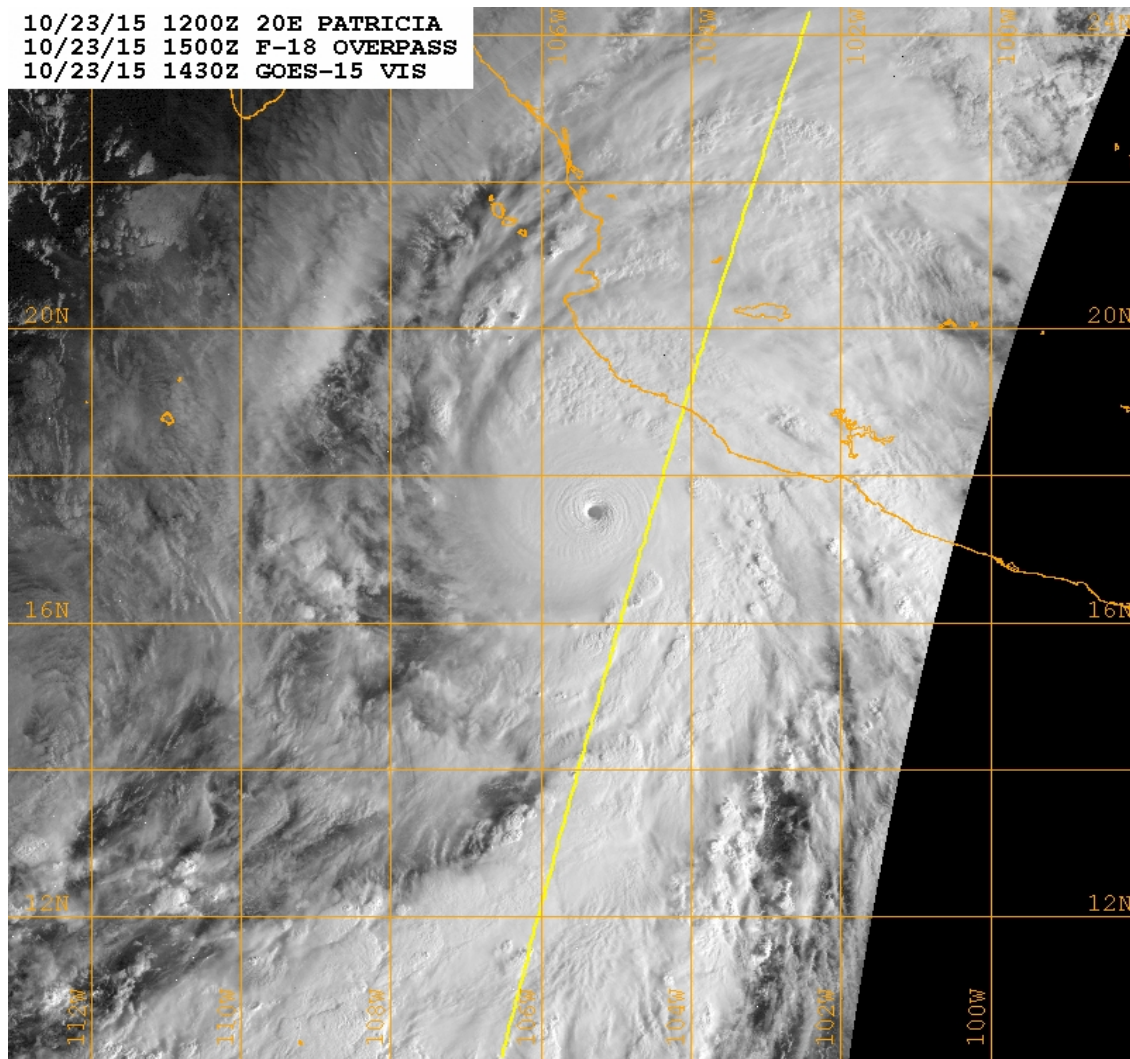


Figure 4. Visible satellite image of Hurricane Patricia at 1500 UTC 23 October near time of maximum intensity. Source: NRL (2017).

In connection with an upper-level shortwave approaching from the northwest, Patricia's translation speed increased prior to landfall at 2300 UTC 23 October near Playa Cuixmala. Patricia had already rapidly weakened in response to increased vertical wind shear, so the intensity at landfall was 130 kt (66.9 m/s), and Patricia continued to rapidly weaken as it moved over land and into high terrain (Kimberlain et al., 2016).

B. OBSERVED TRACK AND INTENSITY

In the NHC best track for Hurricane Patricia, the initial west-southwest motion and slow forward movement can clearly be seen south of the Gulf of Tehuantepec (Figure 5). Patricia then turned to the west-northwest on 21 October and rapidly intensified into a major hurricane late on 22 October. Based on satellite imagery between 0600 UTC and 1800 UTC 23 October, NHC determined that Patricia's maximum intensity occurred between those times (Figure 6; Kimberlain et al., 2016).

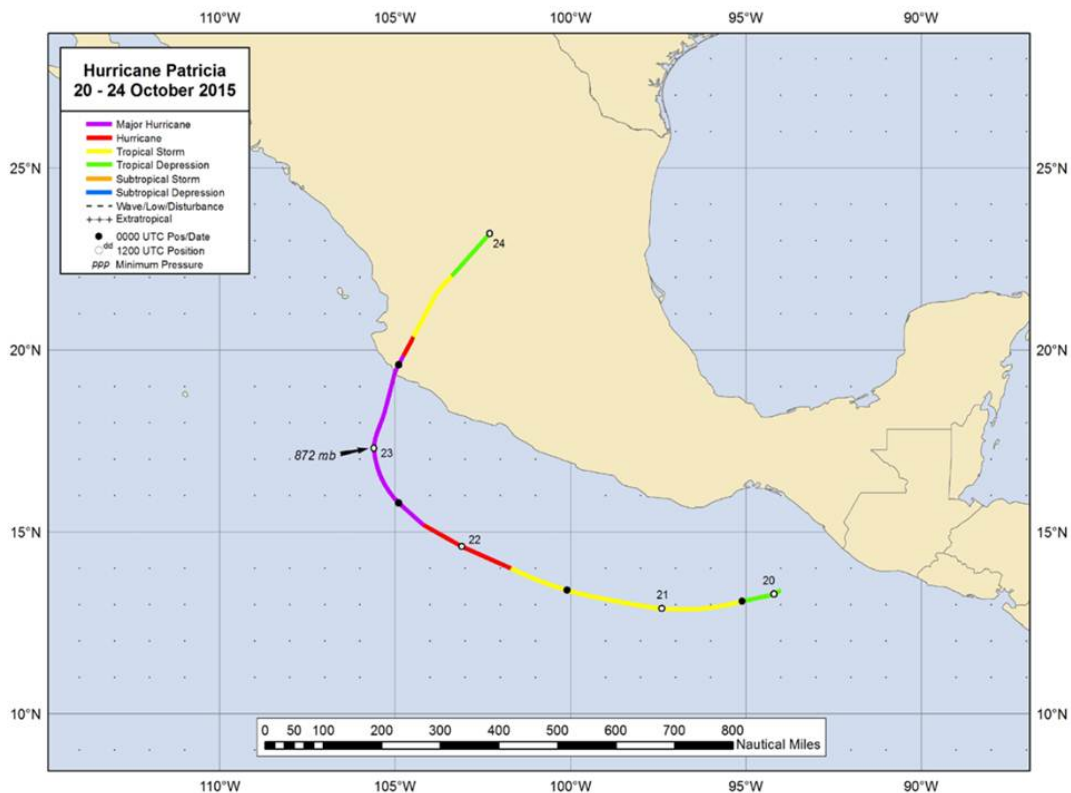


Figure 5. Track of Hurricane Patricia. Source: Kimberlain et al. (2016).

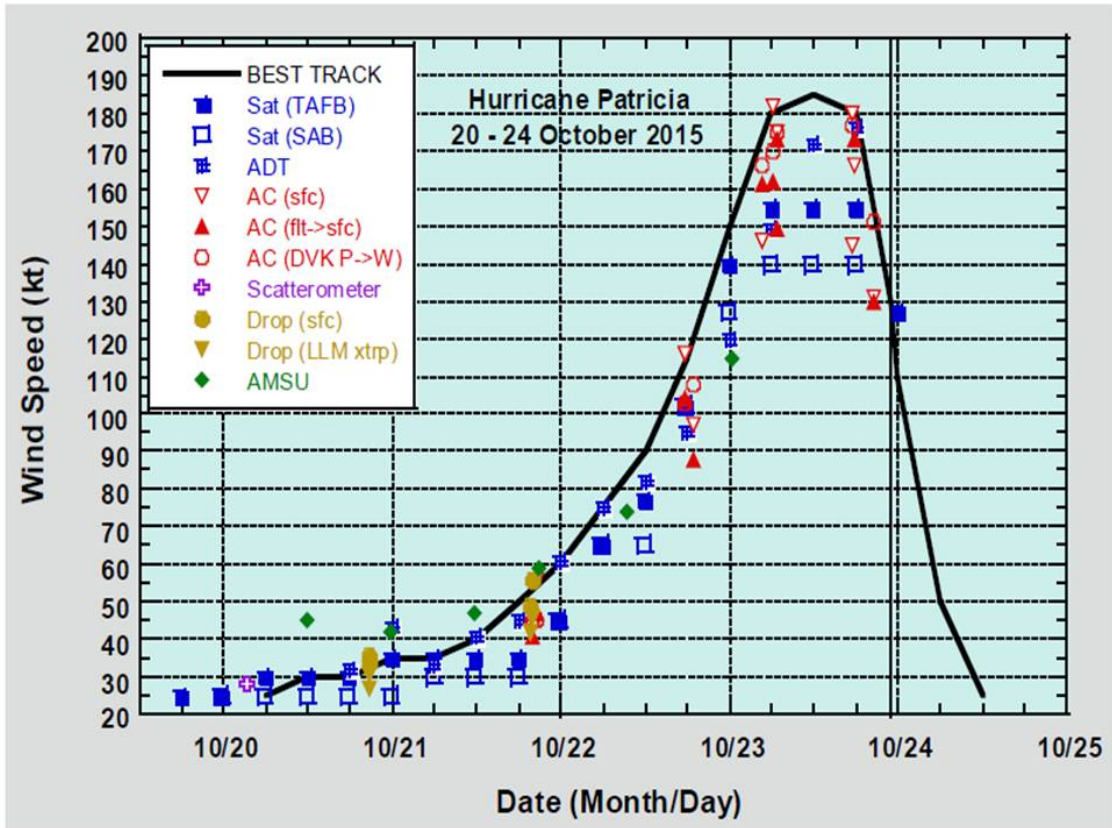


Figure 6. Various sources for intensity estimates (see inset) for Hurricane Patricia between 20–24 October 2015 and the NHC best track intensities (black line). Source: Kimberlain et al. (2016).

C. DEVELOPMENT OF OUTFLOW JETS

Due to the relative lack of observations in the middle and upper levels of TCs, one of the least-studied mechanisms for TC intensity is the outflow layer and the impact of the upper-level anticyclone structure on the intensity of the TC. Merrill (1988) found differences in outflow structure between intensifying and weakening TCs (Figure 7).

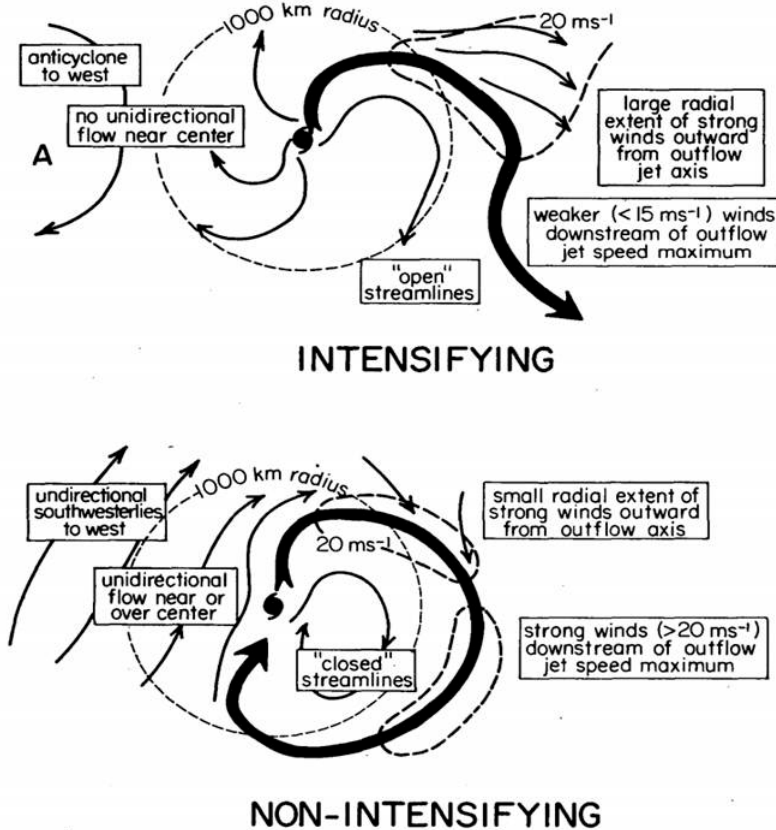


Figure 7. Schematic of the streamlines (thin lines) and outflow jets (thick lines) for intensifying TCs (top) and non-intensifying TCs (bottom).
Source: Merrill (1988).

Note that intensifying TCs tend to have strong jet axes directed outward from the core with spreading streamlines downstream. Additionally, the most intense cyclones tend to develop not one, but two outflow jets directed away from the core: one poleward toward the westerlies and one equatorward toward the easterlies (Rappin et al., 2011). By contrast, the non-intensifying TCs tend to have somewhat closed streamlines and are affected by unidirectional flow penetrating to near (or even over) the TC center.

The Hurricane Patricia outflow structure is well-depicted by the Atmospheric Motion Vectors (AMV) and satellite imagery even prior to its rapid intensification on 21 October (Figure 8), the 100–250 mb winds above Patricia depicted an open streamline pattern, with one outflow jet extending from the northwest quadrant of Patricia into the

Gulf of Mexico and another less distinctive and broader outflow directed toward the south.

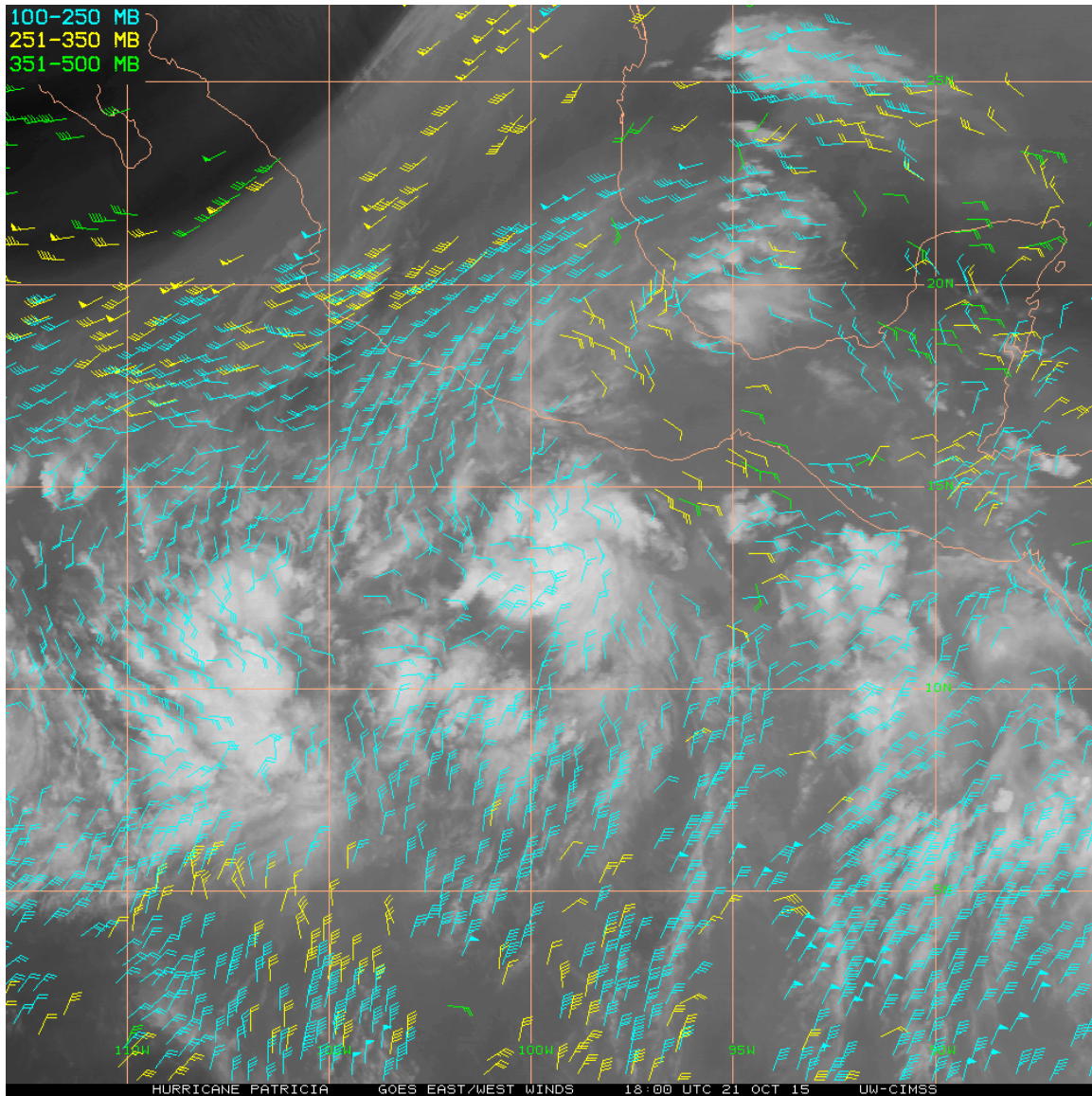


Figure 8. Infrared satellite imagery and AMVs at 1800 UTC 21 October 2015.
Source: Cooperative Institute for Meteorological Satellite Studies
(CIMSS; 2017).

At 1800 UTC 22 October (Figure 9), Patricia's southern outflow was much better defined and both outflow jets had increased wind speeds away from the core. Additionally, the infrared imagery depicts that the jets had wrapped around the core as Patricia's spiral bands became more prominent.

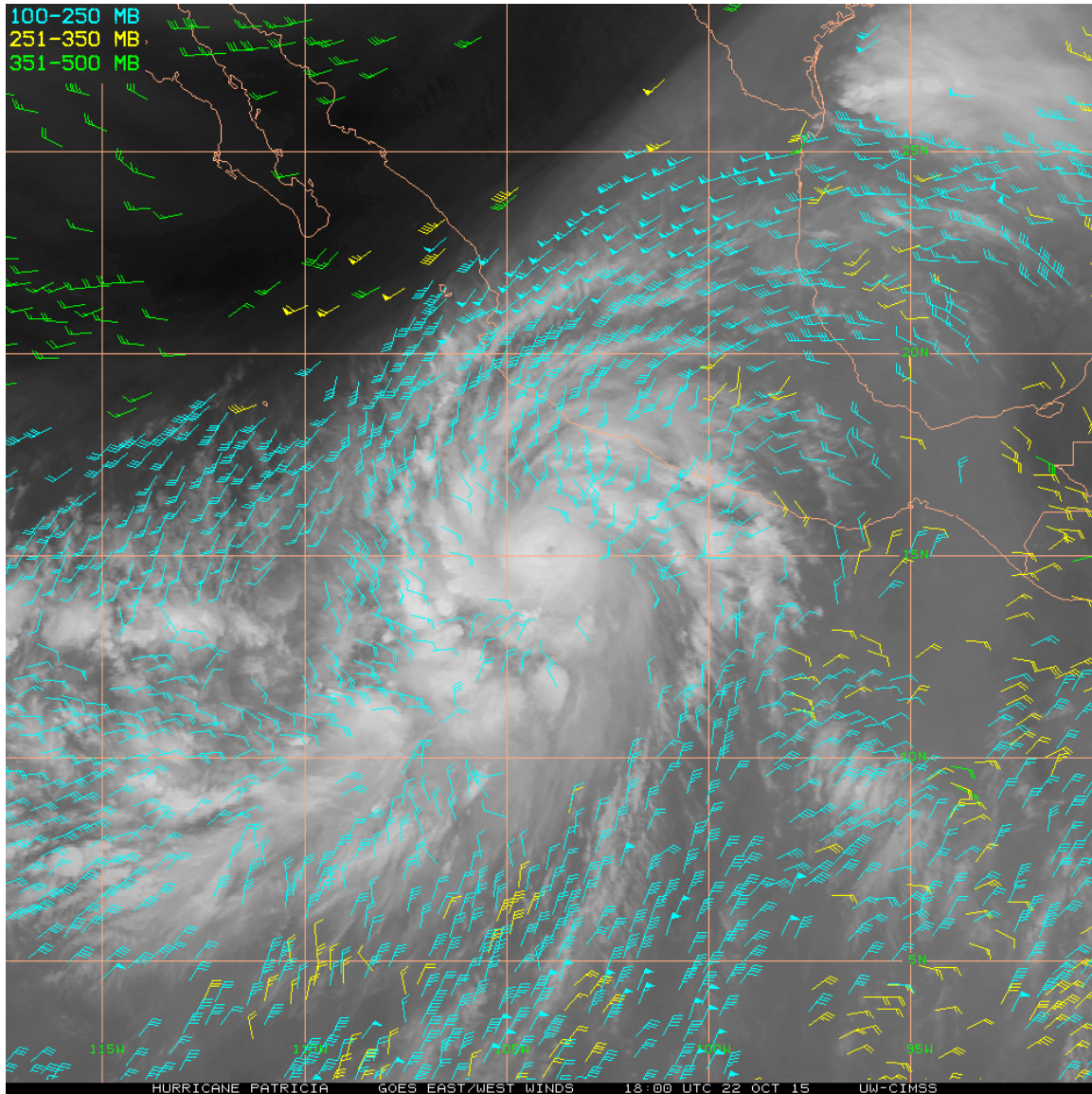


Figure 9. Infrared satellite imagery and AMVs as in Figure 7, except for 1800 UTC 22 October 2015. Source: CIMSS (2017).

At 1800 UTC 23 October (Figure 10), both the equatorial and poleward outflow jets were still present. The poleward jet was even stronger in magnitude. Weakening in the spiral banding in the southwest quadrant of the system, coupled with decreasing upper-level winds in both the southwest quadrant and the equatorial jet, possibly indicates that the intensification of Patricia was nearing an end.

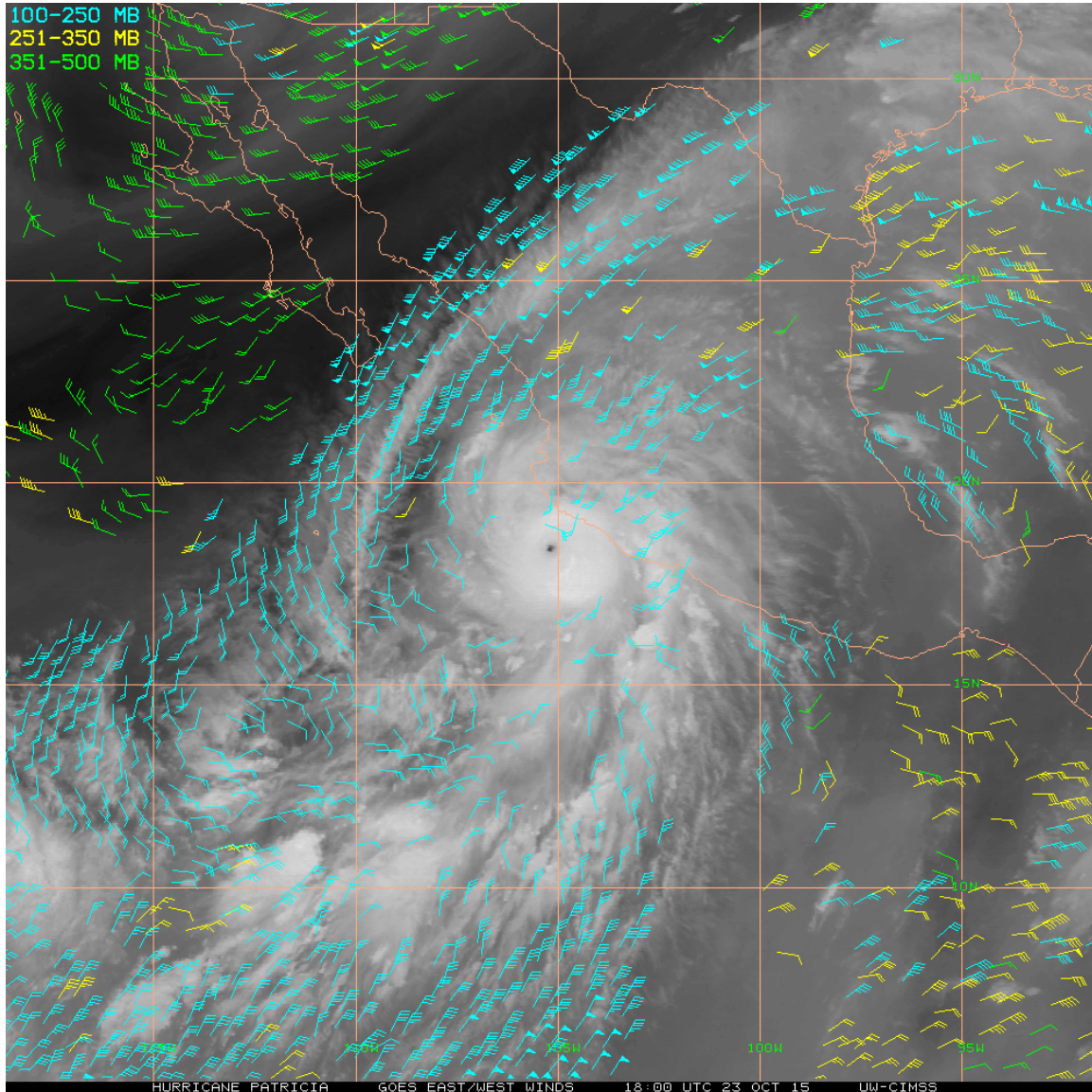
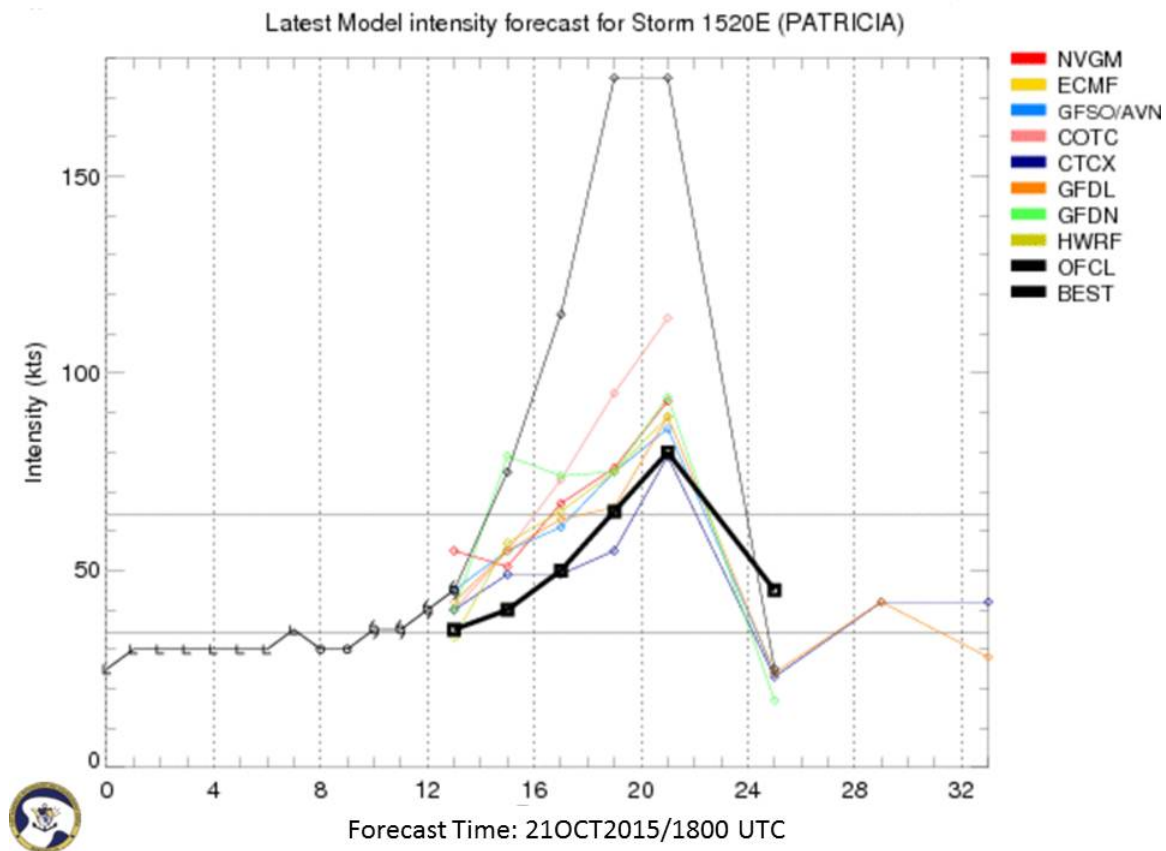


Figure 10. Infrared satellite imagery and AMVs as in Figure 7, except for 1800 UTC 23 October 2015. Source: CIMSS (2017).

D. COAMPS-TC MODEL PERFORMANCE DURING INTENSIFICATION

At 1800 UTC 21 October (Figure 11), which was immediately prior to Patricia's rapid intensification, the CTCX intensity forecast was more conservative than most of the other dynamical NWP models, and was actually very close to the official NHC forecast.



The NHC best track is the thin black line. The NHC official forecast from 1800 UTC 21 October is highlighted with the thick black line. The CTCX forecast from 1800 UTC 21 October is labeled in purple.

Figure 11. Validation of the intensity forecasts from 1800 UTC 21 October for Patricia by various intensity products (inset) versus the NHC best track intensity (thin black line). Source: Fleet Numerical Meteorology and Oceanography Center (FNMOC; courtesy of Raymond Lee).

However, the CTCX model under-predicted the actual winds by 15 kt already at six hours, 30 kt (15.4 m/s) at 12 hours, and by over 105 kt (54 m/s) at peak intensity. One encouraging note is that all of the dynamical models accurately forecast the timing of maximum intensity, even if the predicted winds were far too low.

The CTCX at 1800 UTC 22 October predicted more 24 hr intensification for Patricia than every other dynamical model (Figure 12). However, still the CTCX under-forecast the actual peak intensity by 45 kt (23.2 m/s) at 24 hours. At the end of this forecast period, all of the models began to accurately predict the timing of rapid weakening just prior to and during landfall.

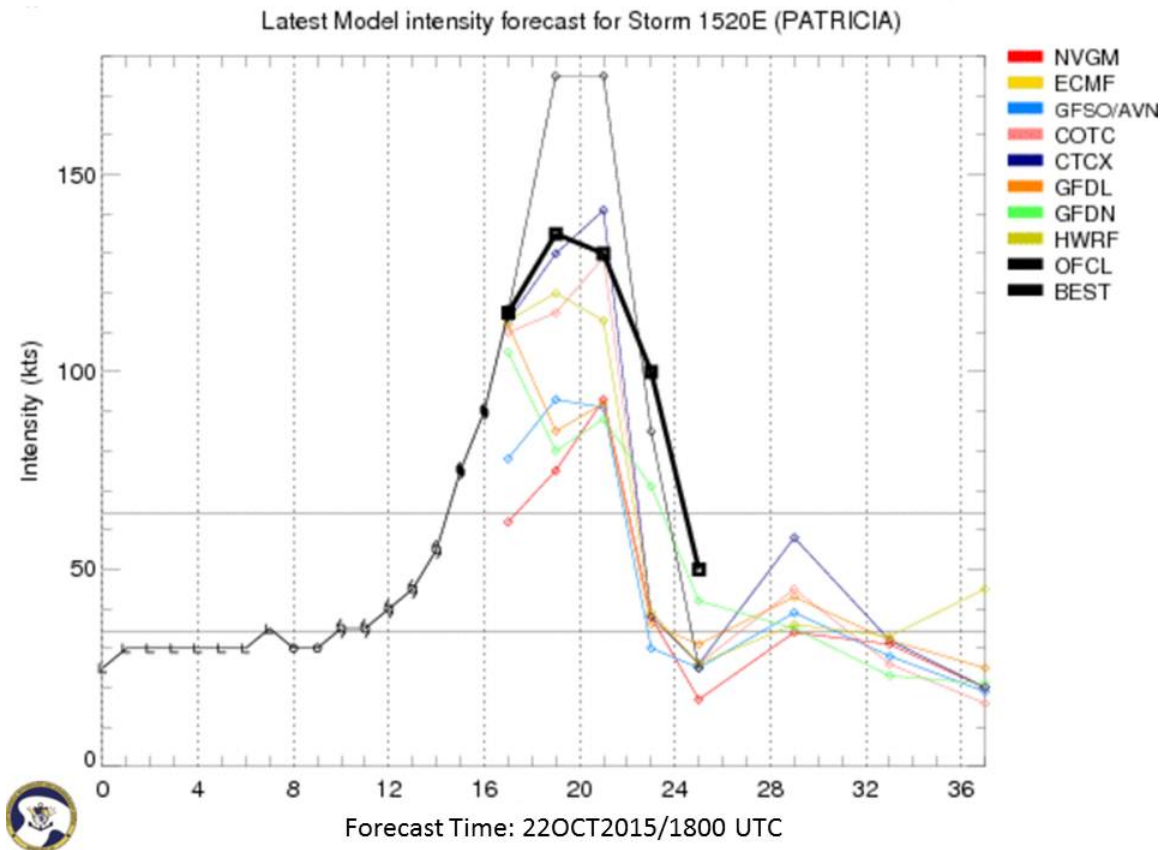


Figure 12. Validation of intensity forecasts as in Figure 10, except for 1800 UTC 22 October. Source: FNMOC (courtesy of Raymond Lee).

The final set of intensity forecasts analyzed here is 1800 UTC 23 October, which was immediately after Patricia reached maximum intensity (Figure 13). At this forecast time, nearly all of the intensity guidance correctly predicted a period of rapid weakening, but the CTCX model's initial intensity more closely matches the NHC analysis than any other dynamical model.

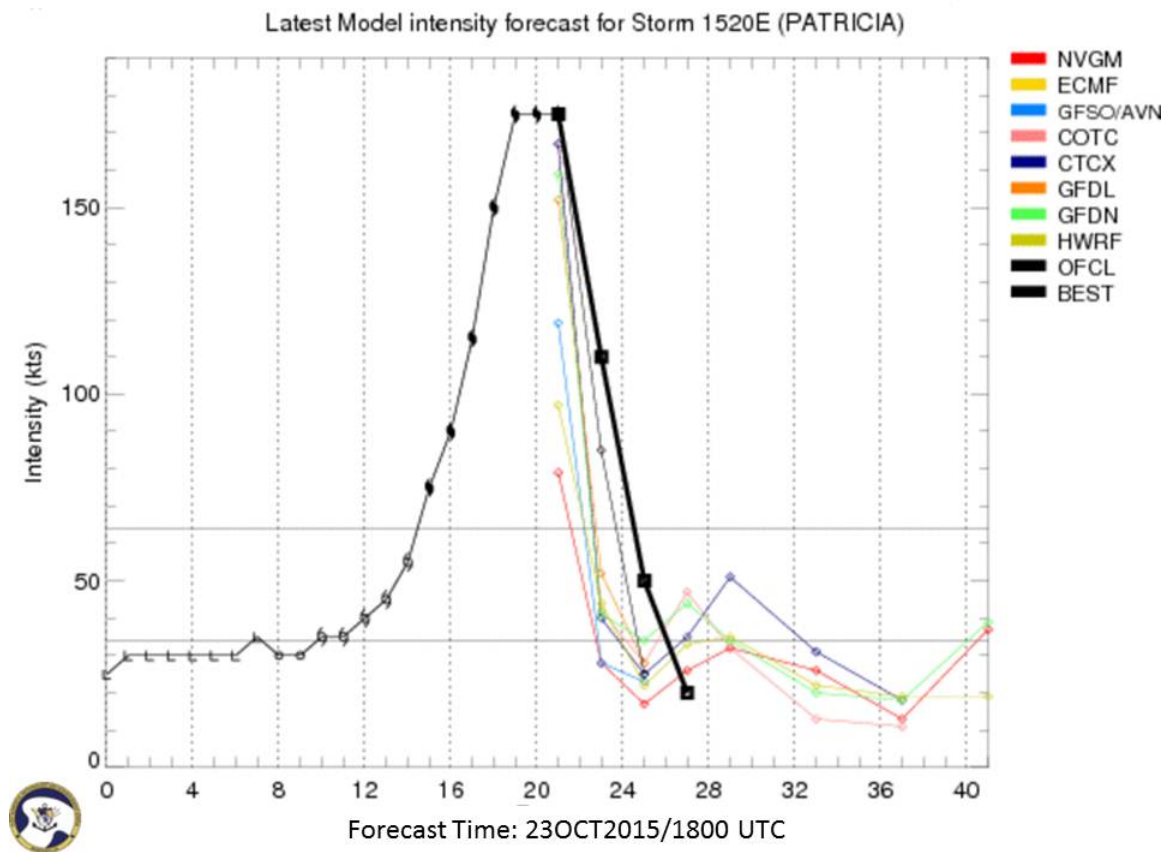


Figure 13. Validation of intensity forecasts as in Figure 10 and 11, except for 1800 UTC 23 October. Source: FNMOC (courtesy of Raymond Lee)

To briefly summarize the performance of CTCX for predicting the intensity of Hurricane Patricia, its accuracy went from below average prior to the rapid intensification to being the best dynamical model after rapid intensification began. However, even though it provided the best intensity forecast on 22 October, COAMPS-TC still under-forecast the peak intensity by a significant margin, and more investigation into the initialization of this model is warranted.

THIS PAGE INTENTIONALLY LEFT BLANK

III. DATA AND METHODOLOGY

A. DATASETS

1. COAMPS-TC (CTCX) Model Data

The model datasets used in this study are from the real-time CTCX model runs during the lifecycle of Patricia. The specific times selected from the model output are 21–23 October 2015 at 1800 UTC, as these times most closely correspond with the in-situ observations collected as part of the TCI field program. From Doyle et al. (2014):

The COAMPS-TC atmospheric model uses the nonhydrostatic and compressible form of the dynamics and has prognostic variables for the three components of the wind (two horizontal wind components and the vertical wind), the perturbation pressure, potential temperature, water vapor, cloud droplets, raindrops, ice crystals, snowflakes, graupel (soft hail), and turbulent kinetic energy (Hodur, 1997). Physical parameterizations include representations of cloud microphysical processes, convection, radiation, boundary layer processes, and surface layer fluxes. The COAMPS-TC model contains a representation of dissipative heating near the ocean surface, which has been found to be important for tropical cyclone intensity forecasts (Jin et al., 2007). The COAMPS-TC system uses a flexible nesting design, which has proven useful when more than one storm is present in a basin at a given time, as well as special options for moving nested grid families that independently follow individual tropical cyclone centers of interest. ... COAMPS-TC uses three standard nested grids of 45 km, 15 km, and 5 km horizontal resolution and 40 vertical levels that extend from 10 m to approximately 30 km. (Doyle et al., 2014)

“The inner two grid meshes follow the storm” and are re-centered based on the official forecast bogus vortex for each run (Doyle et al., 2014).

2. Office of Naval Research (ONR) Tropical Cyclone Intensity (TCI) Initiative

The goal of the TCI program is to improve TC intensity predictions, including rapid intensification and rapid decay, by better understanding TC structure change, and specifically changes in the upper-level outflow layer. In-situ observations of Hurricane Patricia were collected by the Hurricane Imaging Radiometer (HIRAD) and High

Definition Sounding System (HDSS) dropsondes from the NASA WB-57 aircraft, as well as flight-level observations from aircraft reconnaissance missions directed by NHC.

a. Hurricane Imaging Radiometer (HIRAD)

The HIRAD sensor is a multi-band passive microwave radiometer operating between 4 GHz and 6.6 GHz embarked on the WB-57 aircraft. It was developed by scientists and engineers at NASA's Marshall Space Flight Center (MSFC), the University of Central Florida, and the University of Michigan to measure ocean surface wind speeds in TCs. The surface wind speed measurements generated by the instrument use excess brightness temperature calculations that compute the difference between observed brightness temperatures and a modeled top of the atmosphere brightness temperatures where the surface wind speed is set to zero. (Braun et al., 2013; Cecil, 2016)

b. High Definition Sounding System (HDSS) Dropsondes

The HDSS uses expendable digital dropsondes (XDD) to measure winds, skin sea-surface temperatures (SST) and vertical profiles of pressure, temperature, and humidity near TCs (Table 1). In addition to the XDD, the HDSS also includes a system of antennas and receivers that receive and record the data from XDDs as they descend, collecting Global Positioning System (GPS) location and altitude in addition to the aforementioned environmental measurements (Black et al., 2017; Bell et al., 2015). The XDDs are deployed via an Automated Dropsonde Dispenser (ADD) located under the aft fuselage of the WB-57 aircraft (Figure 14). All HDSS data used in this study has been obtained from the TCI project (TCI; Doyle et al., 2017; available at catalog.eol.ucar.edu/tci).



Figure 14. View of the Automated Dropsonde Dispenser (ADD) aboard the NASA WB-57 aircraft flying over outflow region of Tropical Storm Patricia. Source: Doyle et al. (2017).

Table 1. Expendable Digital Dropsonde (XDD) sensor specifications, including range, accuracy, and resolution. Adapted from Black et al. (2017).

Parameter	Sensor type/ data rate	Range	Accuracy	Resolution
Temperature	Thermistor/2 Hz	-90° to 50°C	±0.14°C	0.016°C
Pressure	MEMS ^a /2 Hz	150-1150hPa	±1.5hPa at 25°C	±2.5hPa
Relative Humidity	MEMS ^a /2 Hz	10%-100% for temperature > -37°C	1.8% at 25°C	0.1%
SST	Infrared micro-radiometer 9-11μm/1Hz	0°-50°C	±0.2°C at 25°C	0.016°C

a. MEMS: Microelectromechanical System

3. Satellite Data

The primary satellite datasets used are imagery from NASA's Geostationary Operational Environmental Satellite (GOES) system. Atmospheric Motion Vectors (AMVs) from this system will be used to compare the horizontal outflow structure (outflow jets) to the upper-level winds in the initial conditions of the CTCX model.

4. Aircraft Reconnaissance Data

The NOAA aircraft reconnaissance datasets used in this study are from 690 mb to 710 mb as the aircraft flew through Patricia's eyewall and center position at 1736 UTC 22 October and 1734 UTC 23 October as part of a collaborative observing program (Doyle et al., 2017; available at https://www.eol.ucar.edu/projects/tci/flight_data). The flight-level wind speeds are accurate to within 4 kt (2.06 m/s), pressure height to within 10 m, and temperature to within 1 °C (USDOD, 2017).

B. METHODOLOGY

1. Zero-Wind Center (ZWC) Method for Acquiring Wind Vectors in Storm-Relative Coordinate System

Creasey and Elsberry (2017) have utilized the high temporal resolution HDSS measurements and a version of the Willoughby and Chelmow (1982) technique to find the Zero-Wind Center (ZWC) of a TC (Figure 15). Their ZWC algorithm will be used to find Patricia's core in three dimensions. Whereas the Willoughby and Chelmow method uses wind vectors from observed flight-level winds and calculates normals to each wind vector in the direction of the storm center, Creasey and Elsberry (2017) calculate those normals to the HDSS dropsonde winds as the dropsondes deployed near the TC center fall to the surface. Where these normals intersect is the TC center at that particular elevation.

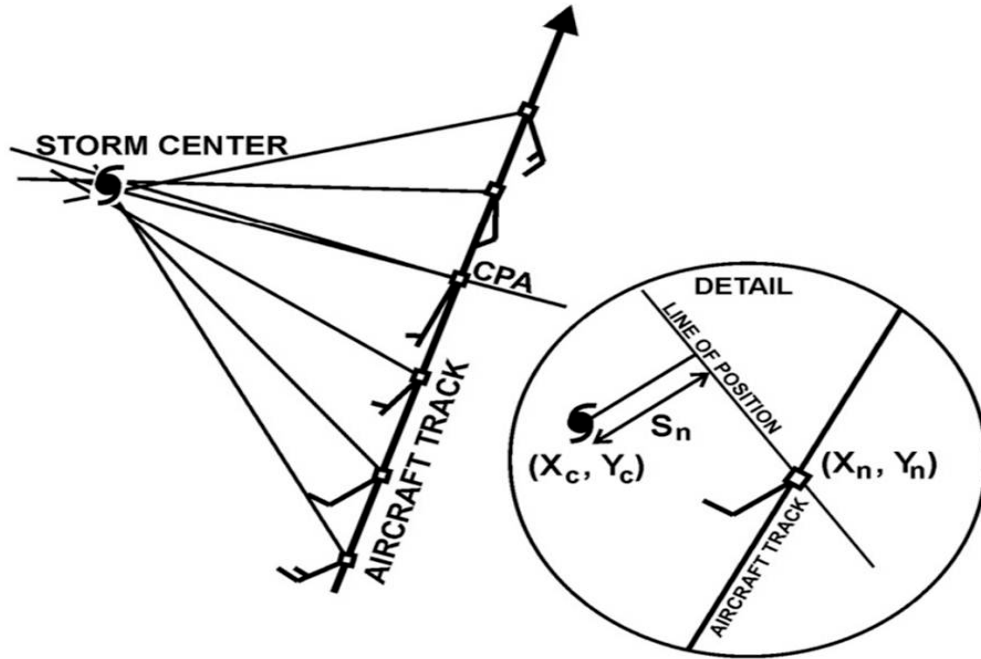


Figure 15. Schematic of the Willoughby and Chelmow (1982) technique for locating a TC center from the changing flight-level wind directions as the aircraft flies near the center. Source: Creasey and Elsberry (2017).

Note that while HDSS dropsondes are deployed along the flight path in a straight line from a height of 60,000 ft (18,288 m), they drift with the wind, and especially in the strong winds near the eye-wall. Although in many cases the dropsondes are displaced horizontally in response to those winds, the HDSS system records precise GPS location data of the XDDs. The rapid deployment of multiple XDDs can be used to calculate the ZWCs at many vertical levels by computing the intersection of normals to each wind vector. An example from Creasey and Elsberry (2017) of the ZWCs between 9.5 km (upper red dot) and 1.5 km (lower red dot) at 1900 UTC 4 October 2015 in Hurricane Joaquin is shown in Figure 16. Note that the ZWCs in the lower troposphere are vertically stacked, but at upper levels the vortex is tilted to the east by approximately 20 km. Creasey and Elsberry (2017) also calculate the storm motion vector using a series of ZWCs from a sequence of two center over-passes with the HDSS data. Once the storm motion vector is computed, wind vectors observed by the HDSS dropsondes may be converted to storm-relative winds by subtracting the storm motion vector. After the

winds are converted to storm-relative winds, the other XDD readings (pressure, temperature, humidity) may also be analyzed in the new storm-relative coordinate system using latitude and longitude offsets from the ZWCs. Since not all of the HDSS readings occurred at precisely 1800 UTC when the CTCX model run was initialized, the storm motion vector may also be used to adjust the HDSS observation positions to 1800 UTC for analysis.

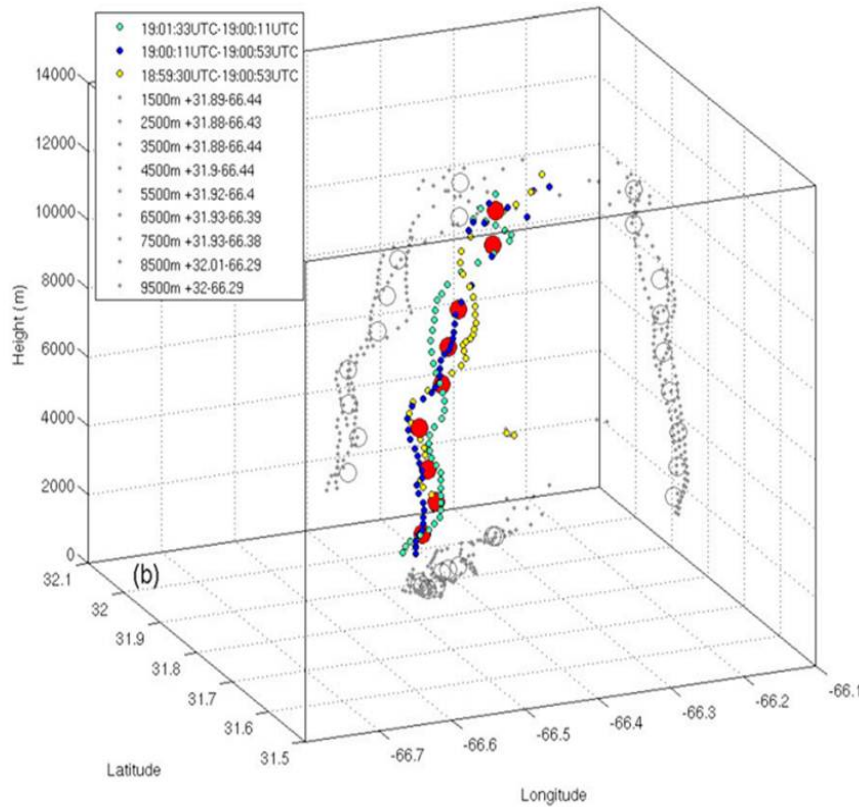
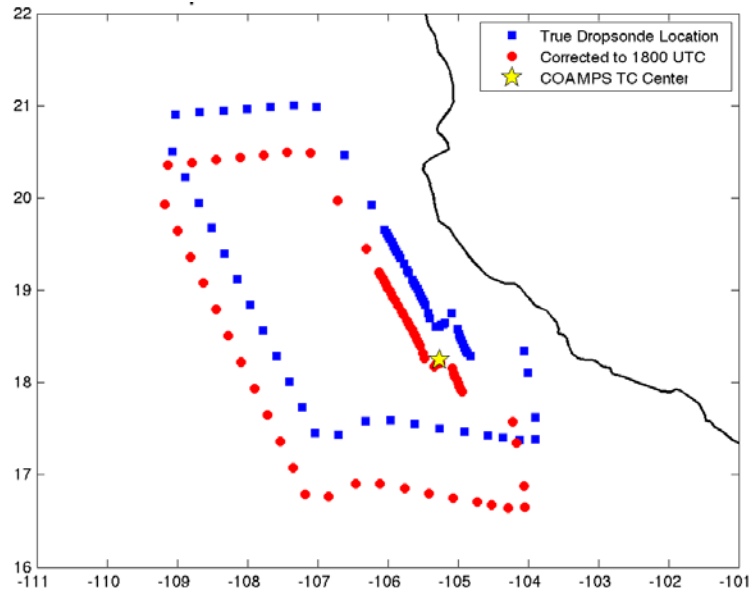


Figure 16. Vortex tilt of Hurricane Joaquin (2015) based on ZWCs each kilometer from 9.5 km to 1.5 km (large red dots) derived from HDSS wind vector directions. Source: Creasey and Elsberry (2017).

2. Determining Differences in TC Structure between COAMPS-TC Initial Conditions and Observations

In order to compare the TC structure in the CTCX initial conditions to the HDSS observations, the CTCX winds are first converted to storm-relative winds by subtracting the storm motion vector of Patricia (determined by the ZWC analysis). Then the HDSS

observations are placed in the same storm-relative coordinate system as CTCX by adding the latitude and longitude offsets from the ZWC to the CTCX center. An example of this correction is provided in Figure 17 (provided courtesy of Mary S. Jordan).



The true dropsonde locations (blue squares) deployed at approximately 2000 UTC, the corrected HDSS locations (red dots) have been adjusted to the CTCX center (star) by subtracting the storm motion between 1800 and 2000 UTC. X-axis: longitude in deg E. Y-axis: latitude in deg N. The thick black line is the Mexico coastline. Image courtesy of Mary S. Jordan.

Figure 17. Example of HDSS storm-relative correction at 500 mb for 1800 UTC
23 October 2015

Once both HDSS observations and CTCX data are in the same storm-relative coordinate system, a series of two-dimensional radial plots will be used to find anomalies in the model's initial representation of Patricia's structure. The primary fields used to compare the dynamic and thermodynamic structure of Patricia in CTCX and in-situ observations are wind speed, potential temperature, and geopotential height. These fields will be compared at the 200 mb, 300 mb, 500 mb, 700 mb, and 850 mb pressure levels. These factors are selected to analyze important features of TC structure, such as warm core magnitude and location, vertical structure of tangential winds, and radial structure of

the tangential wind. The innermost nested domain of CTCX with a horizontal grid spacing of two-day period 5 km will be used for these comparisons.

In addition to qualitatively exploring differences in Patricia's structure from in-situ observations and CTCX data, a quantitative evaluation of the CTCX initial conditions can also be computed from the anomalies observed in the scatter plots, including the Mean Error (ME), Mean Absolute Error (MAE), and Root Mean Square Error (RMSE). Equations for these error statistics are given in Figure 18.

$$ME = \frac{\sum_1^n (M - O)}{n}$$

$$MAE = \frac{\sum_1^n |(M - O)|}{n}$$

$$RMSE = \sqrt{\frac{\sum_1^n (M - O)^2}{n}}$$

M is the CTCX model value, O is the in-situ observation value, and n is the number of points (i.e., number of HDSS drops) at which they are being compared.

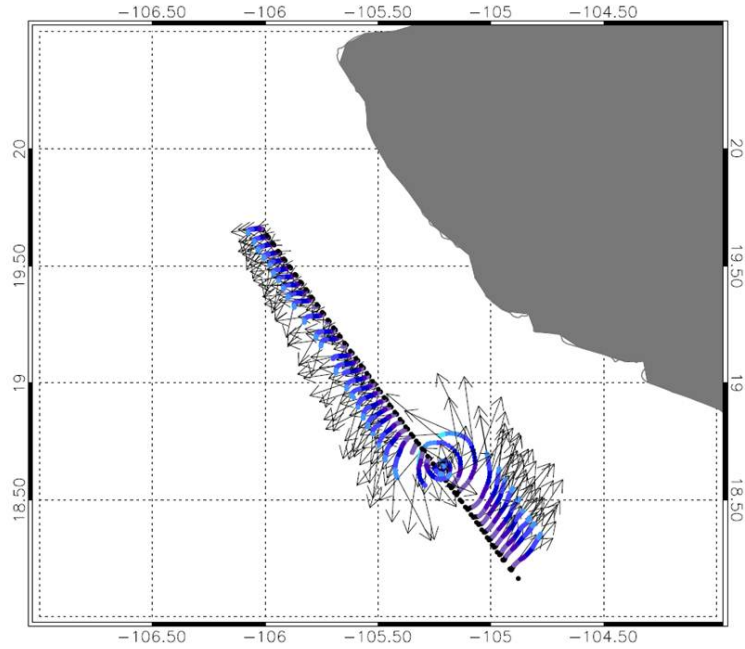
Figure 18. Error equations used in this study

IV. RESULTS

This chapter will begin with an analysis of the observed HDSS dropsonde drift effect, as it plays a key role in understanding the results that follow. Next, the wind speed magnitude and direction in the CTCX initial conditions and a variety of observations will be compared, beginning with HIRAD observations of winds near the surface and then the upper-level Atmospheric Motion Vectors (AMVs). True wind (not storm-relative winds) will be used in both the AMV and HIRAD comparisons. Finally, a storm-relative verification of HDSS and CTCX will be provided for wind speed, potential temperature, and geopotential height at five pressure levels: 200, 300, 500, 700, and 850 mb. Here, radial profiles of the quantities will be shown to understand differences in both the inner-core region and outer circulation.

A. HDSS DROPSONDE DRIFT

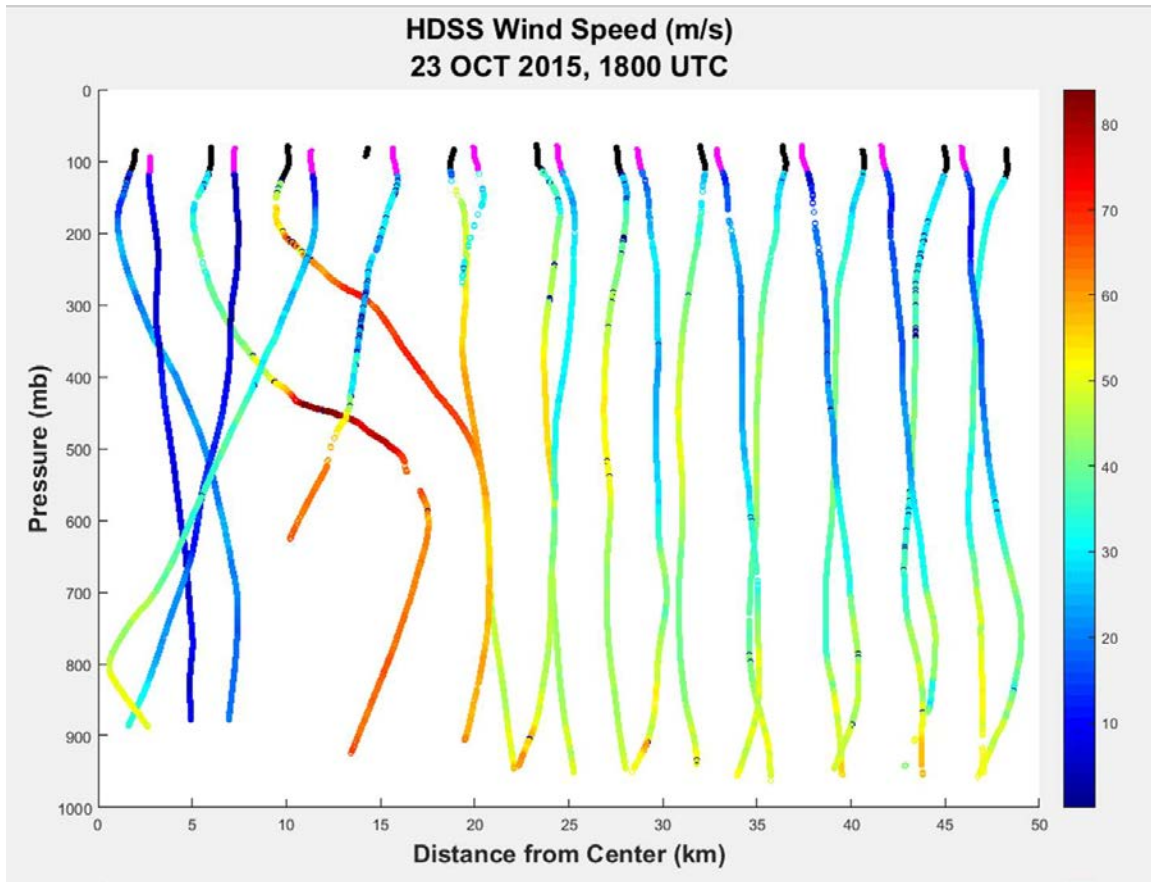
For 1800 UTC 22 October and 1800 UTC 23 October, a significant lack of HDSS data was noticed near the eye-wall below 300 mb. This data deficiency motivated a brief study of the horizontal displacement of the XDDs as they fell from 60,000 ft (18,288 m) to the surface. Dropsonde drift was an expected result in this study, especially given the strong winds near Patricia's eye-wall. However, for both 22 October and 23 October, this drift contributed to scarce data in the eye-wall at levels below 300 mb, and thus is of critical importance to discuss prior to comparing low level wind structure. Figure 19 displays the extent of the horizontal displacement of the dropsondes, which drifted further near the TC center than in the outer regions due to the very strong tangential flow at this time. While the dropsondes move approximately tangentially, there is some radial movement as well. In particular, distinct outward movement is seen in the two dropsondes just southeast of the TC center.



Black dots indicate the HDSS deployments from 60,000 ft (18,288 m). Blue lines indicate the drift as the dropsonde descends to the ocean surface. Arrows indicate the wind vectors at various pressure levels as the dropsondes fall to the surface.

Figure 19. Southwest to northwest flight track of the NASA WB-57 through the center of Hurricane Patricia at approximately 1800 UTC 23 October

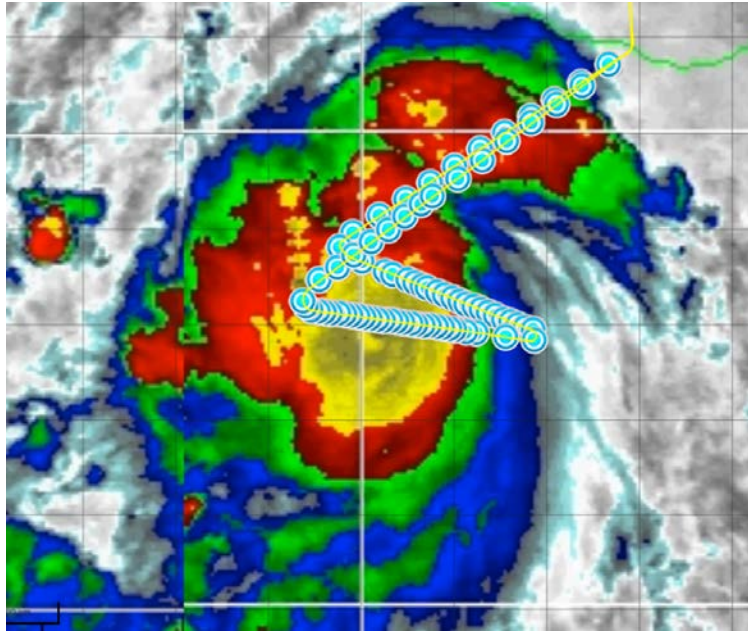
Figure 20 depicts an example of this effect for 23 October, where only one dropsonde was able to reach the lower levels in the eye-wall, which by that time had already tightened to a radius of 7 n mi (Kimberlain et al., 2016), equivalent to 12.96 km.



Profiles highlighted in black near the top were deployed when the WB-57 aircraft was inbound the TC center. Profiles highlighted in magenta were deployed while the aircraft was outbound from the TC center.

Figure 20. HDSS-observed wind speeds (color scale on right) as a function of distance from Patricia's zero-wind center (ZWC) at approximately 1800 UTC 23 October

Due to the insufficient amount of HDSS data in the lower level eye-wall region for 22 and 23 October, HIRAD and NOAA and flight-level reconnaissance mission data will be used to supplement the HDSS data for this study. For further context, Figures 21–23 are provided to display the flight path of the NASA WB-57 and the location of the HDSS missions in relation to Patricia for 21–23 October.



The blue circles indicate dropsonde deployments. The green line is the coastline of Mexico.

Figure 21. NASA WB-57 flight path (yellow line) overlaid on GOES enhanced infrared image of Patricia at 1830 UTC 21 October.
Source: TCI; Doyle et al. (2017).

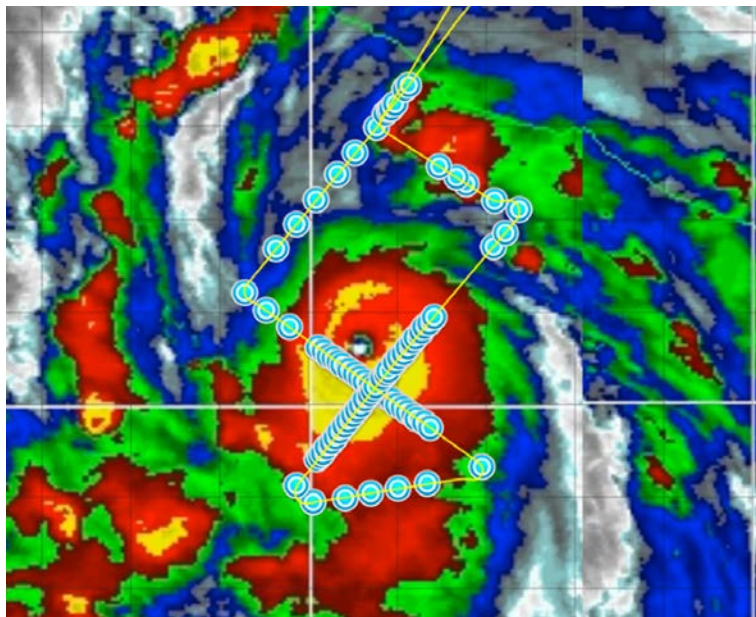


Figure 22. NASA WB-57 flight path as in Figure 19, except at 1815 UTC 22 October

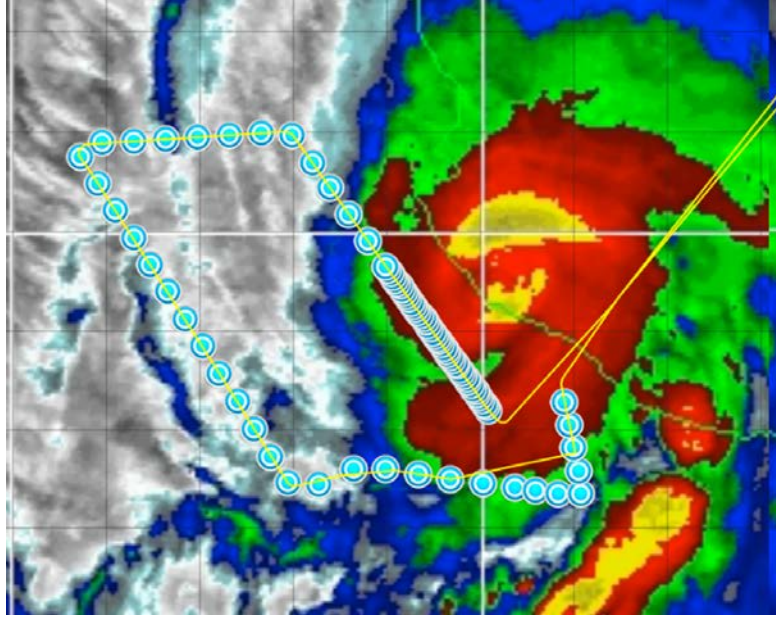
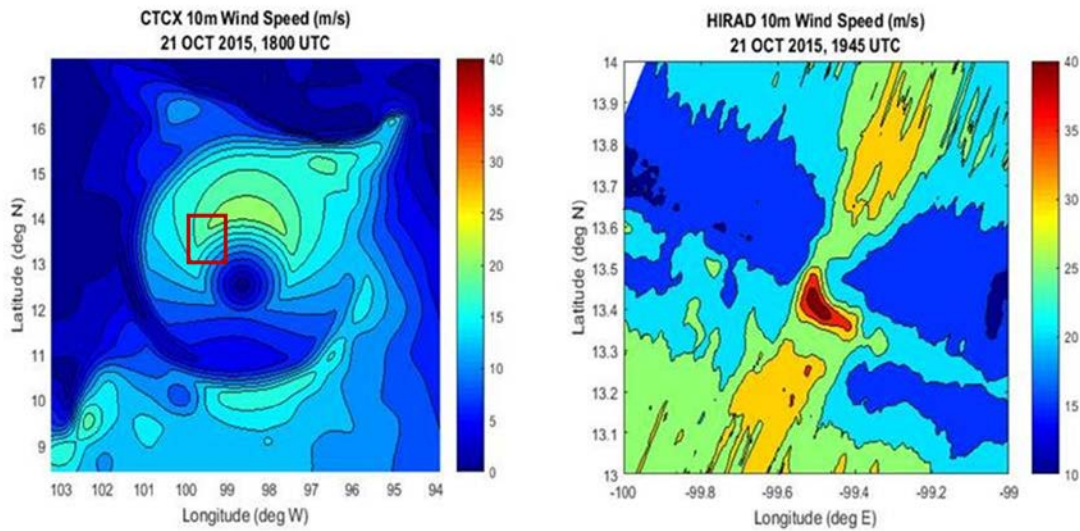


Figure 23. NASA WB-57 flight path as in Figure 19, except at 2015 UTC 23 October

B. WIND SPEED COMPARISONS

1. Near-surface Wind Field Structure

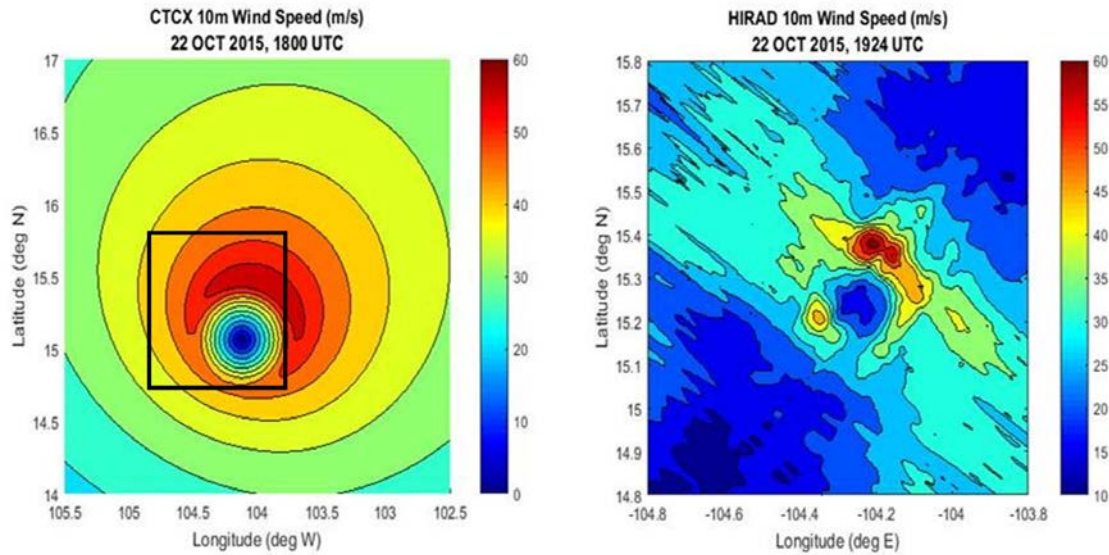
On 21 October when Patricia was merely a well-defined Tropical Depression (TC) with pockets of deep convection, the 5 km horizontal resolution CTCX initial conditions (Figure 24, left) did not have the capability of depicting the localized details that HIRAD (Figure 24, right) was able to observe. Note that the HIRAD analysis is on a much smaller scale and its location is inside the area of maximum winds in the CTCX initial conditions with a grid resolution of 5 km. Whereas the HIRAD has detected a small region of wind speeds greater than or equal to 35 m/s (i.e., hurricane stage rather than TD) on the poleward side of the center, the maximum wind speed in the CTCX analysis is approximately 20 to 25 m/s at a larger radius (120–130 km) to the north of the center. In addition, the HIRAD analysis has regions (yellow color) of wind speeds greater than 30 m/s at larger radii both to the north and to the south. While the northern region may roughly correspond to maximum wind speed in the CTCX analysis, the southern maximum has no corresponding feature in the CTCX analysis.



Left: Wind speed (m/s, color scale on right) at 10 m elevation in the CTCX initial conditions at 1800 UTC 21 October. Right: Surface wind speed (m/s, color scale on right) from the HIRAD analysis of Patricia at 1945 UTC 21 October. The red box indicates the extent of the HIRAD image on the left panel.

Figure 24. Wind speed at 10 m elevation in the CTCX initial conditions at 1800 UTC 21 October and surface wind speed from the HIRAD analysis of Patricia at 1945 UTC 21 October

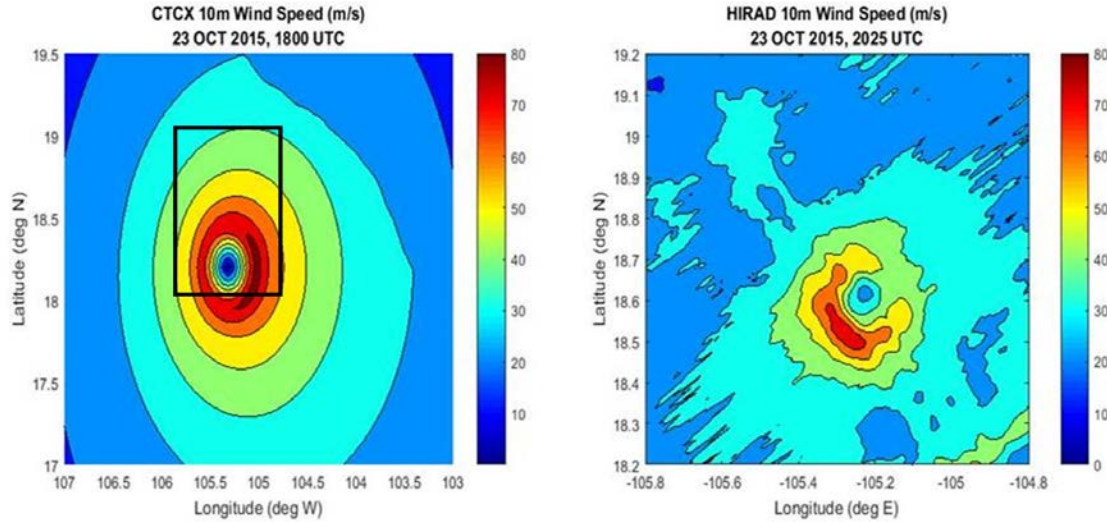
On 22 October (Figure 25), both the CTCX and HIRAD maximum winds are approximately 60 m/s and located to the north-northeast of Patricia's eye. However, note that this maximum wind speed region is only approximately 13 km from the TC central region with HIRAD analyzed wind speeds of 15 m/s (dark blue circular region). By contrast, the maximum wind speed in the CTCX initial conditions is approximately 50 km from the center. Furthermore, the wind speed gradient in the HIRAD observations is extremely large outside of the area of maximum winds. In the CTCX initial conditions, the wind speed decreases much more gradually northeast of the area of maximum winds. Thus, Patricia is analyzed as an extremely compact TC in the HIRAD analysis and a very broad TC in the CTCX analysis.



Left: Wind speed (m/s, color scale on right) at 10 m elevation in the CTCX initial conditions at 1800 UTC 22 October. Right: Surface wind speed (m/s, color scale on right) from the HIRAD analysis of Patricia at 1924 UTC 21 October. The black box indicates the extent of the HIRAD image on the right panel.

Figure 25. Wind speed at 10 m elevation in the CTCX initial conditions at 1800 UTC 22 October and surface wind speed from the HIRAD analysis of Patricia at 1924 UTC 21 October

On the last WB-57 mission into Patricia around 2025 UTC 23 October (Figure 26), the HIRAD analyzed Patricia's maximum winds of 70 m/s at 12 km radius around the western side of the TC, and the CTCX initial conditions had a small region of maximum wind speed of 80 m/s on the east side of the center at a radius of around 25 km. At this time, Patricia was approaching landfall on the western coast of Mexico. The CTCX analysis had a much broader circulation in the north-south direction. Note that the HIRAD analyses did not occur at the same times as the CTCX initialization times. However, the differences in resolution and wind speed gradients are consistent from day to day, and thus time differences of less than three hours do not invalidate this study's evaluation of the comparisons.



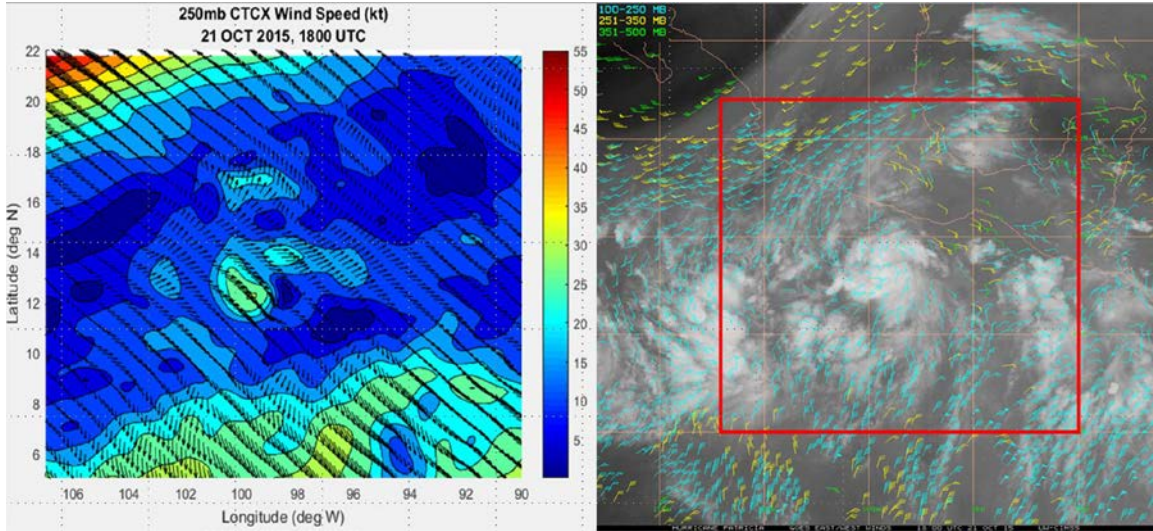
Left: Wind speed (m/s, color scale on right) at 10 m elevation in the CTCX initial conditions at 1800 UTC 23 October. Right: Surface wind speed (m/s, color scale on right) from the HIRAD analysis of Patricia at 2025 UTC 23 October. The black box indicates the extent of the HIRAD image on the right panel.

Figure 26. Wind speed at 10 m elevation in the CTCX initial conditions at 1800 UTC 23 October and surface wind speed from the HIRAD analysis of Patricia at 2025 UTC 23 October

2. Outflow Wind Field Structure

In order to compare Patricia's outflow wind structure in the CTCX initial conditions to observations, the wind speeds at 250 mb in the CTCX model will be compared to Atmospheric Motion Vectors (AMVs) from CIMSS overlaid on infrared GOES satellite imagery. For these comparisons only, CTCX wind speed units have been converted from m/s to kt, as the AMVs indicate wind speed in kt. It is important to note that the outflow layer in CTCX is not part of the initial bogus vortex. Rather, the upper-level winds outside of the core are interpolated from the vortex structure in the GFS model (Doyle et al., 2014). Thus, differences in these initial conditions in the outflow layer may still lead to errors in the CTCX forecast.

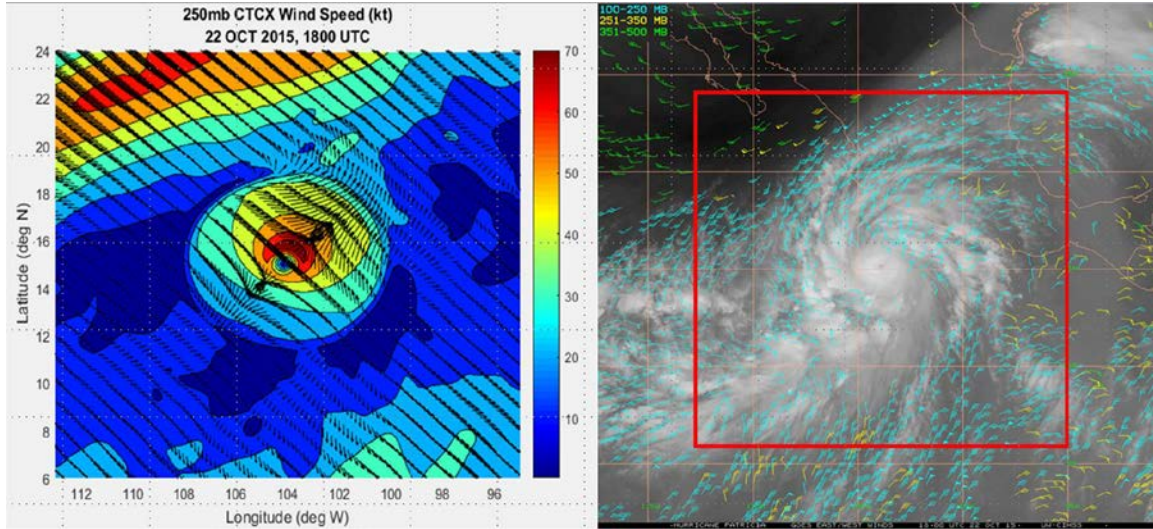
At 1800 UTC 21 October (Figure 27), winds at 250 mb in the CTCX model are consistent with the winds analyzed from the AMVs in all areas except near the western edge of the TC, where CTCX winds are westerly and the AMV analysis indicates that winds in that region are easterly.



The red square indicates the extent of the CTCX image on the left panel.

Figure 27. CTCX wind (kt) at 250 mb (left) and upper-level Atmospheric Motion Vectors (AMVs, kt) overlaid on an infrared satellite image (right) at 1800 UTC 21 October. Right panel source: CIMSS (2017).

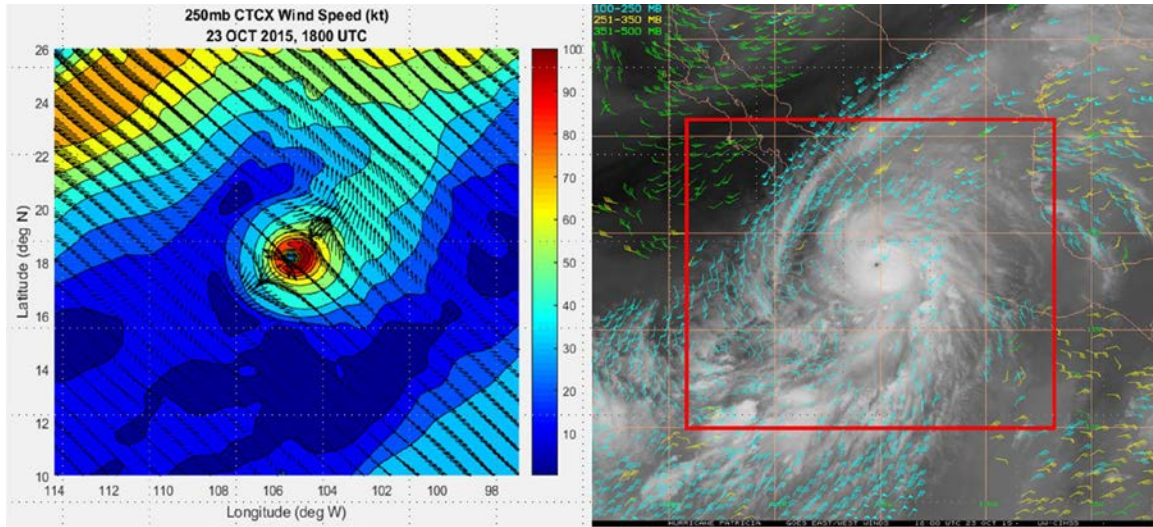
At 1800 UTC 22 October (Figure 28), the 250 mb winds in the CTCX initial conditions depict a poleward outflow jet that is consistent with the AMVs. However, an equatorward jet is not analyzed in the model even though it is very pronounced in the AMVs.



The red square indicates the extent of the CTCX image on the left panel.

Figure 28. CTCX wind at 250 mb (left) and AMVs (right) at 1800 UTC 22 October. Right panel source: CIMSS (2017).

At 1800 UTC 23 October, again there is a poleward jet present in both the CTCX model and the AMVs (Figure 29). However, the weakening equatorward jet indicated in the AMVs is not present in the CTCX analysis. Outside of the bogus vortex in the upper levels, the GFS global model fields are interpolated to match the vortex. Therefore this error is largely due to the 1800 UTC GFS initial model fields.



The red square indicates the extent of the CTCX image on the left panel.

Figure 29. CTCX wind at 250 mb (left) and AMVs (right) at 1800 UTC 23 October. Right pane source: CIMSS (2017).

It is noteworthy that while the CTCX analysis and observed upper-level outflow structure were relatively consistent at 1800 UTC 21 October, the CTCX forecast initialized at that time did not predict the rapid intensification that was about to begin. The CTCX forecast from 1800 UTC 22 October was initialized as Patricia was continuing to intensify, but the initial fields for that CTCX forecast did not contain two outflow jets as observed in the satellite imagery and AMVs. Rappin et al. (2011) noted that both a poleward and an equatorward outflow jet typically precede the development of the most intense TCs. Consequently, it is perhaps not surprising that the CTCX model did not forecast an intense Patricia when the initial conditions did not include the two observed outflow jets.

3. Storm-Relative Wind

Whereas the CTCX and AMV/HIRAD comparisons were conducted utilizing true wind, the following comparisons between the CTCX model and the TCI HDSS observations (Doyle et al., 2017) will be made with the storm-relative adjustments described in chapter III. This ensures that both datasets are valid at the same time and that

Patricia's center position is identical in both datasets. In addition, the CTCX initial conditions were interpolated to the HDSS points.

In order to conduct a quantitative verification of HDSS and CTCX at the HDSS points, all points will be plotted as a function of distance to Patricia's zero-wind center (ZWC) in a series of radial plots. Additionally, cross-section plots of the storm-relative winds will be provided where major wind speed inconsistencies are found between the CTCX initial conditions and HDSS observations.

CTCX error statistics will be calculated in two regions: inside Patricia's core defined as within three times the radius of maximum winds (RMW) and outside the core, where this RMW is from the NHC (USDOC, 2017; available at <http://ftp.nhc.noaa.gov/atcf/archive/2015/bep202015>). Since the CTCX model errors will be averaged in 10 km radial bands, these radii of maximum winds will be rounded to the nearest 10 km. Thus, the inner core is defined to be 160 km at 1800 UTC 21 October, 60 km at 1800 UTC 22 October, and 30 km at 1800 UTC 23 October.

a. 21 October 2015

Patricia's wind structure in the CTCX model initial conditions at 1800 UTC 21 October are compared with HDSS storm-relative wind speed as a function of distance from the TC center (Figures 30–39). At each of the 200 mb, 300 mb, 500 mb, 700 mb, and 850 mb pressure levels, a plot of the HDSS and the CTCX model wind speeds as a function of radius from the zero-wind center (ZWC) will be provided. Additionally, the mean bias (CTCX-HDSS) with radius, averaged in 10 km radial bands is plotted. The Root Mean Square Error (RMSE) as in Figure 18 will be averaged within the inner core and outside the inner core as described above. For example, the 200 mb HDSS and CTCX wind speeds at 1800 UTC 21 October are plotted in Figure 30 and the mean bias is plotted in Figure 31 with the RMSE values in the inset box.

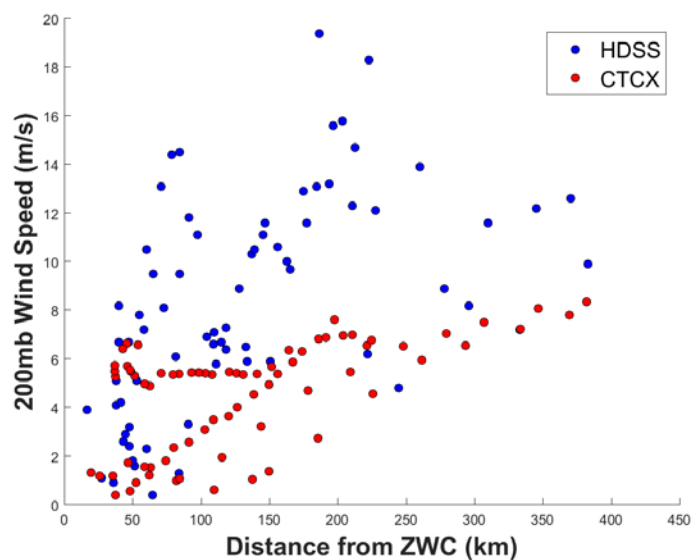


Figure 30. Storm-relative wind speeds from HDSS (blue dots) and CTCX initial conditions (red dots) as a function of distance to Patricia's zero-wind center (ZWC) at 200 mb for 1800 UTC 21 October

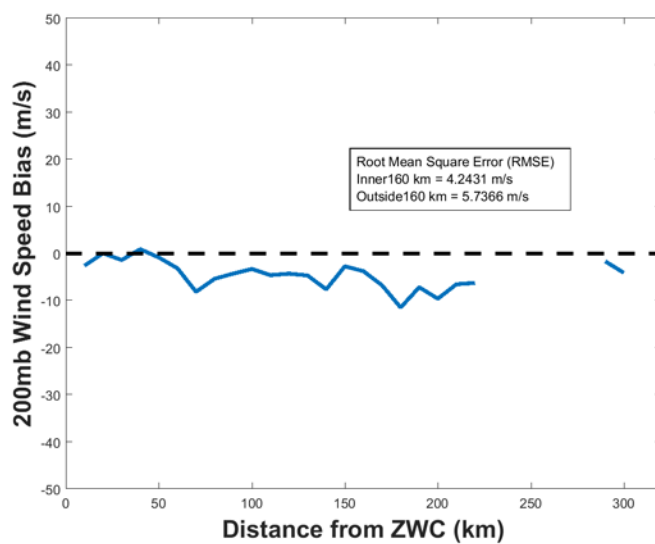


Figure 31. CTCX mean wind speed bias relative to the HDSS wind speeds averaged in 10 km radial bands at 200 mb for 1800 UTC 21 October

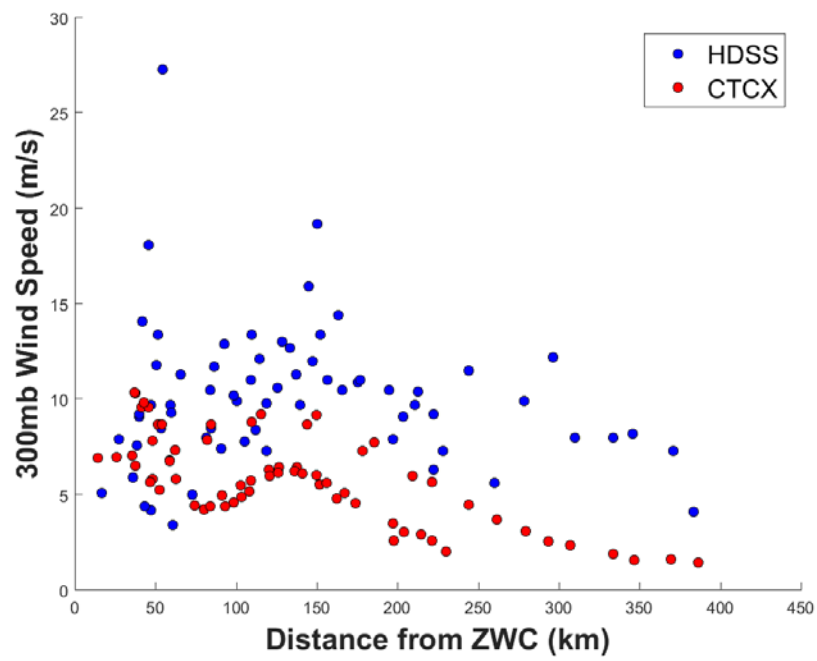


Figure 32. Storm-relative wind speeds as in Figure 30 except at 300 mb for 1800 UTC 21 October

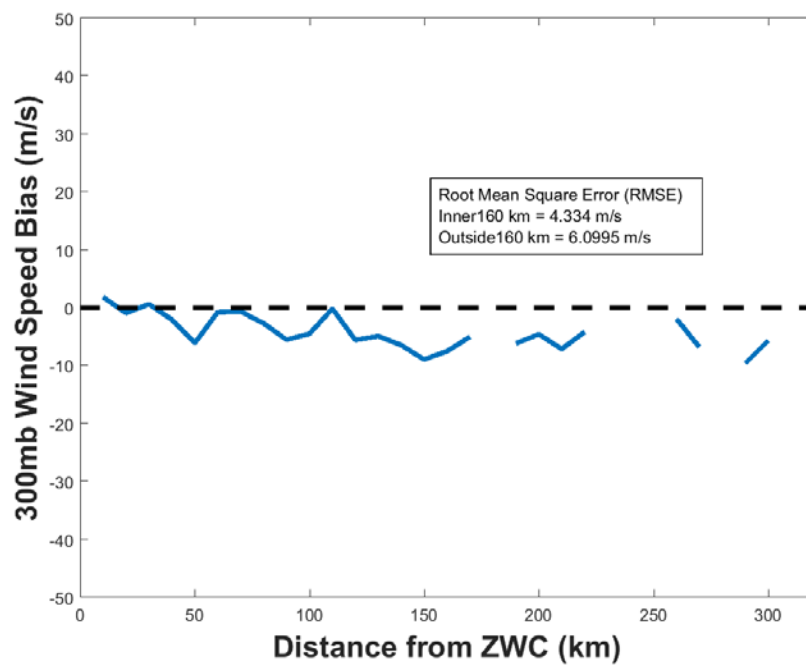


Figure 33. CTCX mean wind speed bias as in Figure 31 except at 300mb for 1800 UTC 21 October

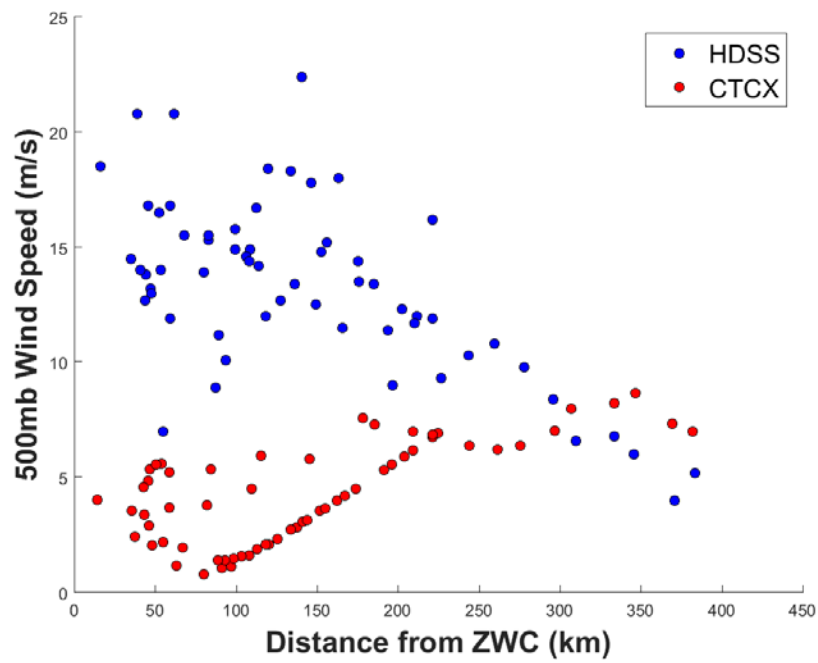


Figure 34. Storm-relative wind speeds as in Figure 30 except at 500 mb for 1800 UTC 21 October

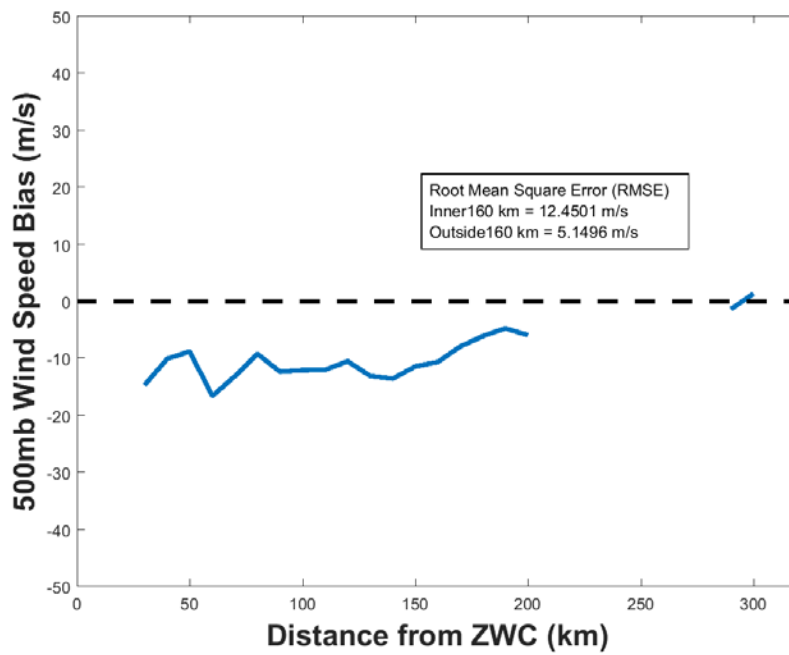


Figure 35. CTCX mean wind speed bias as in Figure 31 except at 500 mb for 1800 UTC 21 October

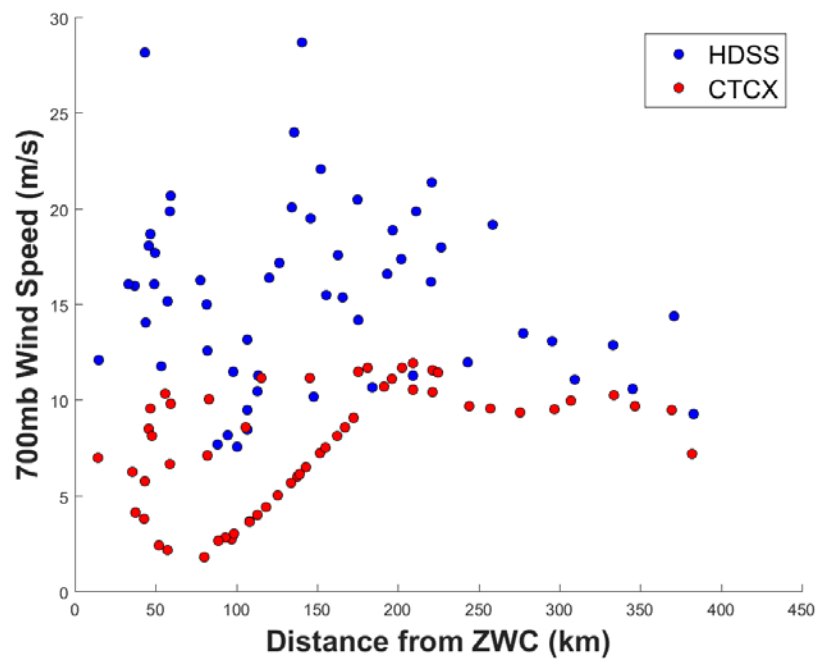


Figure 36. Storm-relative wind speeds as in Figure 30 except at 700 mb for 1800 UTC 21 October

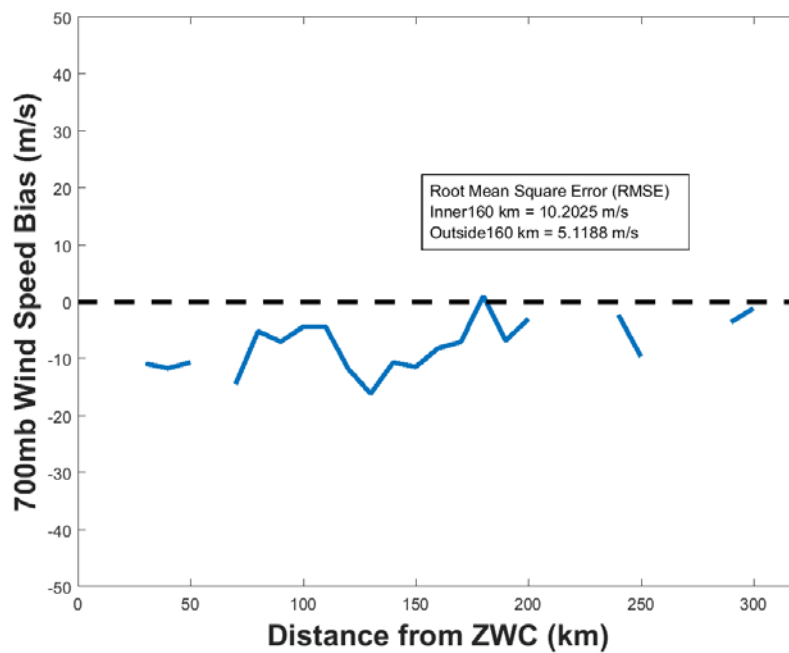


Figure 37. CTCX mean wind speed bias as in Figure 31 except at 700 mb for 1800 UTC 21 October

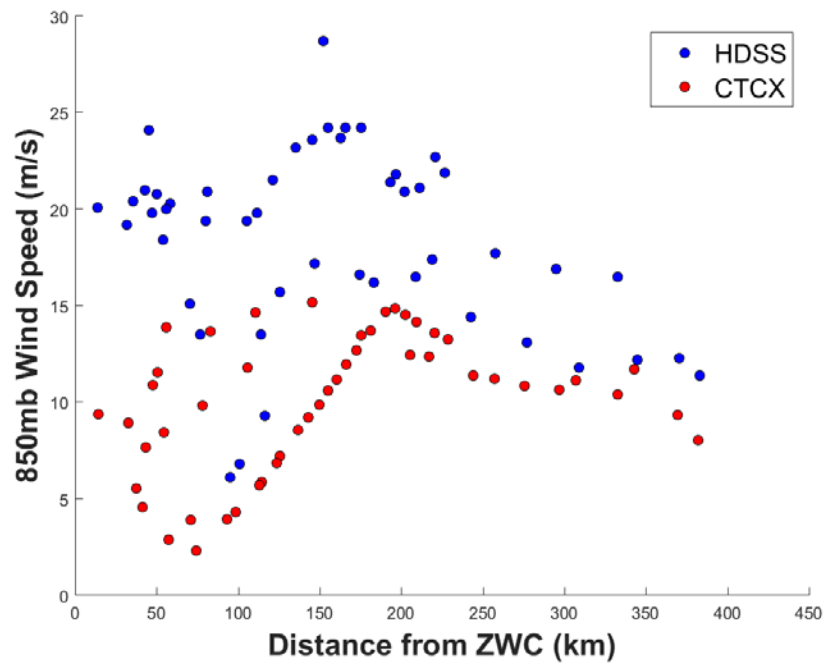


Figure 38. Storm-relative wind speeds as in Figure 30 except at 850 mb for 1800 UTC 21 October

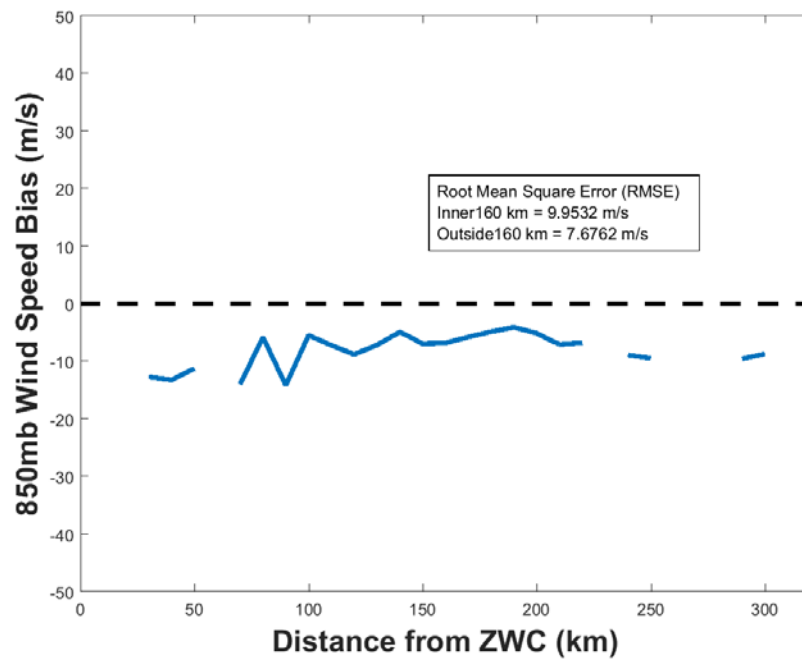


Figure 39. CTCX mean wind speed bias as in Figure 31 except at 850 mb for 1800 UTC 21 October

At 200 mb and 300 mb, the HDSS-observed winds are on average nearly twice the magnitude of winds in the CTCX initial fields. From the AMVs in section B.1 of this chapter, these winds are directed away from the TC center, which indicates that the observed outflow winds above Tropical Storm (TS) Patricia were stronger than the outflow winds in the initial conditions of the CTCX model at 1800 UTC 21 October. At 500 mb, 700 mb, and 850 mb, the CTCX initial conditions (based on the bogus vortex) have linearly increasing wind speeds from 75 km to a radius of approximately 225 km, and the CTCX wind profile has the distinct shape of the modified Rankine bogus vortex with constant wind speeds at larger radii than 225 km. By contrast, the HDSS observations have increasing wind speeds inward from 350 km to a peak around 150 km and a separate group of maximum winds at a radius of approximately 50 km. Clearly at this TS stage the CTCX bogus vortex does not well-represent the vortex wind structure of Patricia.

The CTCX initial conditions at 1800 UTC 21 October exhibit a negative bias at all five pressure levels examined, and especially inside the storm core. This indicates that CTCX was initialized too weak at this time, which would certainly have contributed to the forecast intensity errors displayed in Figure 11.

b. 22 October 2015

Similar wind speed comparisons will be evaluated for the 1800 UTC 22 October 2015 mission HDSS soundings (Figures 40–50). As discussed previously, in-situ HDSS observations below 300 mb in the eye-wall region were sparse at this time due to dropsonde drift when the Patricia’s intensity was near 110 kt (56.6 m/s). However, a NOAA aircraft reconnaissance mission (Doyle et al., 2017) passed through the center and eye-wall at 700 mb at 1724 UTC. This dataset has been adjusted to the 1800 UTC valid time and storm-relative coordinates by the same method as for the HDSS data and described in Chapter III and is included on the comparison plots for 700 mb.

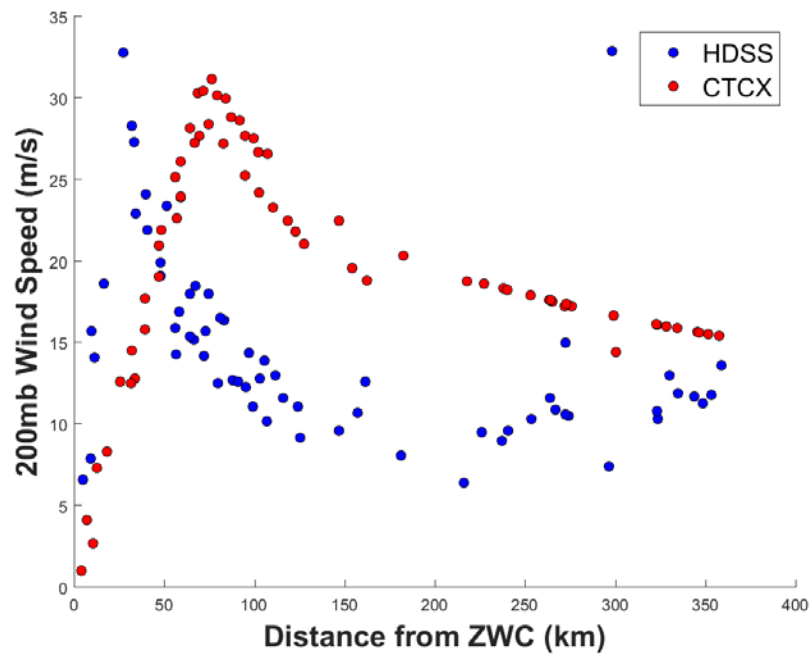


Figure 40. Storm-relative wind speeds as in Figure 30 except at 200 mb for 1800 UTC 22 October

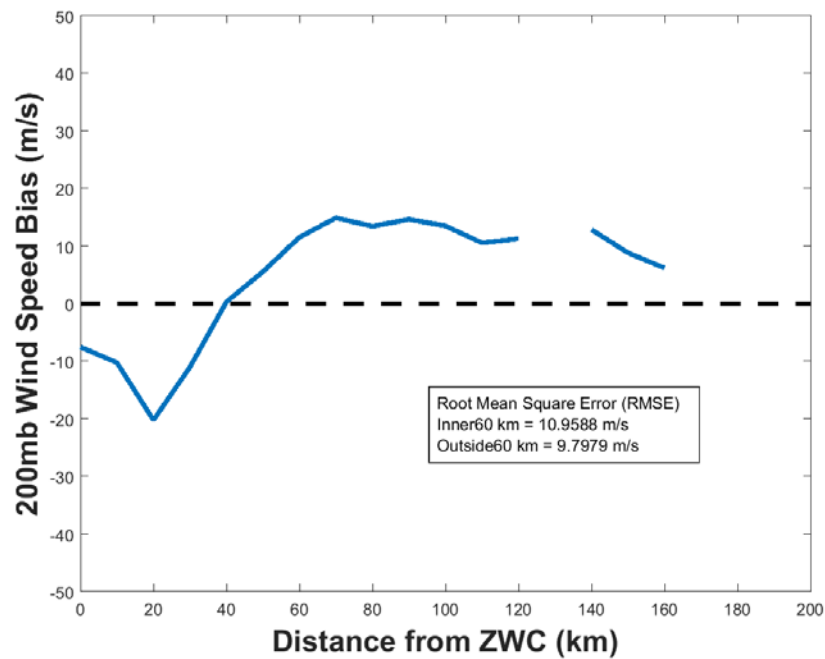


Figure 41. CTCX mean wind speed bias as in Figure 31 except at 200 mb for 1800 UTC 22 October

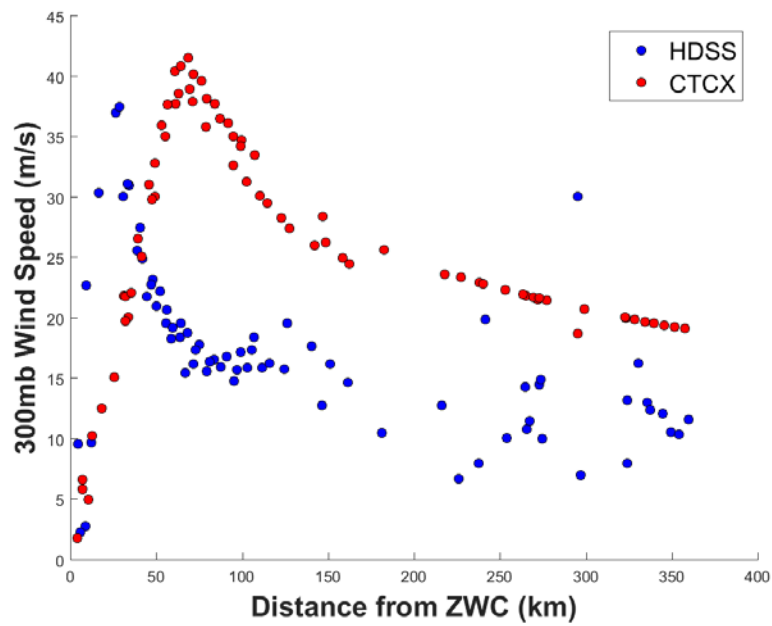


Figure 42. Storm-relative wind speeds as in Figure 30 except at 300 mb for 1800 UTC 22 October

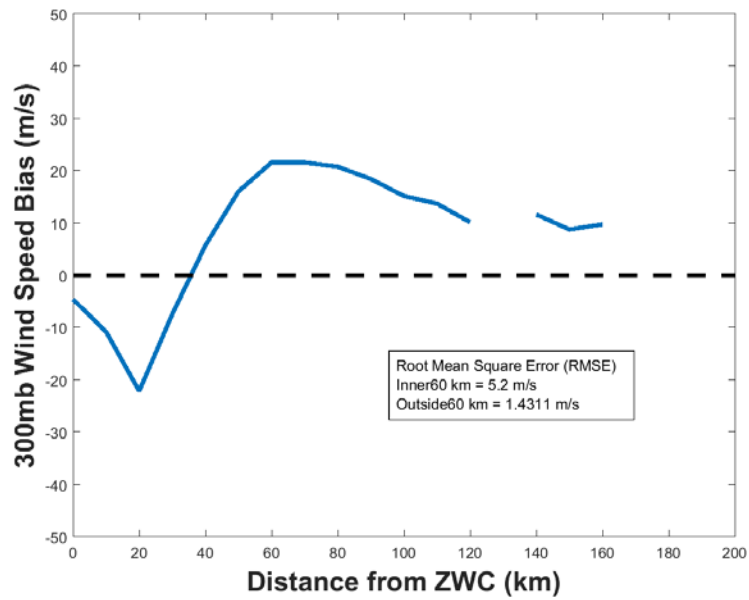


Figure 43. CTCX mean wind speed bias as in Figure 31 except at 300 mb for 1800 UTC 22 October

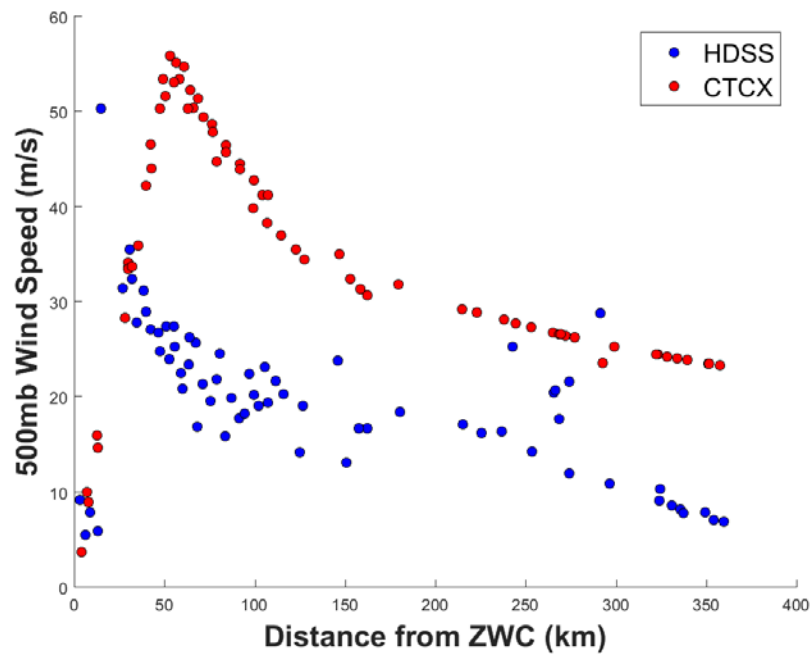


Figure 44. Storm-relative wind speeds as in Figure 30 except at 500 mb for 1800 UTC 22 October

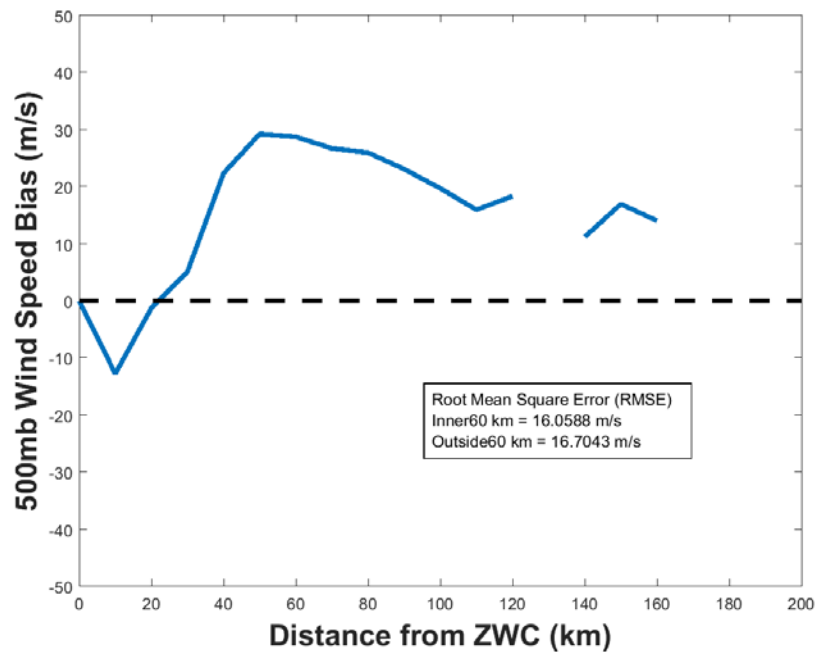


Figure 45. CTCX mean wind speed bias as in Figure 31 except at 500 mb for 1800 UTC 22 October

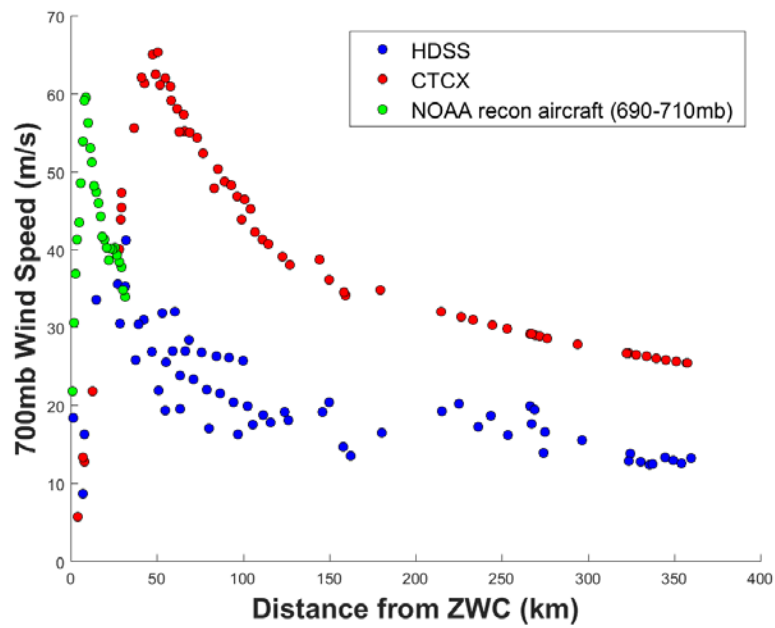


Figure 46. Storm-relative wind speeds as in Figure 30 except at 700 mb for 1800 UTC 22 October

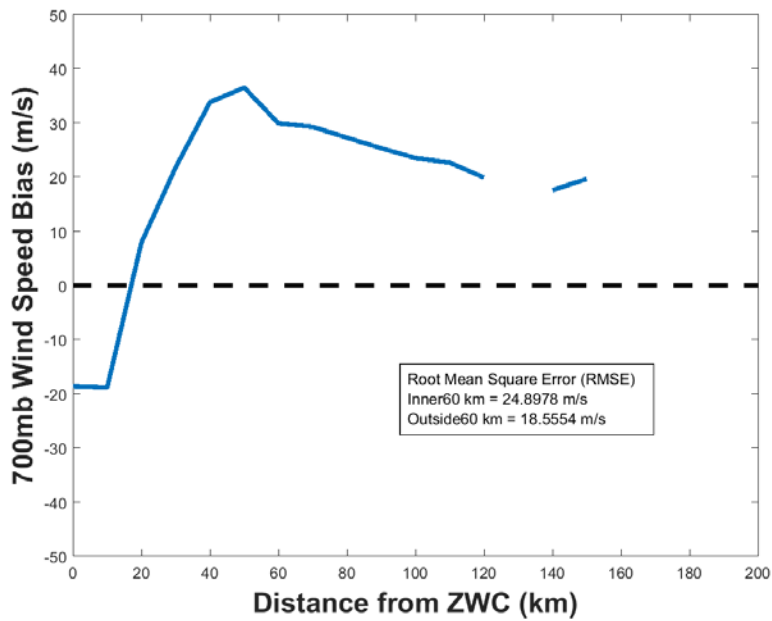


Figure 47. CTCX mean wind speed bias as in Figure 31 except at 700 mb for 1800 UTC 22 October

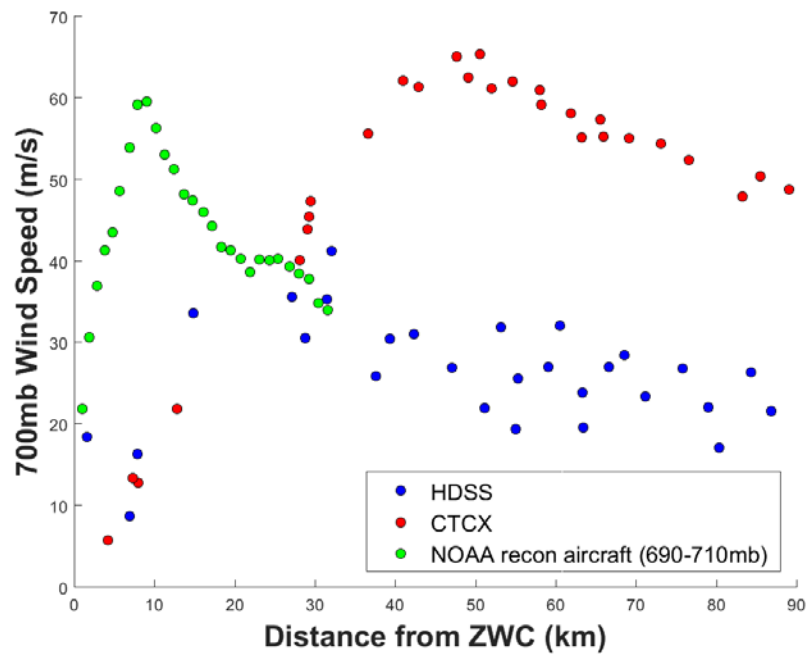


Figure 48. Storm-relative wind speeds as in Figure 30 except at 700 mb for 1800 UTC 22 October (zoomed to display only the inner 90 km)

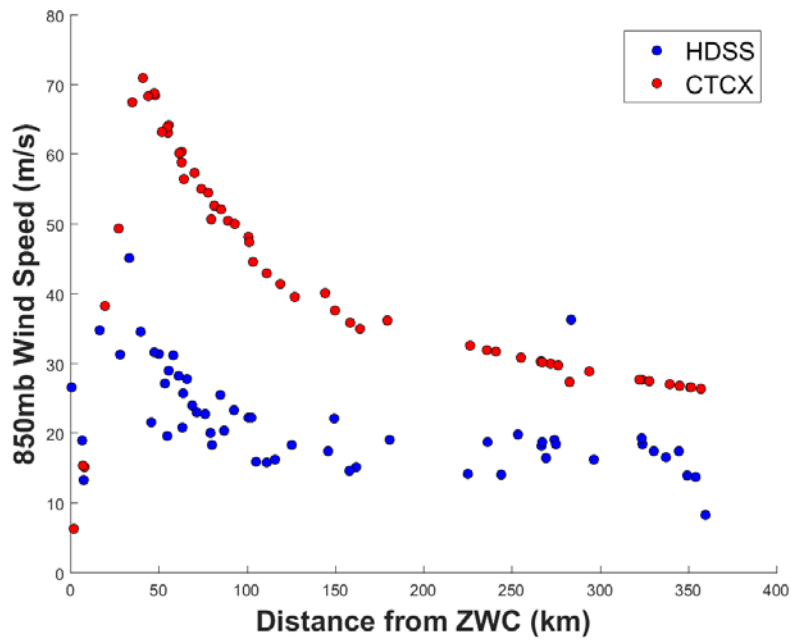


Figure 49. Storm-relative wind speeds as in Figure 30 except at 850 mb for 1800 UTC 22 October

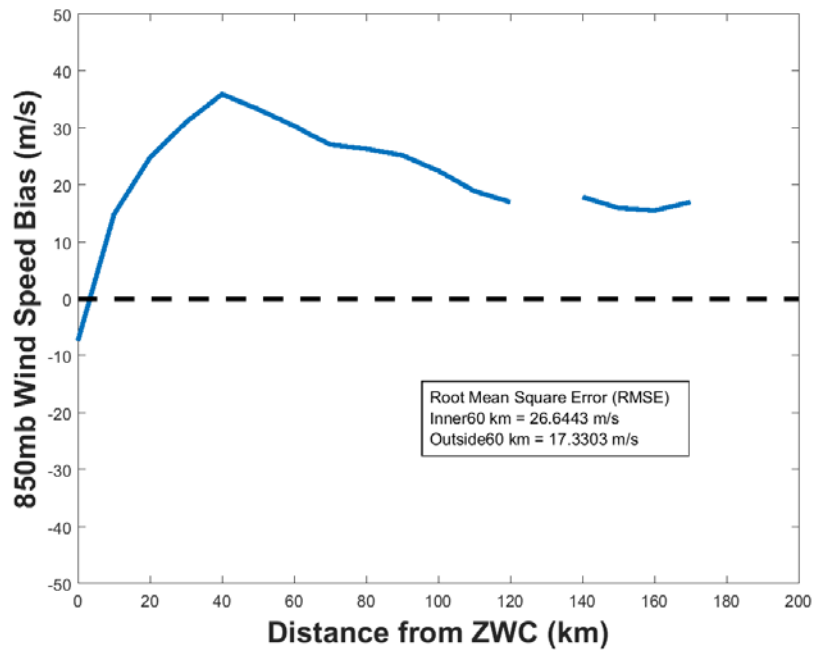


Figure 50. CTCX mean wind speed bias as in Figure 31 except at 850 mb for 1800 UTC 22 October

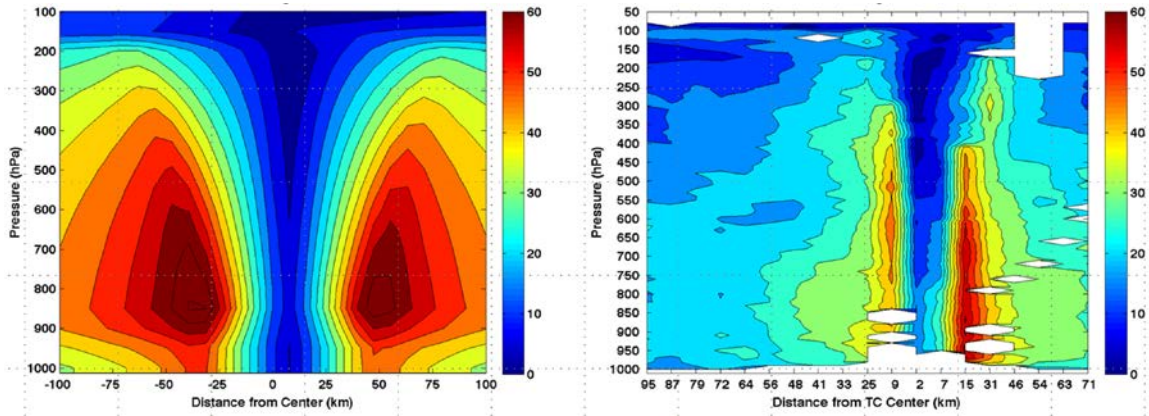
At 200 mb (Figures 40 and 41), the CTCX wind profile is a Rankine-type vortex extending from 15 m/s at 350 km inward to a maximum wind speed of 32 m/s at 70 km radius. By contrast, the outer winds speeds in the HDSS observations are approximately constant at 10 to 15 m/s beyond 100 km radius. Inside that radius, a sharply peaked wind profile with a maximum wind speed of 33 m/s at 20 km is observed from the HDSS dropsondes. A similar difference in wind profiles occurs at 300 mb (Figures 42 and 43). The CTCX Rankine vortex profile has 20 m/s winds at 350 km and a maximum wind speed of 42 m/s at 60 km. The HDSS wind speeds are widely scattered between 7 m/s and 17 m/s outside of 100 km radius, but as at 200 mb, a sharply peaked wind profile with maximum winds of 37 m/s at 20 km radius is observed by the HDSS sondes. Thus, the CTCX vertical wind profile at the upper levels is much broader and much stronger beyond 30 km radius, but weaker than the HDSS observations inside 30 km.

At 500 mb (Figures 44 and 45), the CTCX Rankine-type wind profile is consistently about 15 m/s larger than the HDSS profile from 100 km to 350 km radius. The CTCX has a maximum wind of 55 m/s at 50 km, and a single HDSS observation near a 10 km radius observed a wind speed of 50 m/s.

As previously mentioned, a NOAA aircraft reconnaissance mission provided additional validation of the inner-core wind structure at 700 mb (Figures 46-48). These NOAA wind observations validate the HDSS observations of an intense Hurricane Patricia with 60 m/s winds near 10 km radius even at 700 mb. By contrast, the CTCX vortex has stronger outer-circulation winds and a maximum wind located at a radius of approximately 50 km. The difference between the CTCX Rankine vortex wind profile and the HDSS observations inside a 150 km radius is even larger (20 m/s) at 850 mb (Figures 49 and 50). That CTCX profile has a maximum of 70 m/s at 30 km radius. No validation of the maximum winds is available from the HDSS soundings, which were not successful in the eye-wall region in such a compact hurricane as Patricia.

Note that the error in the CTCX model's radius of maximum winds (RMW) is consistent at all of the analyzed pressure levels. The difference in the magnitude of maximum winds between CTCX and in-situ observations is typically small, but the much

larger RMW in the CTCX model leads to large differences in the in radial structure of the tangential wind, as shown in Figure 51 (provided courtesy of Mary S. Jordan).



Y-axis indicates decreasing pressure. X-axis indicates distance from Patricia's ZWC (color scale on right of each image). Image courtesy of Mary S. Jordan.

Figure 51. CTCX (left panel) storm-relative winds at 1800 UTC 22 October and HDSS (right panel) storm-relative winds from 1815–1828 UTC 22 October

HDSS observations and NOAA aircraft data indicate that the radius of Patricia's eye is between 10 km and 20 km, with a large gradient (40 m/s per 90 km at 700 mb) between the location of maximum winds and 100 km radius. NHC's radius of maximum winds at 1800 UTC 22 October is 18.52 km (Kimberlain et al., 2016), which is a slightly larger radius than observed in the HIRAD analysis and HDSS observations. Beyond 100 km radius from the center, the wind speed gradient is smaller.

The vortex inserted into the CTCX model has an eye-wall radius between 45 km and 65 km, and beyond the eye-wall the wind speed gradient is not as sharp as in the observations. This results in the CTCX model exhibiting a negative wind speed bias in the core and a large positive bias outside the core. The large positive bias may also be due to the assumption of a modified Rankine vortex decay, and further study will be necessary to determine if reality may have been different for Patricia.

As opposed to 21 October, at 1800 UTC 22 October the CTCX was not initialized too weak, but instead it was initialized with a bogus vortex that has a larger RMW and

outer wind field. Both the HIRAD and HDSS comparisons support this conclusion, and this broader vortex at the initial time is hypothesized to have contributed to the CTCX model forecast from 1800 UTC 22 October to under-forecast peak intensity by 45 kt (23.2 m/s).

c. 23 October 2015

Similar wind speed comparisons will be evaluated for the 1800 UTC 23 October HDSS mission (Figures 52–62). As before, NOAA aircraft reconnaissance mission data will be used to supplement the HDSS data at 700 mb. Patricia’s intensity at this time was approximately 160 kt (82.3 m/s) and rapidly decreasing.

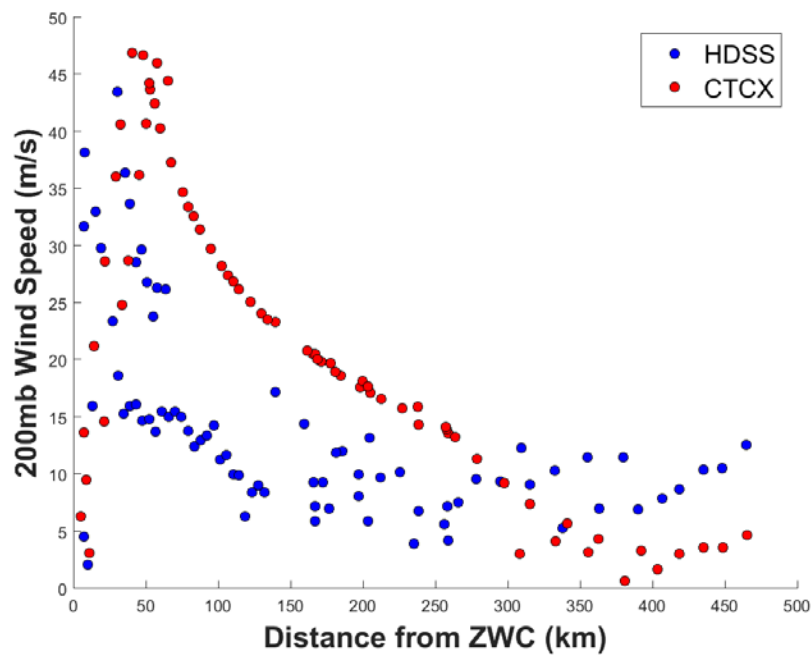


Figure 52. Storm-relative wind speeds as in Figure 30 except at 200 mb for 1800 UTC 23 October

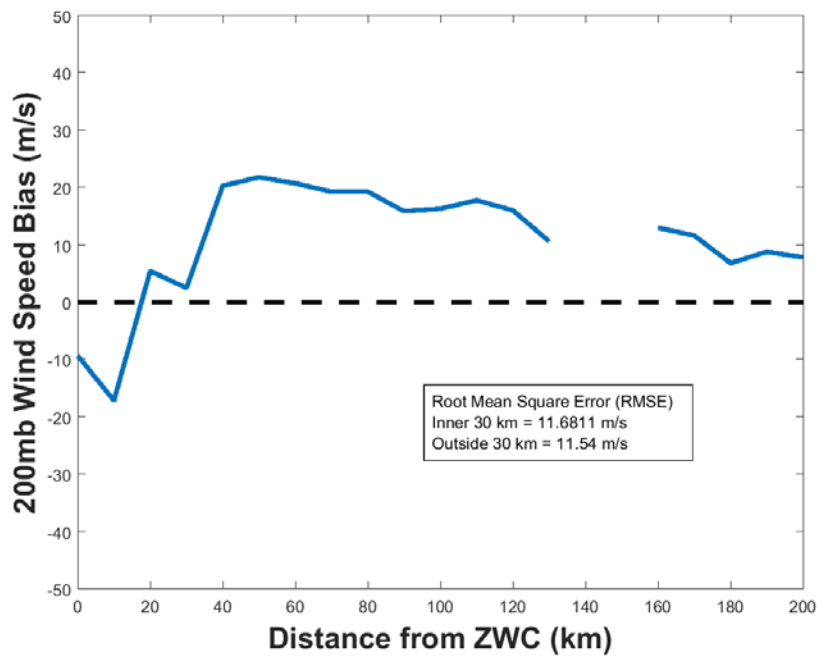


Figure 53. CTCX mean wind speed bias as in Figure 31 except at 200 mb for 1800 UTC 23 October

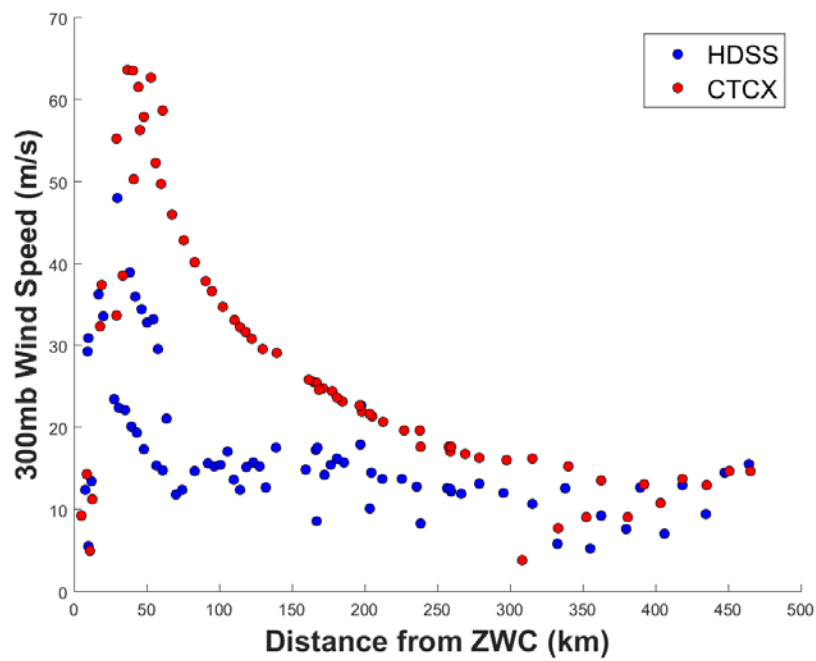


Figure 54. Storm-relative wind speeds as in Figure 30 except at 300 mb for 1800 UTC 23 October

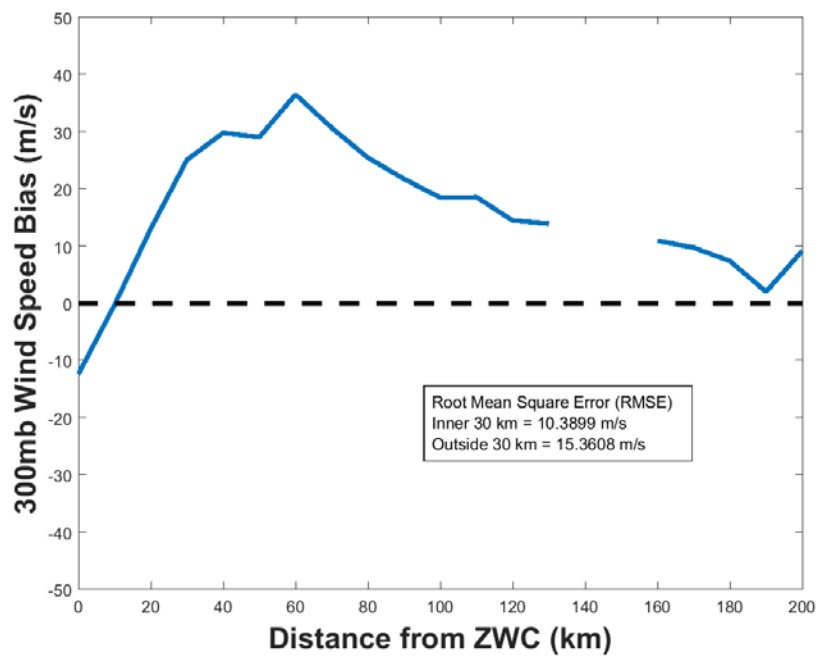


Figure 55. CTCX mean wind speed bias as in Figure 31 except at 300 mb for 1800 UTC 23 October

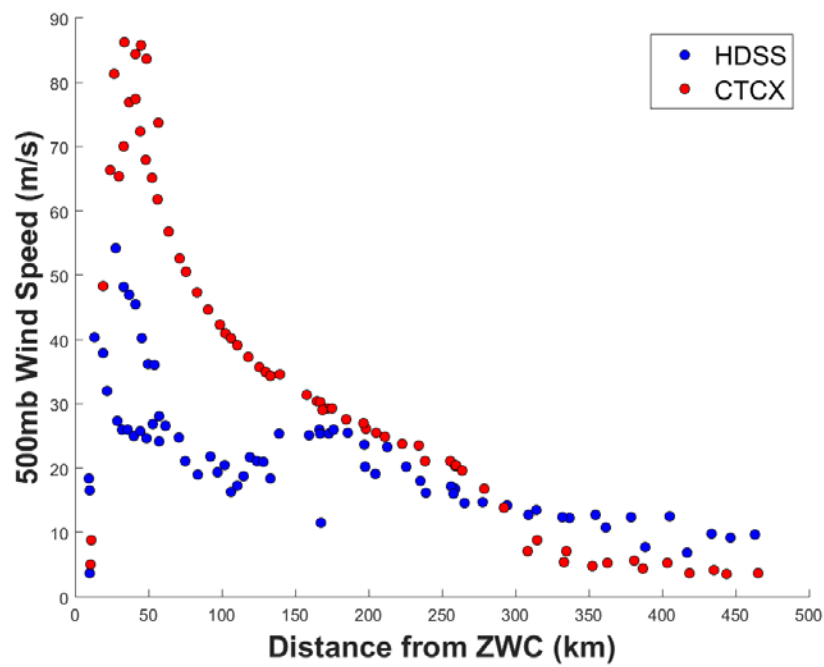


Figure 56. Storm-relative wind speeds as in Figure 30 except at 500 mb for 1800 UTC 23 October

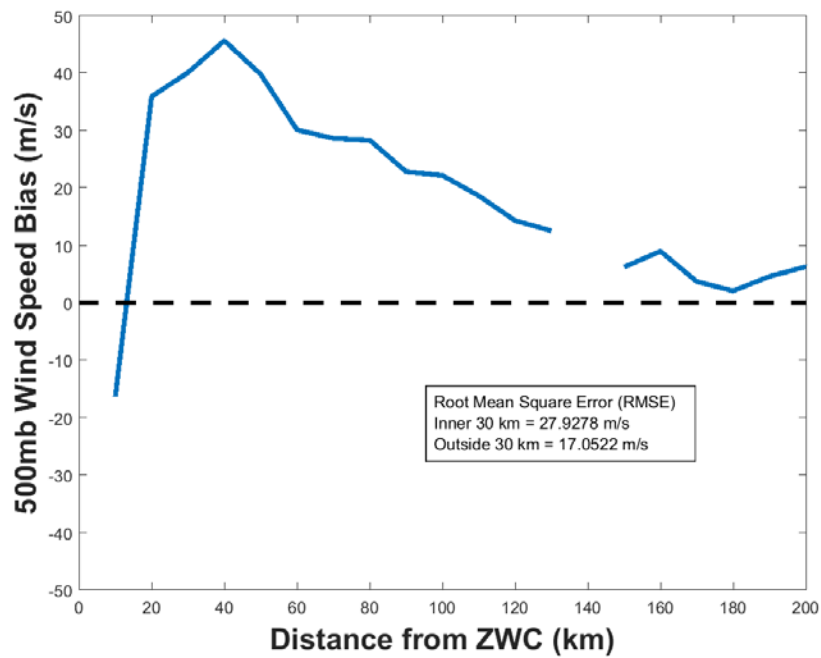


Figure 57. CTCX mean wind speed bias as in Figure 31 except at 500 mb for 1800 UTC 23 October

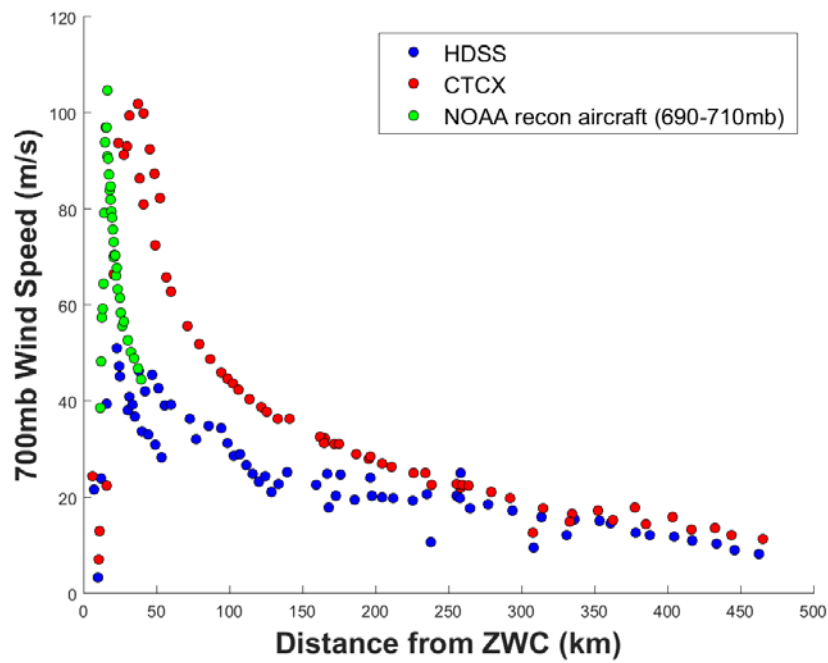


Figure 58. Storm-relative wind speeds as in Figure 30 except at 700 mb for 1800 UTC 23 October

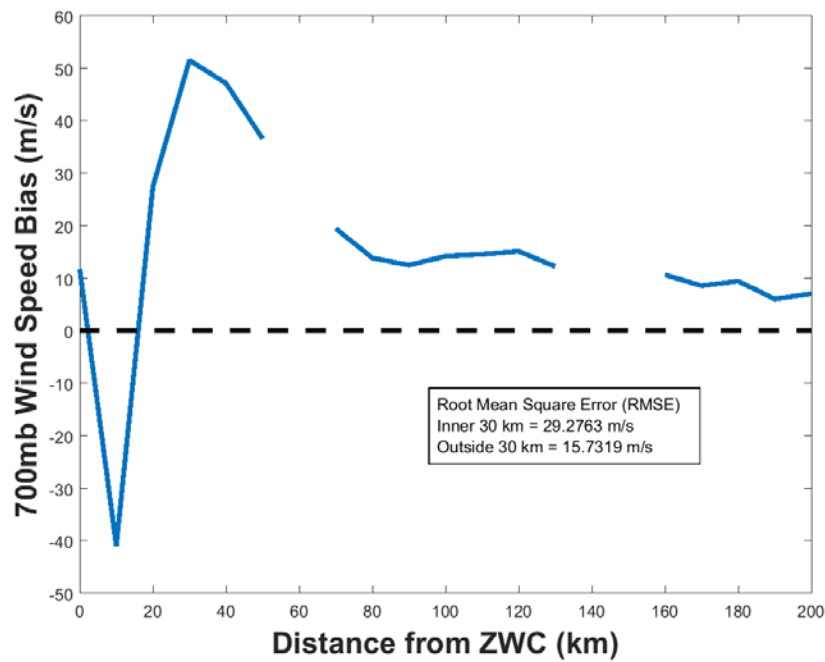


Figure 59. CTCX mean wind speed bias as in Figure 31 except at 700 mb for 1800 UTC 23 October

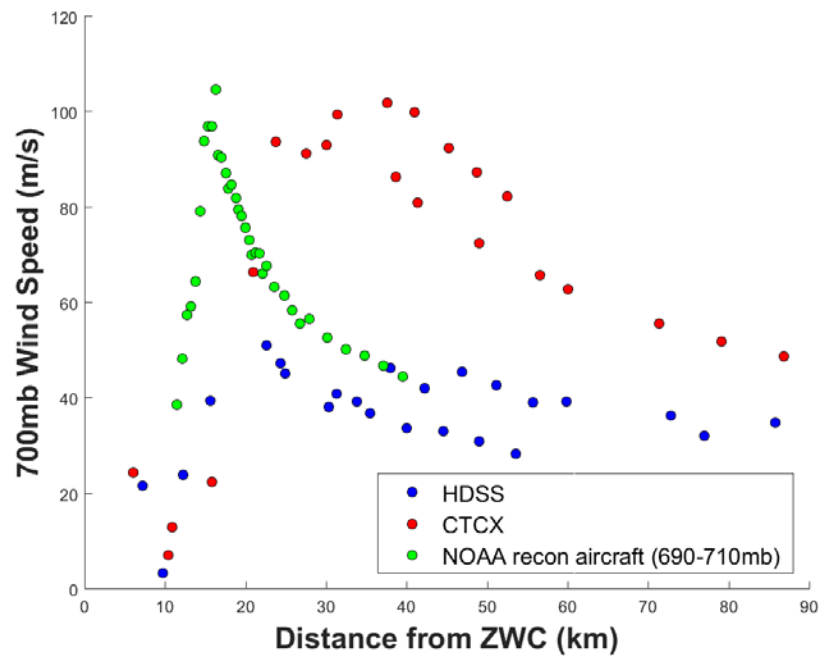


Figure 60. Storm-relative wind speeds as in Figure 30 except at 700 mb for 1800 UTC 23 October (zoomed to display only the inner 90 km)

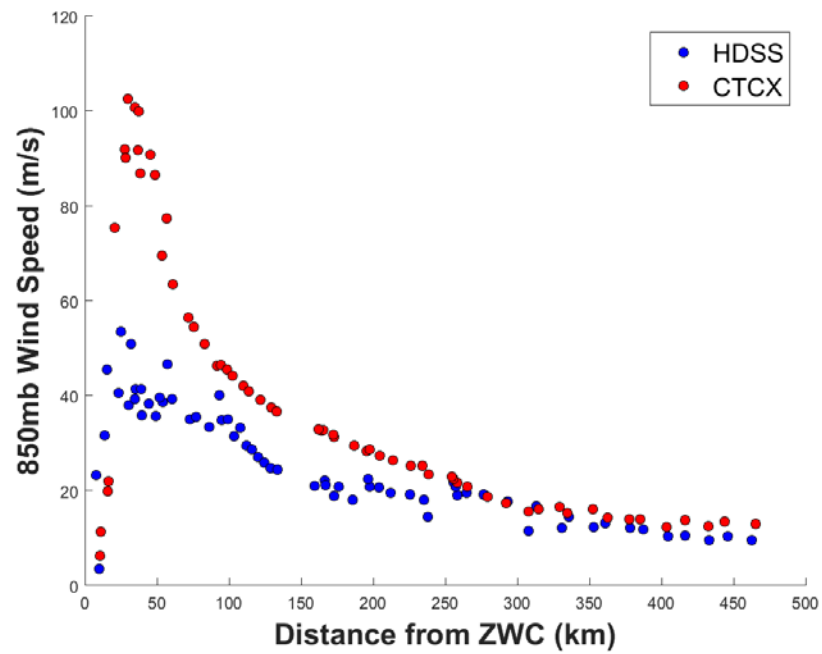


Figure 61. Storm-relative wind speeds as in Figure 30 except at 850 mb for 1800 UTC 23 October

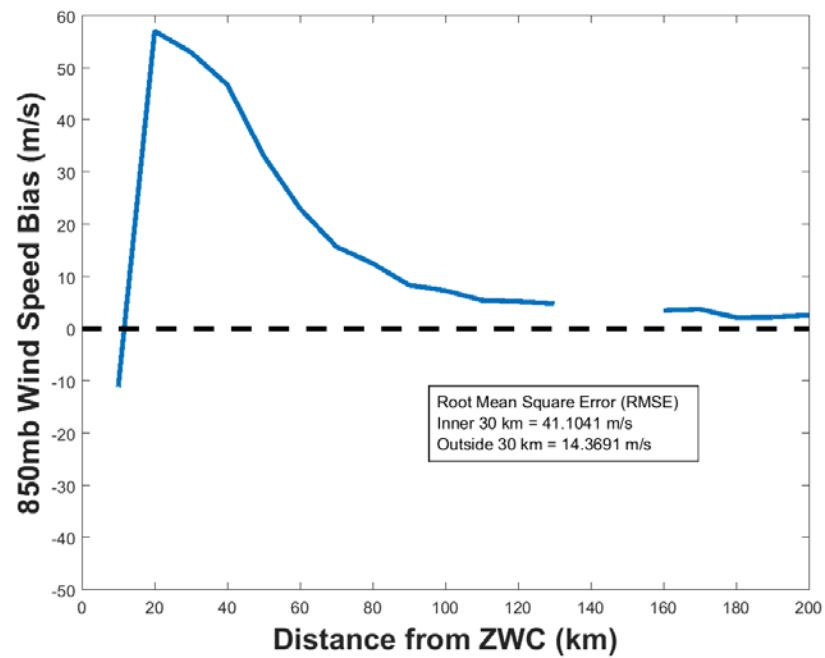


Figure 62. CTCX mean wind speed bias as in Figure 31 except at 850 mb for 1800 UTC 23 October

The 200 mb CTCX wind profile (Figure 52) is again a Rankine-type profile with near-zero storm-relative wind speeds at 350 km and a maximum wind of 47 m/s at about 30 km radius. By contrast, the HDSS outer vortex wind structure beyond 100 km is relatively flat at about 5 to 10 m/s. However, a quite steep increase in wind speed occurs within 100 km with peak wind speeds of 43 m/s near 25 km radius. The 300 mb CTCX wind profile (Figure 54) has its maximum winds at about 50 km radius, with a magnitude around 64 m/s. As was the case at 200 mb, the HDSS outer wind structure outside 100 km is quite flat at 10 m/s. However, the inner-core vortex structure is not well defined by the HDSS dropsondes with only a single data point indicating 47 m/s winds at 30 km radius. Due to the Rankine-type inward increase in wind speed of the 200 mb and 300 mb CTCX analysis versus the flat HDSS winds extending inward, the CTCX winds have a very large mean bias outside of 20 km radius.

It is noteworthy that the 500 mb outer vortex structure from 150 km to 450 km of the CTCX model initial analysis agrees very well with the HDSS wind observations (Figure 56). However, the CTCX wind profile then rapidly increases inward to a maximum of 86 m/s at 30 km radius. The HDSS wind profile has a relative maximum at 150 km that has some characteristics of a secondary eye-wall. As at 300 mb, the 500 mb inner-core maximum is not well-defined by the HDSS dropsondes, as the maximum wind speed is only 54 m/s at 25 km radius.

The availability of NOAA reconnaissance aircraft wind observations at 700 mb is critical for extending the HDSS wind profile inward to the RMW at 12 km with a speed of 106 m/s (Figures 58 and 60). Such a tiny eye region was not able to be observed by HDSS dropsondes deployed from 60,000 ft (18,288 m). As shown in the zoomed-in plot (Figure 60), the largest wind speed measured by the HDSS was 51 m/s at 20 km radius. Although the CTCX Rankine vortex wind structure has a good maximum wind speed of 102 m/s, the radial gradient outside the RMW for the CTCX is not nearly as large as the radial gradient of the NOAA aircraft observations. Also note that the radius of maximum winds (RMW) observed by HDSS dropsondes and the NOAA aircraft missions at 700 mb slightly increased from 10 km at 1800 UTC 22 October to around 12 km at 1800 UTC 23 October. By contrast, the official NHC RMW estimate at the ocean surface decreased

from 10 n mi to 5 n mi (18.52 km to 9.26 km) during the same time period, indicating that the inner-core definition used in this study of three times the NHC RMW may not be the ideal inner-core definition for future research of Hurricane Patricia on 22 and 23 October.

The CTCX initial wind profile at 850 mb (Figure 61) closely resembles the CTCX profile at 700 mb with a maximum wind speed of 102 m/s near 25 km radius. Again, the eye-wall region at 850 mb is not defined by the HDSS dropsondes, as the maximum wind speed of 53 m/s near 15 km radius is clearly a large under-estimate for an intensity of 160 kt (82.3 m/s) at this time.

C. GEOPOTENTIAL HEIGHT

Having examined the comparison of the radial structure of tangential wind between HDSS and CTCX, the mass field (potential temperature and geopotential height) is examined in the next two sections. Understanding the balance between tangential wind, potential temperature, and geopotential height in a TC vortex is instrumental to understanding the evolution of a TC's structure (Willoughby et al., 2006). In the axisymmetric limit, the mass field in real hurricanes largely satisfies the gradient wind and hydrostatic balance equations (Willoughby, 1990). That is, a vortex has a corresponding balanced geopotential and temperature field for a given tangential velocity field. Thus, the mass field in terms of the geopotential height and potential temperature fields will be examined in the next two sections to determine the correspondence to the wind fields described in the previous section. If the tangential velocity field is incorrect, the mass field is likely to be incorrect as well. The set of equations in Figure 63 describe this balance in radius and pressure coordinates (Hendricks and Peng, 2012), beginning with the gradient wind balance, then the hydrostatic balance, and finally the vortex thermal wind balance.

$$\frac{\partial \Phi}{\partial r} = \frac{v^2}{r} + fv$$

$$\frac{\partial \Phi}{\partial p} = \frac{-RT}{p}$$

$$\frac{\partial v}{\partial p} \left(\frac{2v}{r} + f \right) = \frac{-R}{p} \frac{\partial T}{\partial r}$$

Gradient wind balance (top), hydrostatic balance (middle), and vortex thermal wind balance (bottom), where Φ is geopotential, v is tangential velocity, f is the Coriolis parameter, r is the radius from the TC center, p is air pressure, R is the gas constant for dry air, and T is air temperature.

Figure 63. Equations used in the geopotential height and potential temperature balance studies. Source: Hendricks and Peng (2012).

Given the wind field in cylindrical coordinates in the CTCX model, the mass field is determined by solving the nonlinear balance equation for the geopotential, and then assuming the hydrostatic balance, the temperature field is calculated (Hodur, 1997; Doyle et al., 2014). The HDSS geopotential height and potential temperature observations are expected to include both balanced and unbalanced components of the mass field. Understanding the balance between tangential wind, potential temperature, and geopotential height in a TC vortex is instrumental to understanding the evolution of a TC's structure (Willoughby et al., 2006). The HDSS velocity vectors have not yet been decomposed into radial and tangential components about the ZWC. Since the lower-troposphere winds in Patricia are likely to be mostly tangential, the wind speeds in the previous section will be used as a proxy for the tangential wind components below 500 mb.

1. 21 October 2015

The HDSS observations of Patricia's geopotential heights will be compared to the heights in the initial conditions in the CTCX model as a function of radius from the ZWC, and will occur at the same five pressure levels as in the previous section. The following are valid at 1800 UTC 21 October 2015 (Figures 64–73). Once again, all datasets have been adjusted to the same valid time and are in storm-relative coordinates assuming axisymmetric fields.

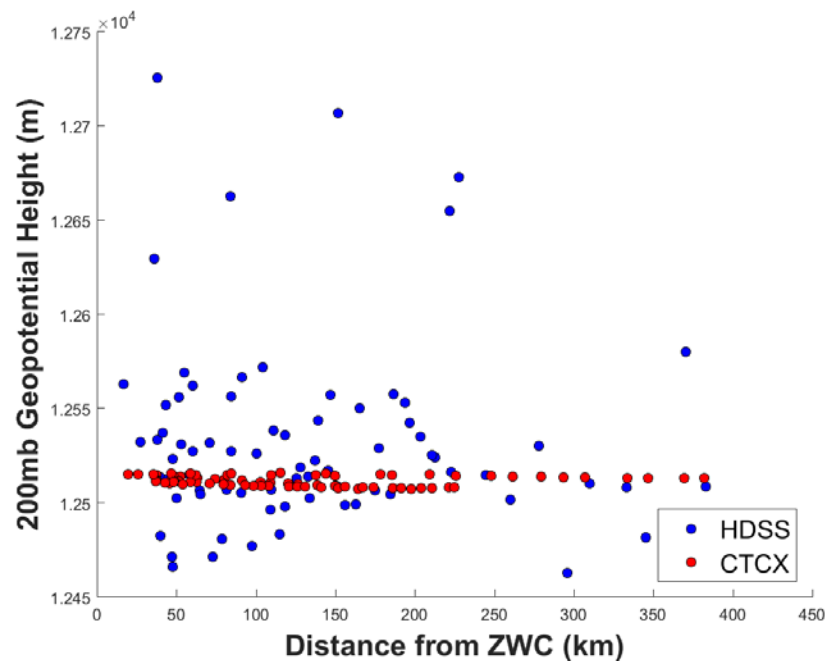


Figure 64. Geopotential heights from HDSS (blue dots) and CTCX initial conditions (red dots) as a function of distance to Patricia's zero-wind center (ZWC) at 200 mb for 1800 UTC 21 October

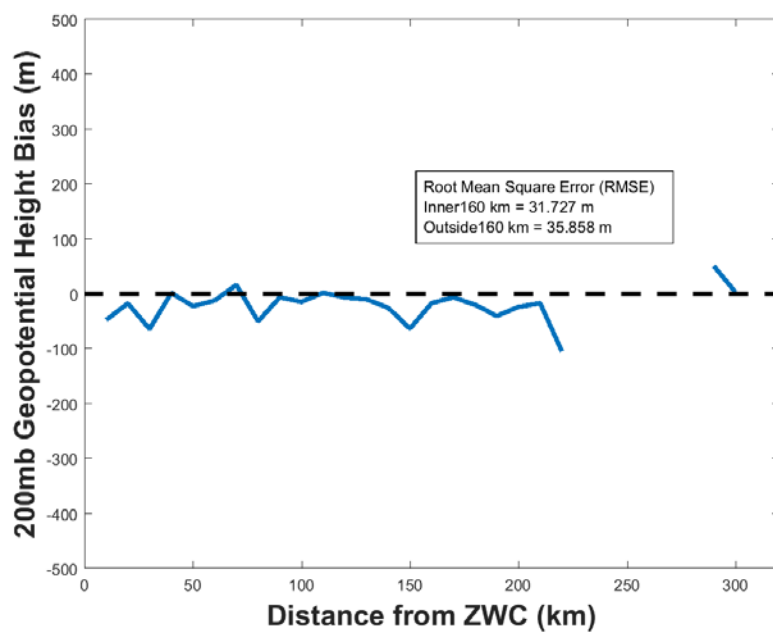


Figure 65. CTCX mean geopotential height bias relative to HDSS observations averaged in 10 km radial bands at 200 mb for 1800 UTC 21 October

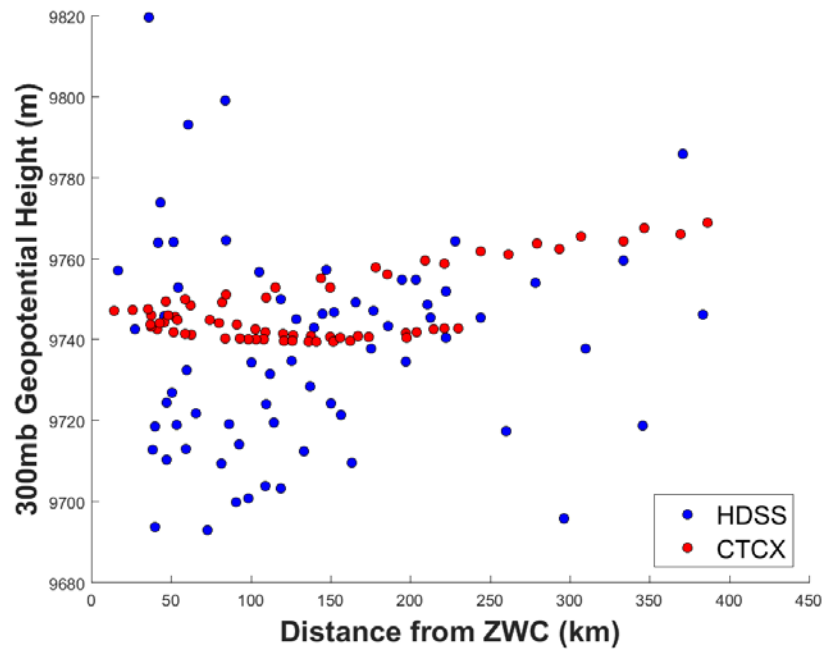


Figure 66. Geopotential heights as in Figure 64 except at 300 mb for 1800 UTC 21 October

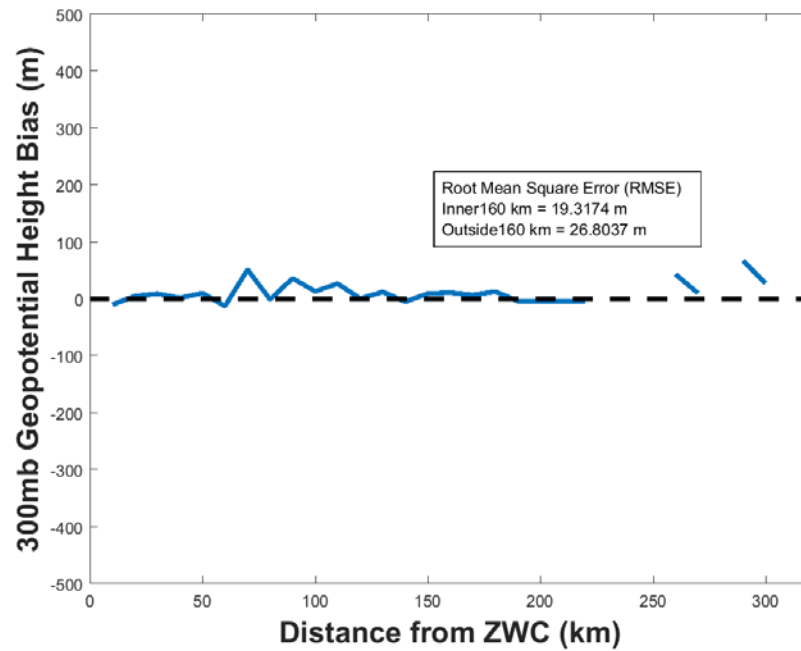


Figure 67. CTCX mean geopotential height bias as in Figure 65 except at 300 mb for 1800 UTC 21 October

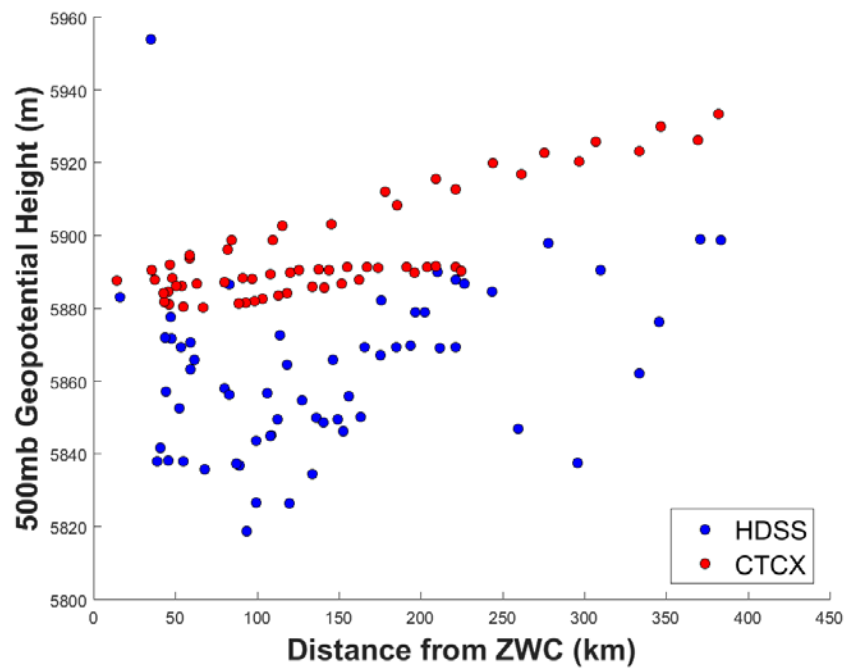


Figure 68. Geopotential heights as in Figure 64 except at 500 mb for 1800 UTC 21 October

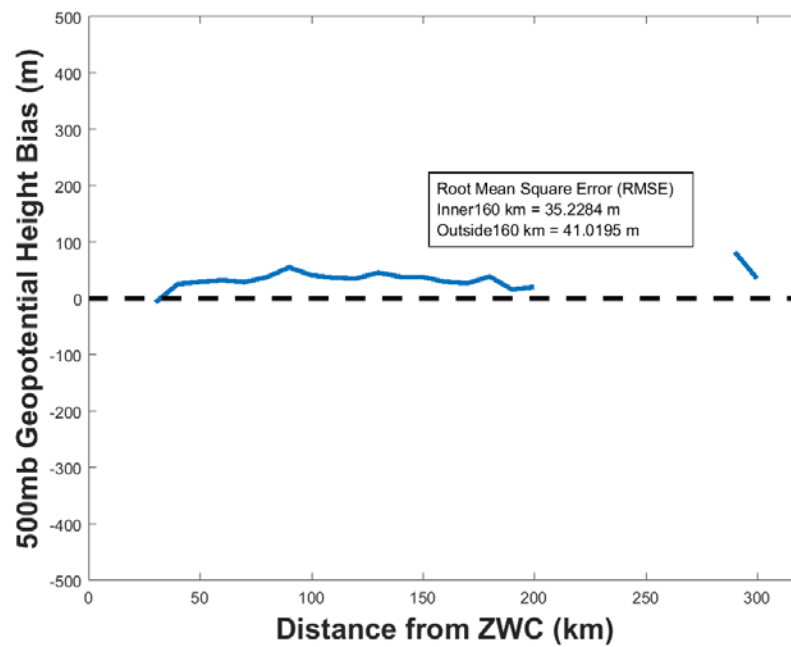


Figure 69. CTCX mean geopotential height bias as in Figure 65 except at 500 mb for 1800 UTC 21 October

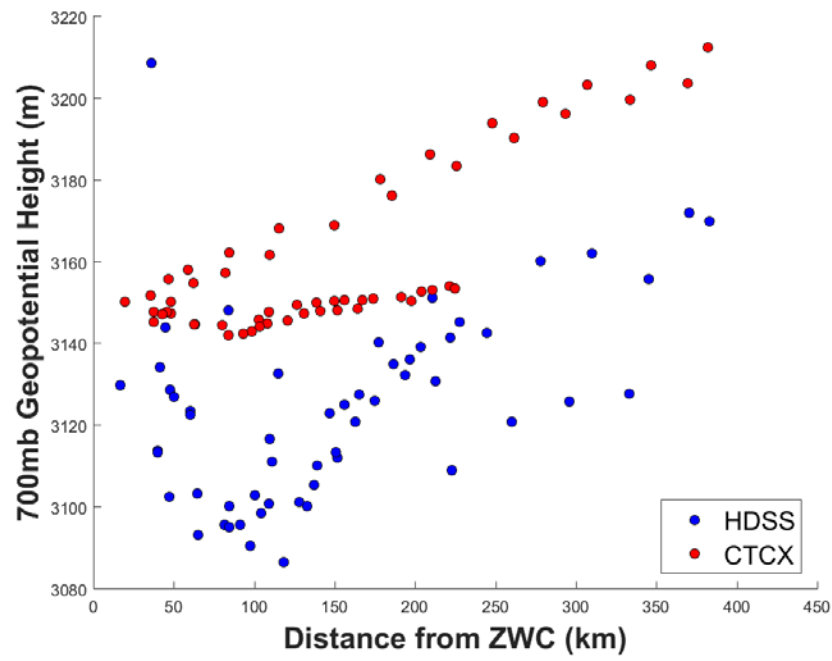


Figure 70. Geopotential heights as in Figure 64 except at 700 mb for 1800 UTC 21 October

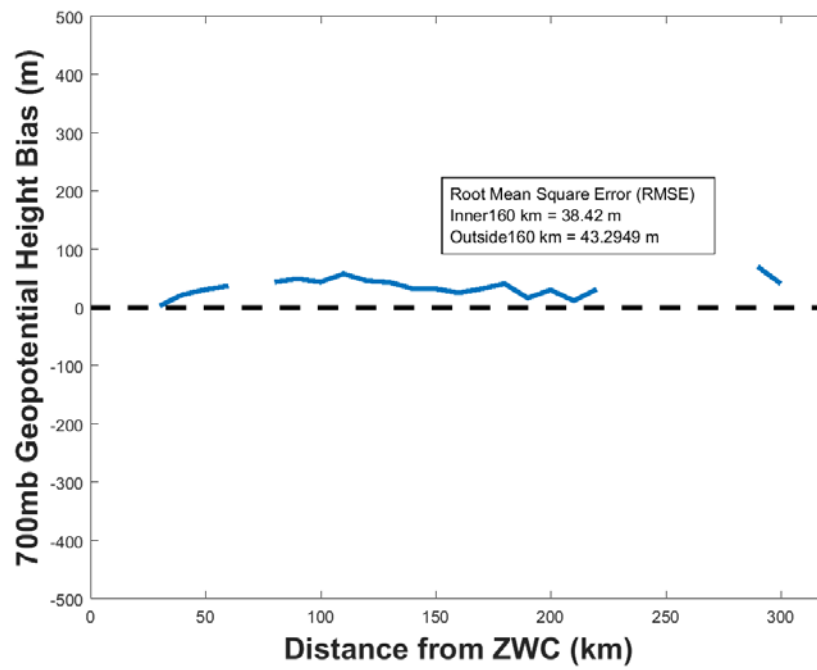


Figure 71. CTCX mean geopotential height bias as in Figure 65 except at 700 mb for 1800 UTC 21 October

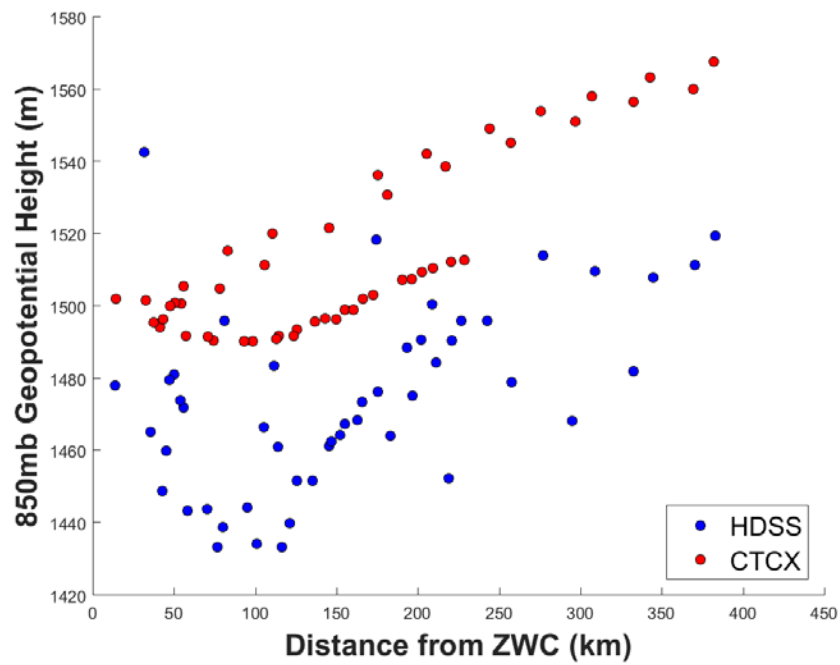


Figure 72. Geopotential heights as in Figure 64 except at 850 mb for 1800 UTC 21 October

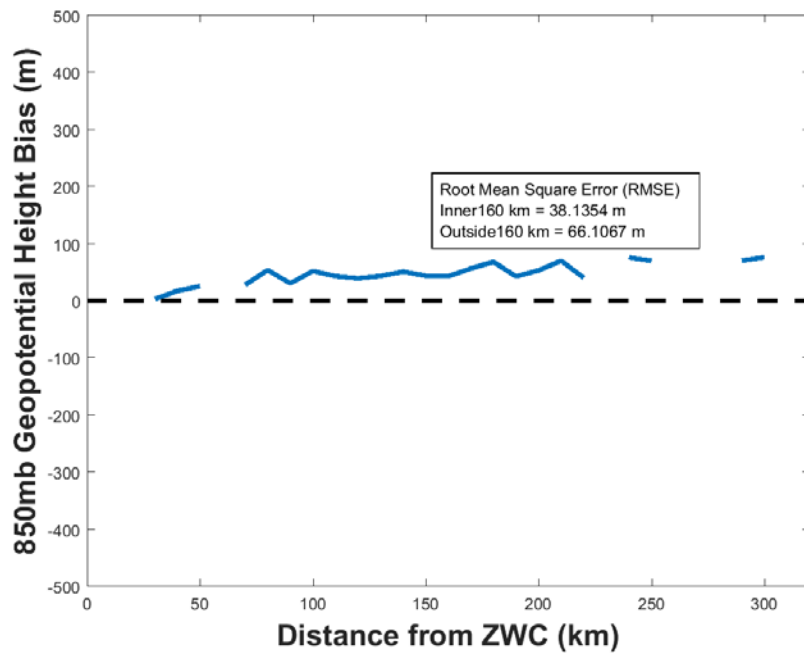


Figure 73. CTCX mean geopotential height bias as in Figure 65 except at 850 mb for 1800 UTC 21 October

The CTCX model initial geopotential heights (Figures 64 and 65) essentially are flat between 400 km radius and the center, which is consistent with the very light wind speeds at this level (Figure 30). No consistent geopotential height radial gradient in the HDSS observations is evident even though the HDSS-observed winds range from 0 to 19 m/s. This apparent departure from gradient wind balance is attributed to the 200 mb flow at this early stage of Patricia being highly disorganized in response to multiple deep convective systems (Figure 2). Thus, the CTCX 200 mb geopotential heights do not have any consistent bias relative to the HDSS observations (Figure 65).

The CTCX model geopotential heights at 300 mb (Figure 66) have a similar flat radial profile as at 200 mb plus a linear profile of decreasing heights toward the center that would indicate the Patricia circulation is embedded in a cyclonic upper-level trough. As at 200 mb, the HDSS geopotential heights are highly scattered, which again is attributed to the outflows from several deep convective systems. No systematic bias of the CTCX heights exists relative to the HDSS observations at this level (Figure 67).

The CTCX model 500 mb geopotential heights (Figure 68) have two flat radial profiles within 200 km radius and two linear gradient profiles extending to 400 km, which may be related to the linear increase in wind speed within 200 km radius and the nearly constant wind speeds between the inner core and 400 km in Figure 34. It is clear in Figures 68 and 69 that the CTCX heights are consistently too large compared to the HDSS observations.

The pattern of the CTCX model having two flat radial profiles within 200 km radius and two linear gradient profiles previously seen at 500 mb is also present for the 700 mb geopotential heights. However, the HDSS geopotential heights have a progressively steeper gradient as the inner-core region is approached, as is expected with an increasing wind speed in the inner core of a TC. In addition to the HDSS geopotential heights being generally lower, the steepening gradient in the inner core contributes to the CTCX heights having a positive bias relative to the HDSS heights (Figure 71).

At 850 mb (Figure 72), the two CTCX geopotential height radial profiles that were flat at 700 mb and above now have a steepening gradient as the inner core is

reached. However, the CTCX gradients are much smaller than the height gradients in the HDSS observations, which is consistent with the much larger wind speeds in the HDSS observations (Figure 38). As at 700 mb, the CTCX heights have a positive bias relative to the HDSS heights, especially within 200 km radius where the HDSS height gradients are steeper.

From the gradient wind balance in Figure 63, a lower geopotential height in the core indicates stronger winds in a TC (Knaff and Zehr, 2007; Hendricks and Peng, 2012). The observed heights in the core at low levels are less than were initialized in the CTCX model, a finding which is consistent with the model being initialized too weak at this valid time. The heights being initialized too small is likely a result of solving the nonlinear balance equation (generalization of the gradient wind equation to asymmetric flow) with too weak of a tangential wind field (as shown earlier in the storm-relative wind comparisons).

2. 22 October 2015

Similar geopotential height plots will be compared for 1800 UTC 22 October (Figures 74–83). Aircraft data is again included in the 700 mb plots. Based on results from the 22 October storm-relative wind speed comparisons, this study expects to find geopotential height anomalies that suggest the CTCX initial bogus vortex radius is too large.

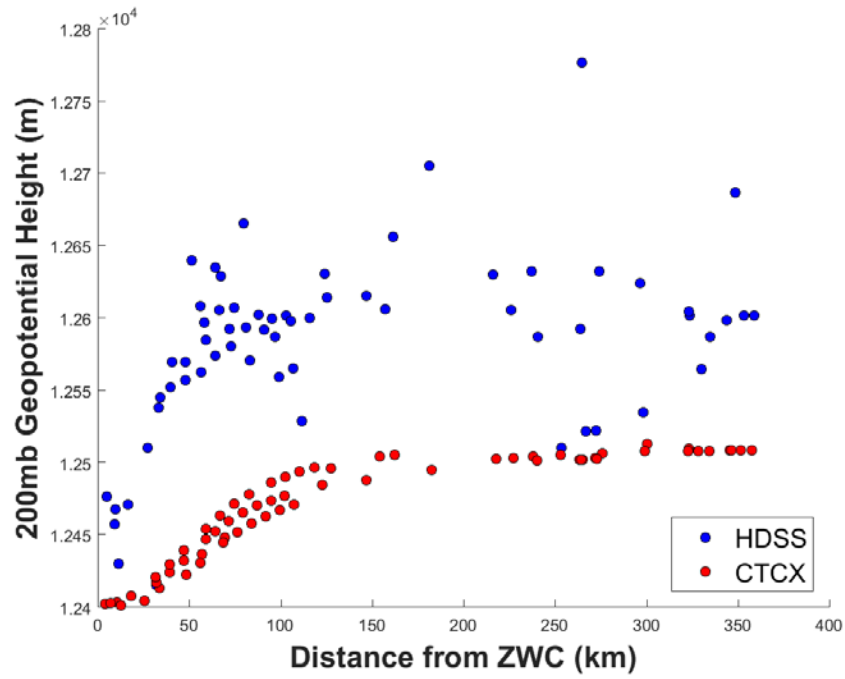


Figure 74. Geopotential heights as in Figure 64 except at 200 mb for 1800 UTC 22 October

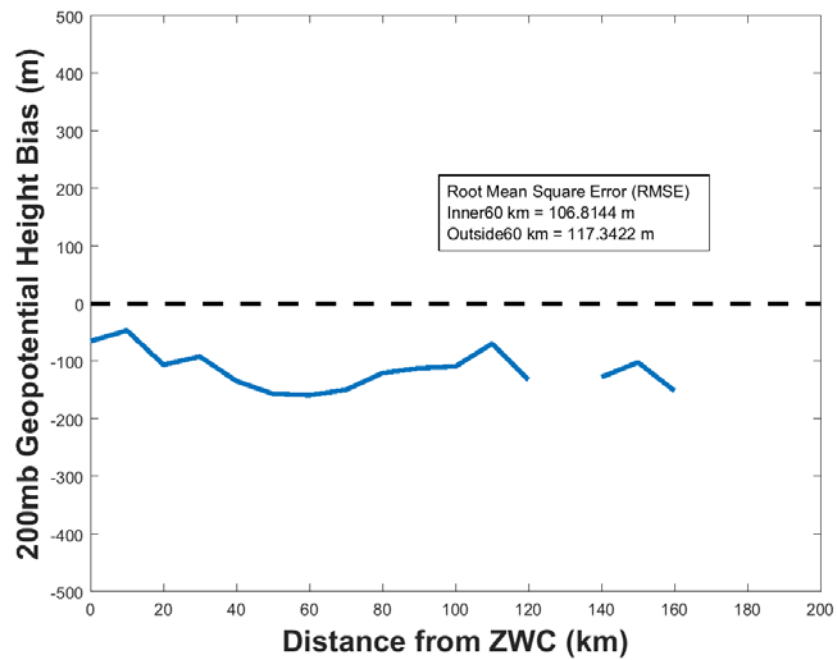


Figure 75. CTCX mean geopotential height bias as in Figure 65 except at 200 mb for 1800 UTC 22 October

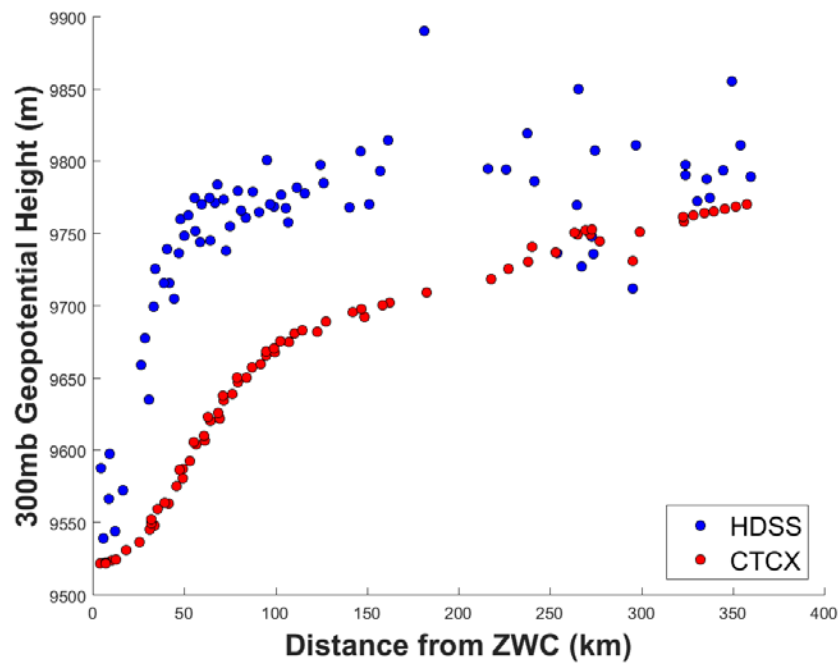


Figure 76. Geopotential heights as in Figure 64 except at 300 mb for 1800 UTC 22 October

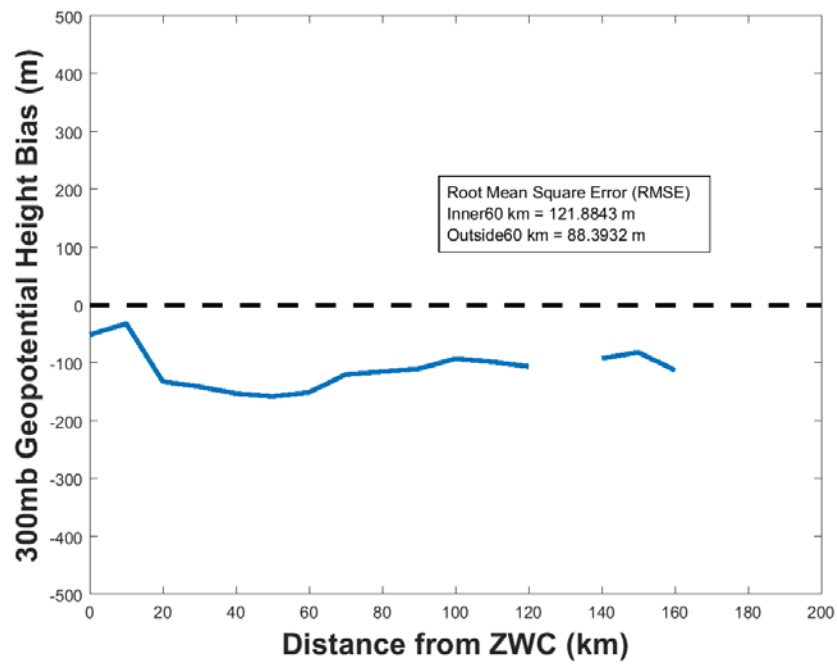


Figure 77. CTCX mean geopotential height bias as in Figure 65 except at 300 mb for 1800 UTC 22 October

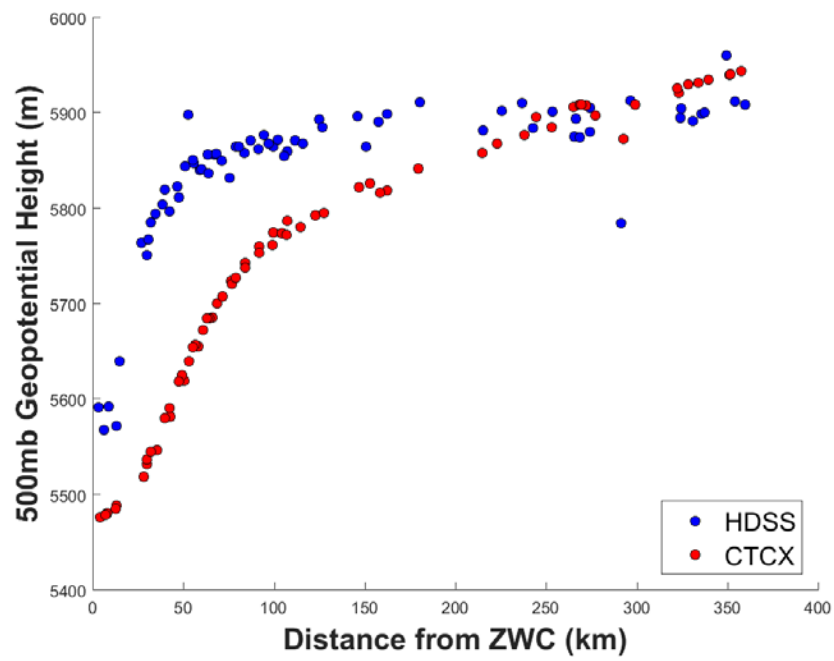


Figure 78. Geopotential heights as in Figure 64 except at 500 mb for 1800 UTC 22 October

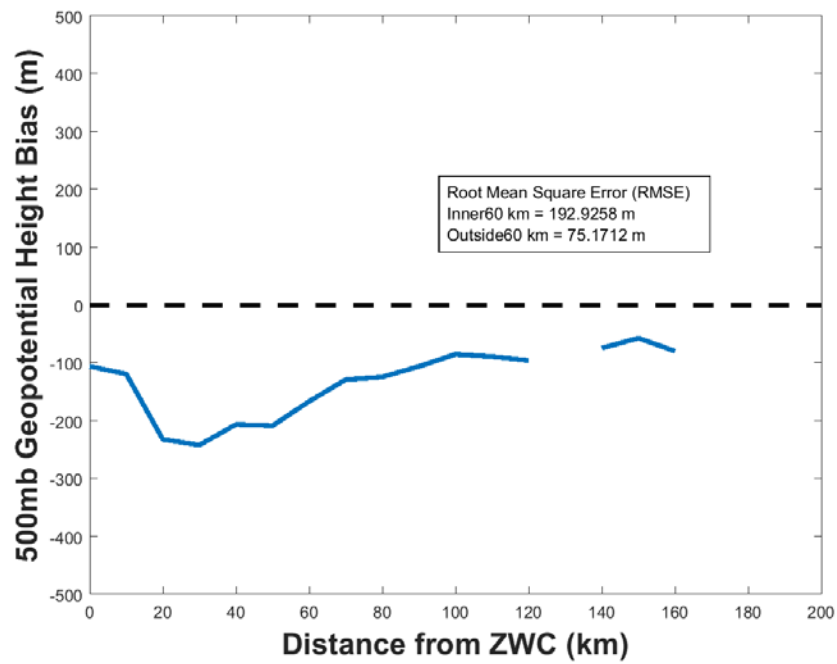


Figure 79. CTCX mean geopotential height bias as in Figure 65 except at 500 mb for 1800 UTC 22 October

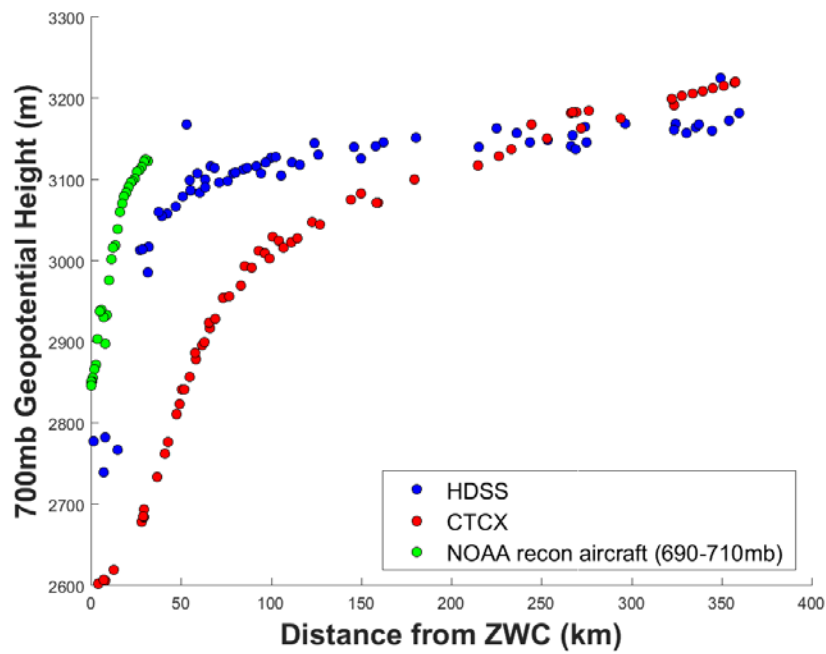


Figure 80. Geopotential heights as in Figure 64 except at 700 mb for 1800 UTC 22 October

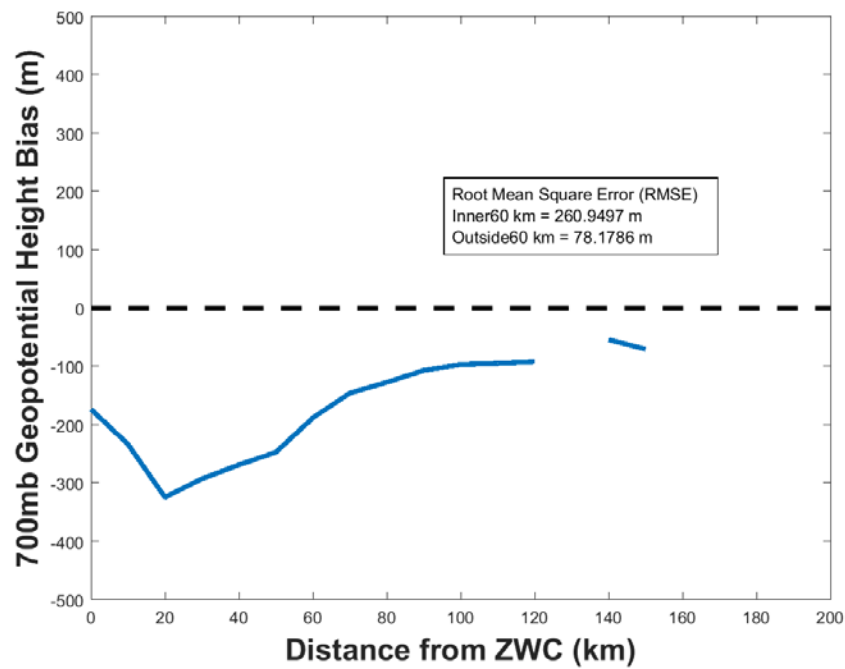


Figure 81. CTCX mean geopotential height bias as in Figure 65 except at 700 mb for 1800 UTC 22 October

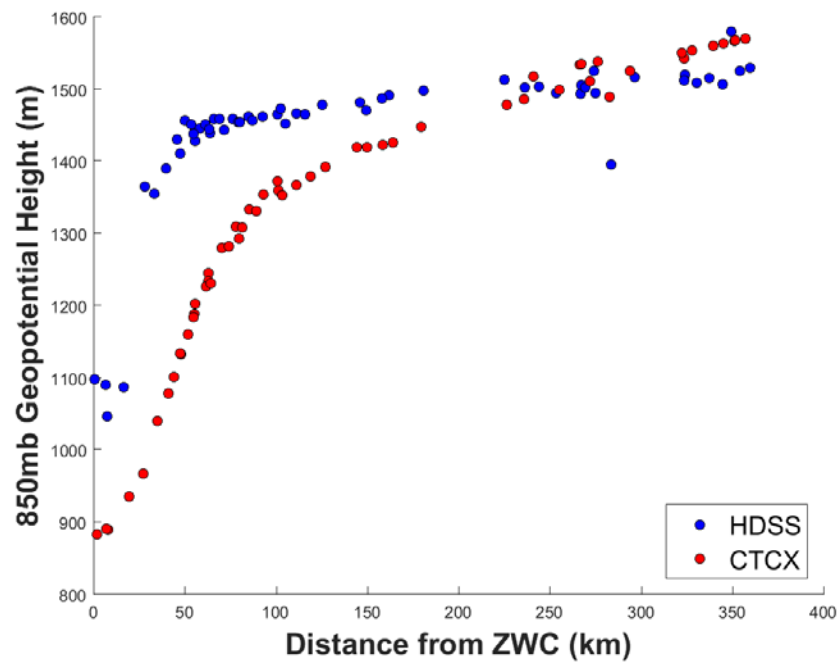


Figure 82. Geopotential heights as in Figure 64 except at 850 mb for 1800 UTC 22 October

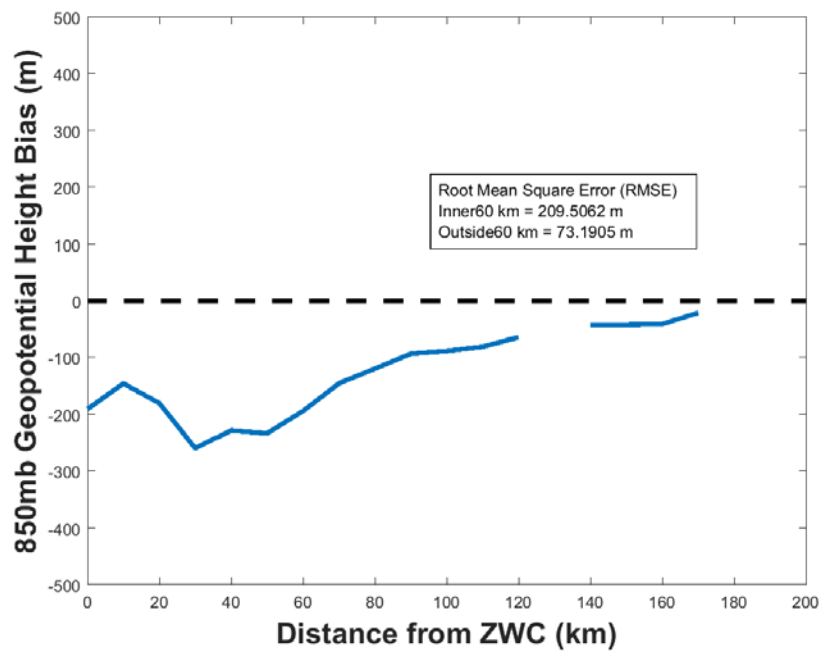


Figure 83. CTCX mean geopotential height bias as in Figure 65 except at 850 mb for 1800 UTC 22 October

Although the CTCX initial conditions have a negative bias in the inner-core region at all analyzed pressure levels when compared to the HDSS observations, there is a clear difference in the radial location of the steep gradients in geopotential heights as the center is approached. In the geopotential height radial plots, the eye-wall can be found in the area where height gradient is largest (Willoughby et al., 2006). At all analyzed pressure levels, the HDSS observations depict this gradient to be around 20 km radius, whereas the steep gradients in the CTCX initial conditions are around 50 km. This indicates the CTCX bogus vortex radius is larger than the observed radius of Patricia's eye, as expected. At 700 mb and 850 mb, again the geopotential heights in the CTCX initial fields are lower than in the observations, indicating a slightly lower minimum central pressure and therefore a stronger wind field. This is consistent with the storm-relative wind speed comparisons. Recall that on 22 October the magnitude of maximum winds for both CTCX and the observations were relatively consistent, but the CTCX winds covered a larger area because they did not diminish at the same rate as the observed winds outside the core. The larger radial extent of stronger winds in CTCX causes larger Coriolis and centrifugal terms in the gradient wind equation, and therefore a significantly lower geopotential height field in the inner-core when integrating the gradient wind equation inward. By contrast, the HDSS observations have weaker outer-circulation winds, which produce very small variations in the geopotential height field in the outer region. However, HDSS indicates very strong winds in the inner-core, causing the geopotential heights to decrease rapidly there. Overall, the variation in geopotential height can be explained well by the variation in tangential winds through the gradient wind balance equation (Figure 63).

3. 23 October 2015

Finally, the geopotential heights will be compared for 1800 UTC 23 October (Figures 84–93). Aircraft data is included in the 700 mb plot. The wind speed analysis suggests that the CTCX initial geopotential heights will be more consistent with the in-situ observations than for 22 October, although the bogus vortex may still have a radius that is slightly too large.

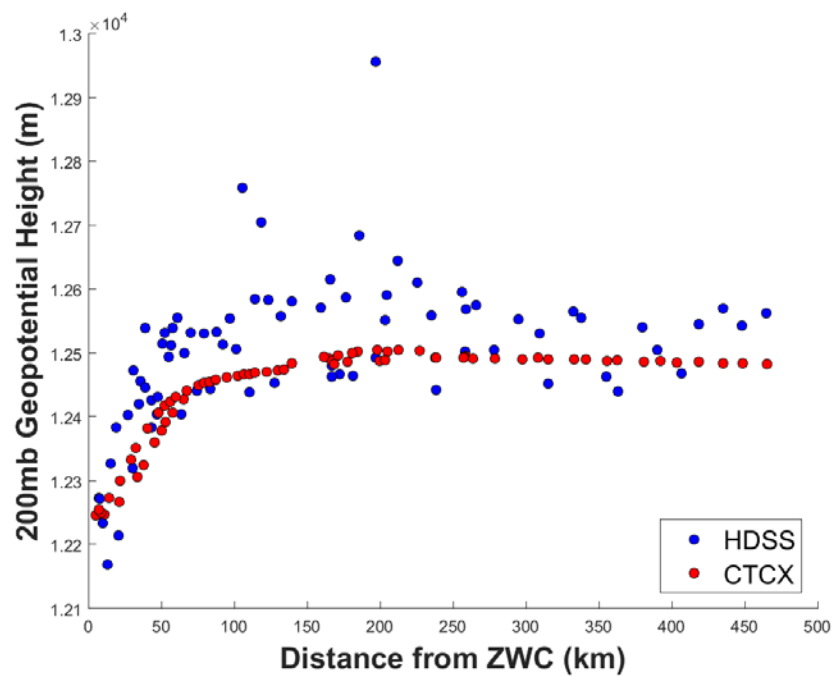


Figure 84. Geopotential heights as in Figure 64 except at 200 mb for 1800 UTC 23 October

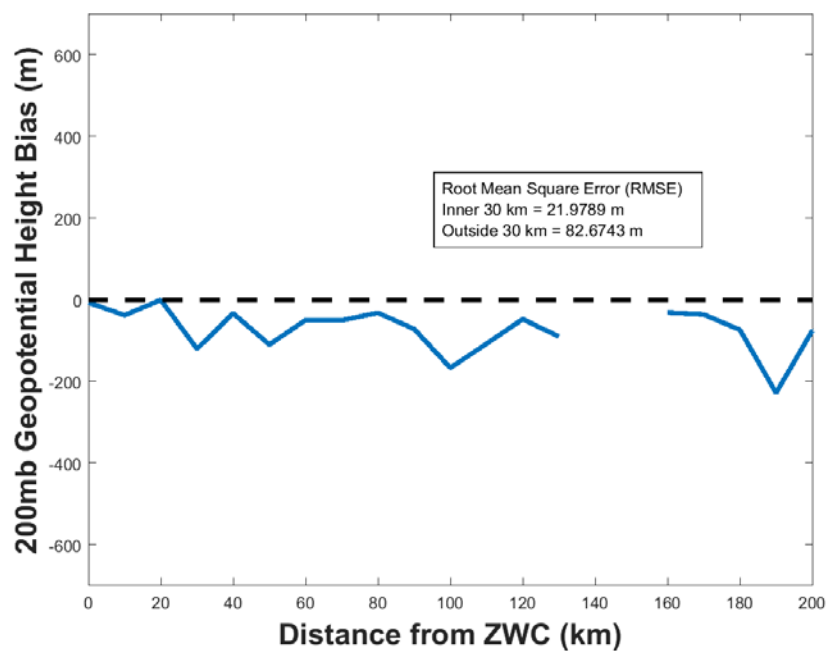


Figure 85. CTCX mean geopotential height bias as in Figure 65 except at 200 mb for 1800 UTC 23 October

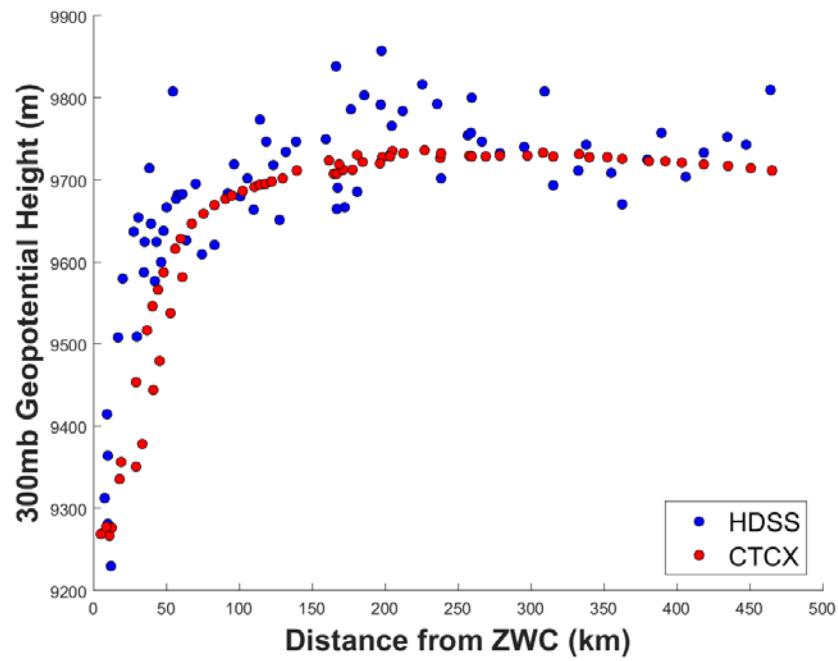


Figure 86. Geopotential heights as in Figure 64 except at 300 mb for 1800 UTC 23 October

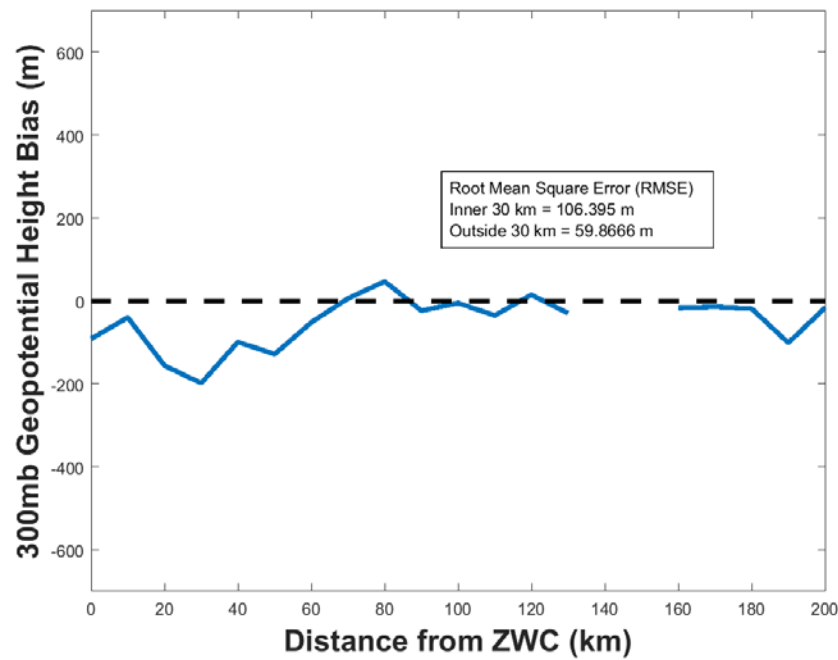


Figure 87. CTCX mean geopotential height bias as in Figure 65 except at 300 mb for 1800 UTC 23 October

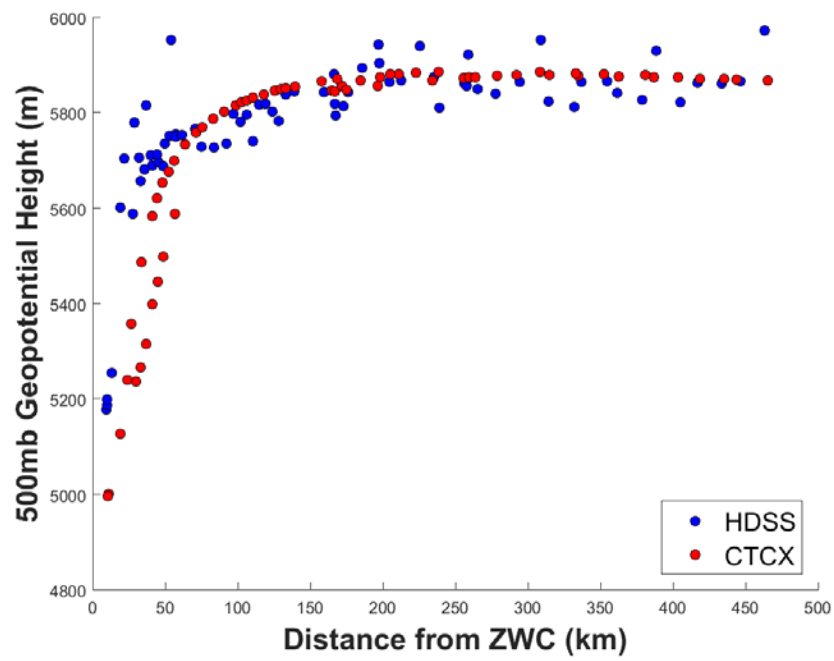


Figure 88. Geopotential heights as in Figure 64 except at 500 mb for 1800 UTC 23 October

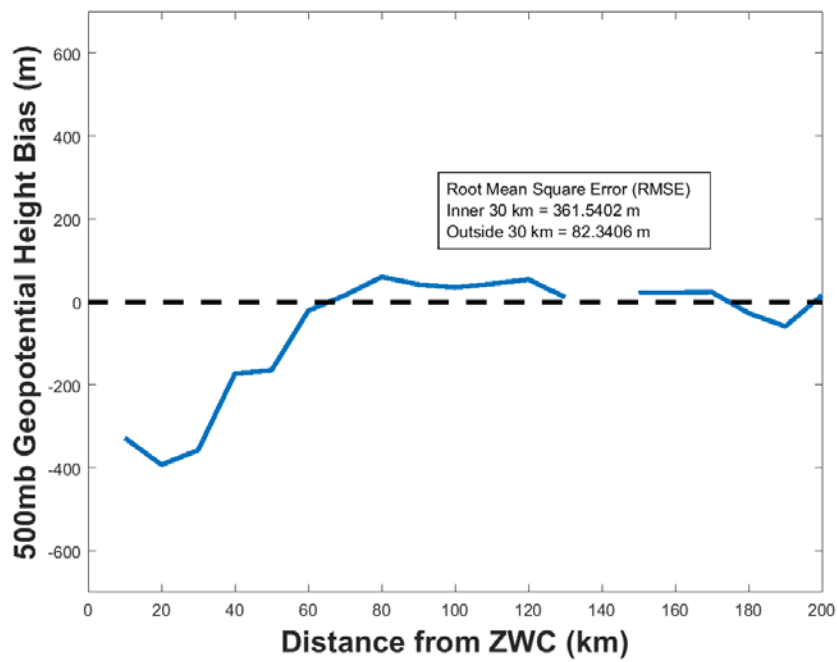


Figure 89. CTCX mean geopotential height bias as in Figure 65 except at 500 mb for 1800 UTC 23 October

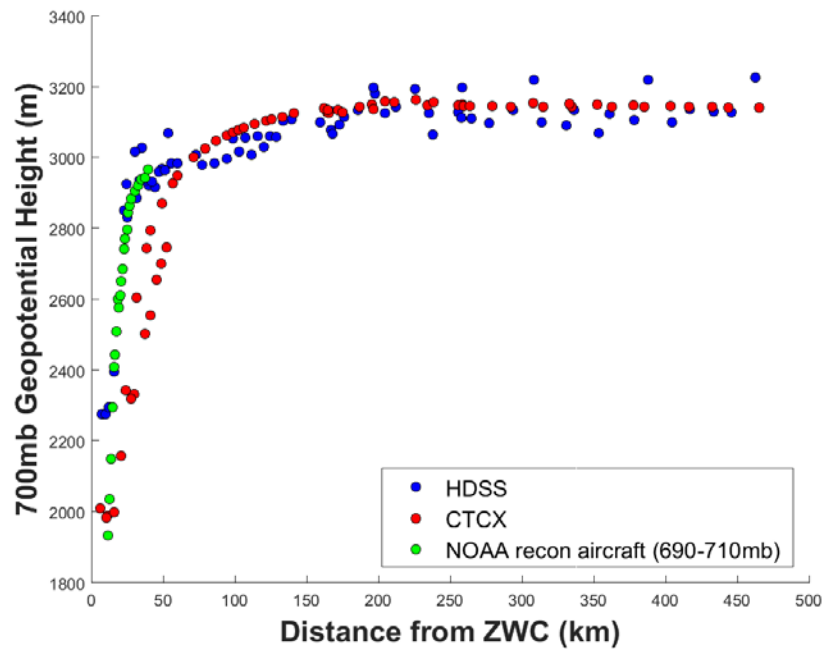


Figure 90. Geopotential heights as in Figure 64 except at 700 mb for 1800 UTC 23 October

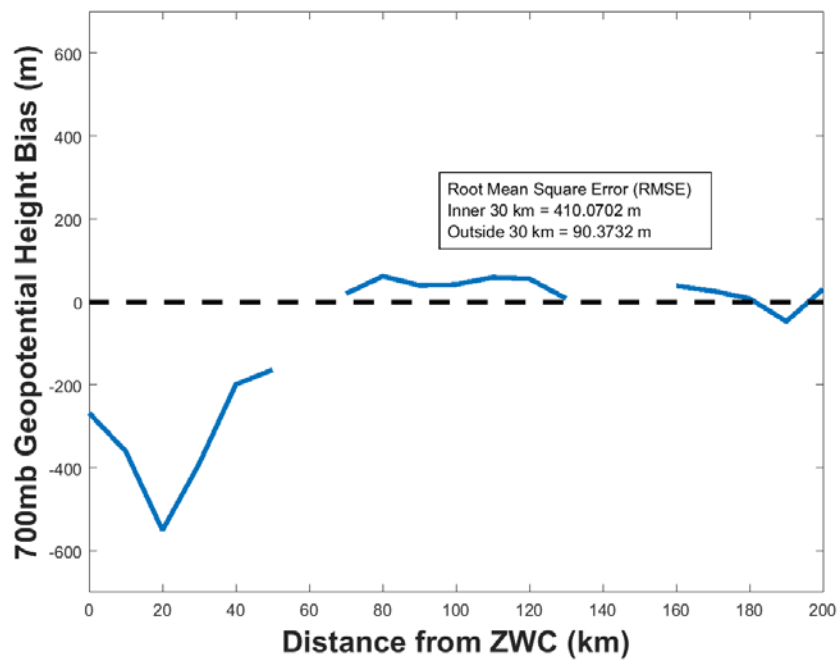


Figure 91. CTCX mean geopotential height bias as in Figure 65 except at 700 mb for 1800 UTC 23 October

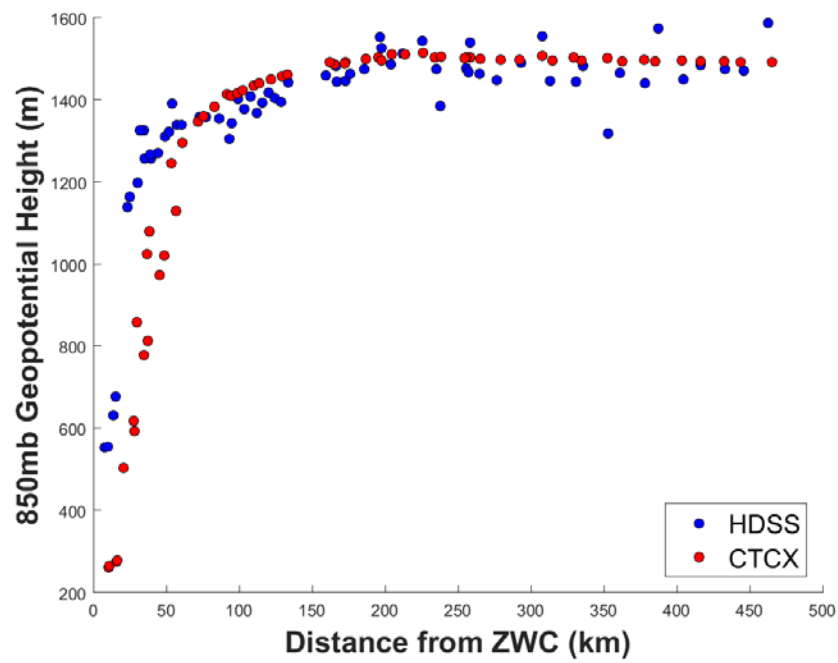


Figure 92. Geopotential heights as in Figure 64 except at 850 mb for 1800 UTC 23 October

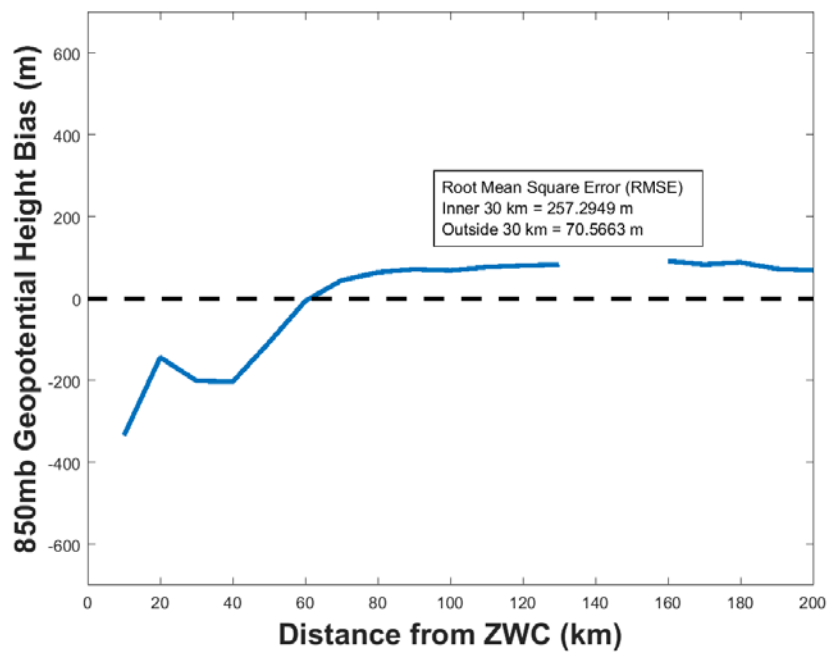


Figure 93. CTCX mean geopotential height bias as in Figure 65 except at 850 mb for 1800 UTC 23 October

The CTCX initialized at 1800 UTC 23 October shows very little bias from the HDSS observations in the middle and upper levels from 500 mb up to 200 mb. However, at the 700 mb and 850 mb pressure levels, a comparison of the strongest geopotential height gradient indicates that the CTCX vortex radius is approximately 15 km larger than the observed eye-wall radius. As in the 22 October comparisons, the CTCX geopotential heights also exhibit a negative bias in the core at the lower levels, although the discrepancy is not as large.

D. POTENTIAL TEMPERATURE AND WARM CORE STRUCTURE

Chen and Zhang (2012) found that even small changes in the radial profile of potential temperature and the height of the TC warm core may have large impacts on the rate of rapid intensification. Recall that the hydrostatic equation in Figure 63 relates the temperature to the vertical gradient of the geopotential heights in the previous section. Since the TC is a warm-core circulation, a higher temperature in the eye means larger geopotential heights between the pressure surfaces. As in the storm-relative wind speed comparisons, the HDSS, aircraft, and CTCX potential temperature datasets have been adjusted to the same valid time and storm-relative coordinates. Potential temperature has been calculated for all datasets using the standard Poisson equation (Figure 94).

$$\theta(z) = T(z)(p_s/p)^{R/c_p}$$

$T(z)$ is the observed air temperature in K at height z , and p_s is the air pressure at height z . p is the reference pressure (1000 mb for this study), and the Poisson constant R/c_p is 0.286.

Figure 94. Standard Poisson equation for potential temperature $\theta(z)$ in K.

Source: University of Washington (www.atmos.washington.edu).

1. 21 October 2015

Similar to the previous sections, CTCX model potential temperatures will be compared with the HDSS observations as a function of distance from the TC center.

These evaluations will be at the 200 mb, 300 mb, 500 mb, 700 mb, and 850 mb pressure surfaces for 1800 UTC 21 October 2015 (Figures 95–104).

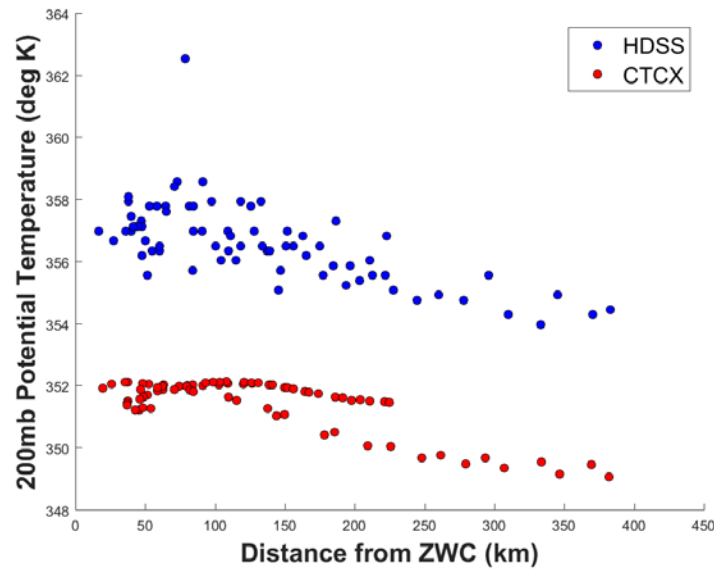


Figure 95. Potential temperatures (K) from HDSS (blue dots) and CTCX initial conditions (red dots) as a function of distance from the zero-wind center (ZWC) at 200 mb for 1800 UTC 21 October

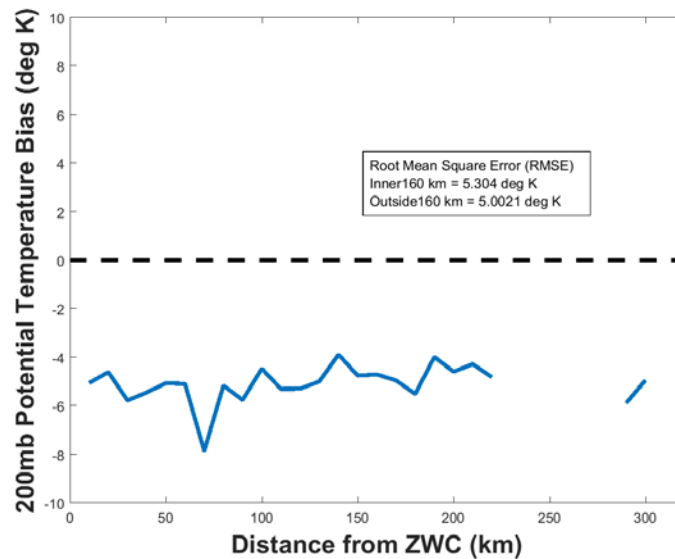


Figure 96. CTCX mean potential temperature bias relative to HDSS observations averaged in 10 km radial bands at 200 mb for 1800 UTC 21 October

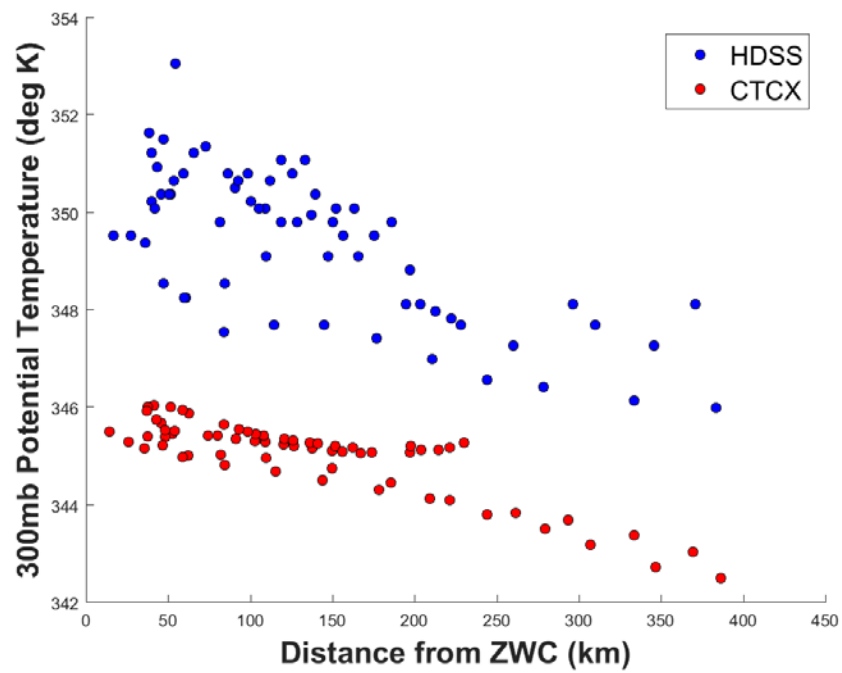


Figure 97. Potential temperatures as in Figure 95 except at 300 mb for 1800 UTC 21 October

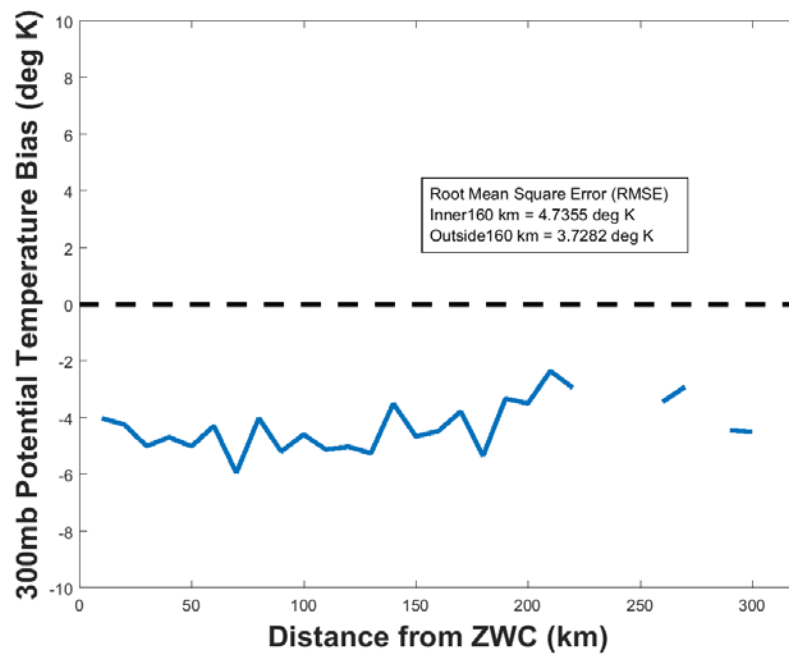
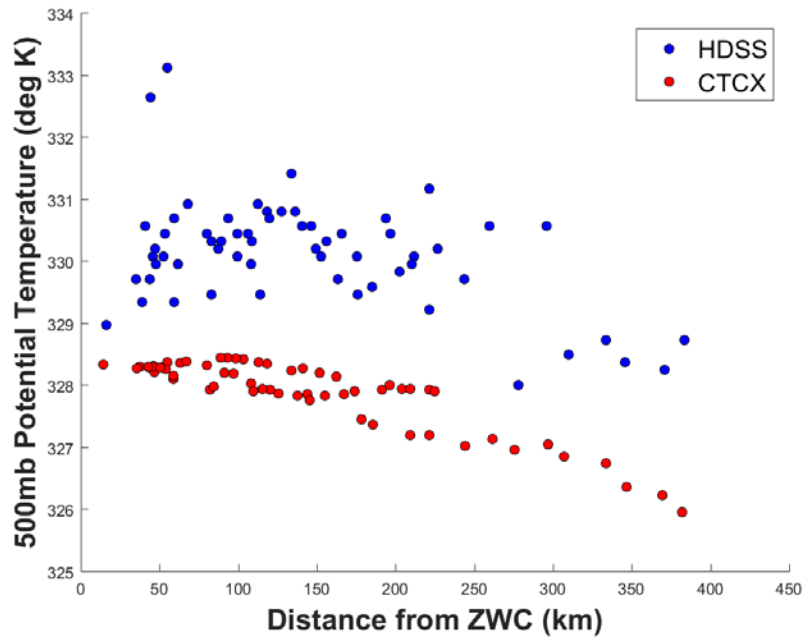


Figure 98. CTCX mean potential temperature bias as in Figure 96 except at 300 mb for 1800 UTC 21 October



Note the smaller temperature increments on the Y-axis relative to the 200 mb and 300 mb plots.

Figure 99. Potential temperatures as in Figure 95 except at 500 mb for 1800 UTC 21 October

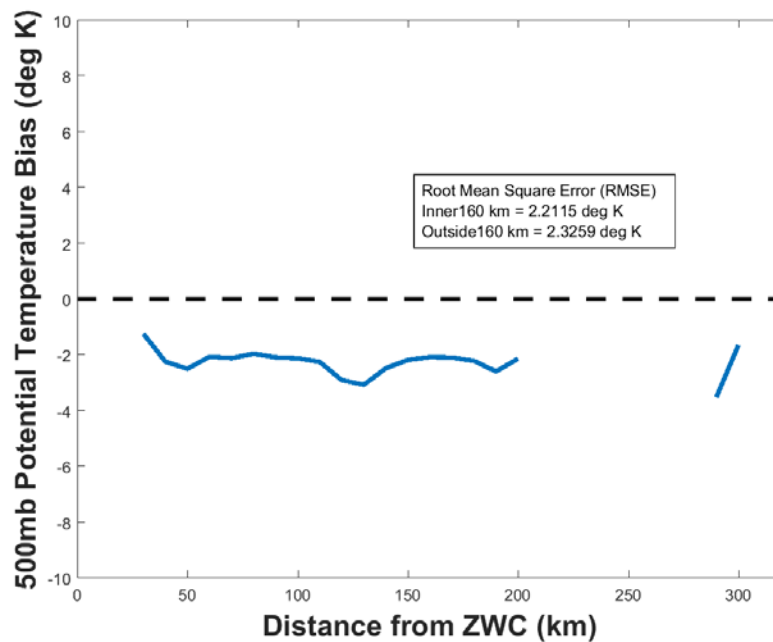
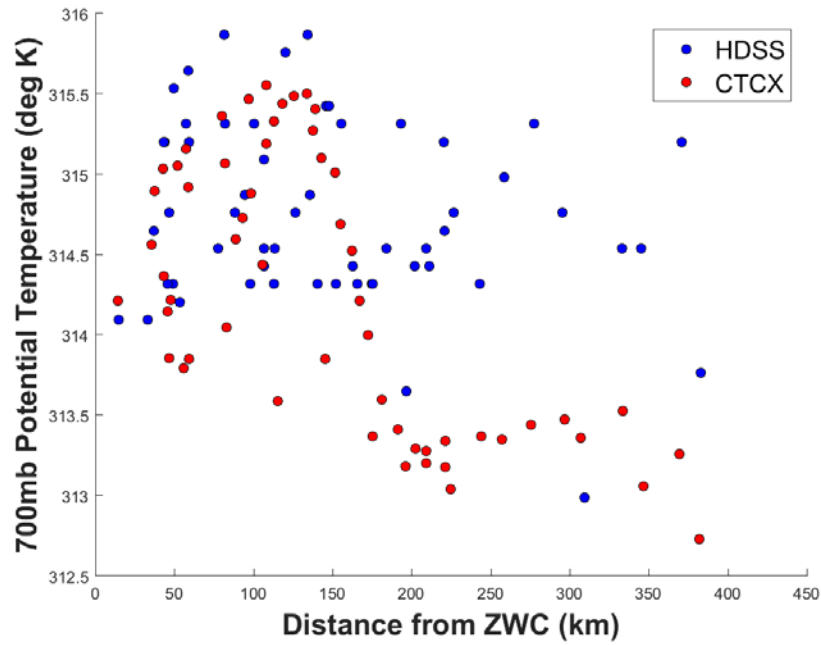


Figure 100. CTCX mean potential temperature bias as in Figure 96 except at 500 mb for 1800 UTC 21 October



Note the smaller Y-axis temperature increments relative to the 500 mb plot.

Figure 101. Potential temperatures as in Figure 95 except at 700 mb for 1800 UTC 21 October

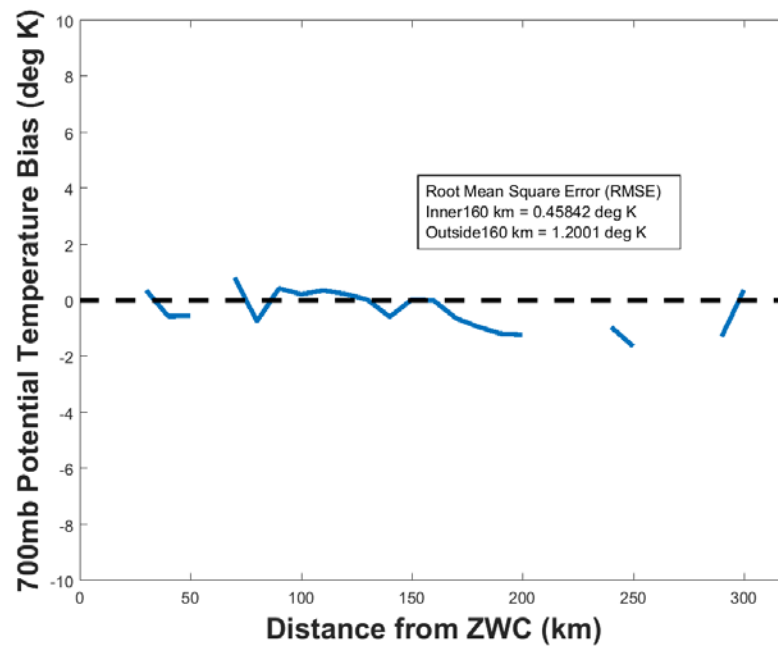


Figure 102. CTCX mean potential temperature bias as in Figure 96 except at 700 mb for 1800 UTC 21 October

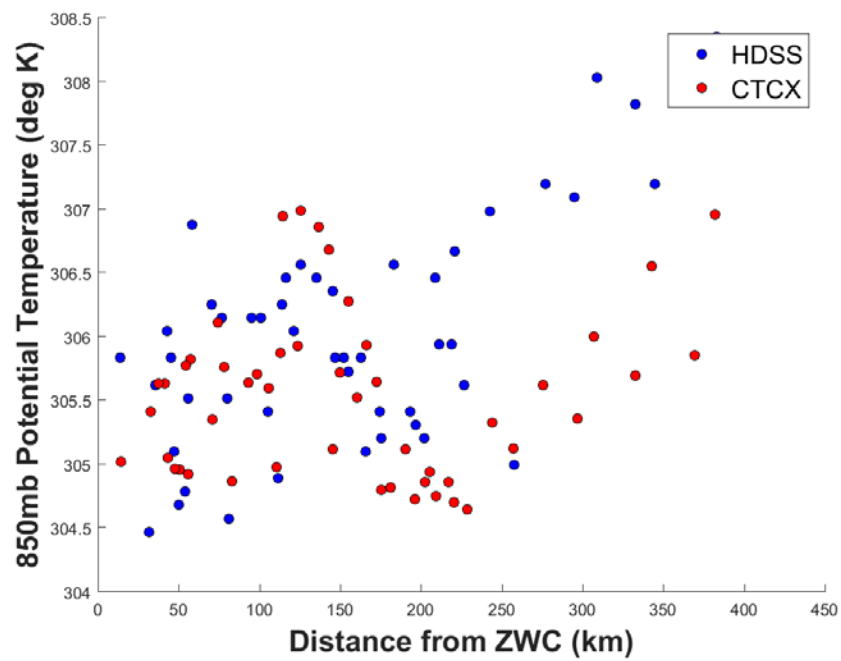


Figure 103. Potential temperatures as in Figure 95 except at 850 mb for 1800 UTC 21 October

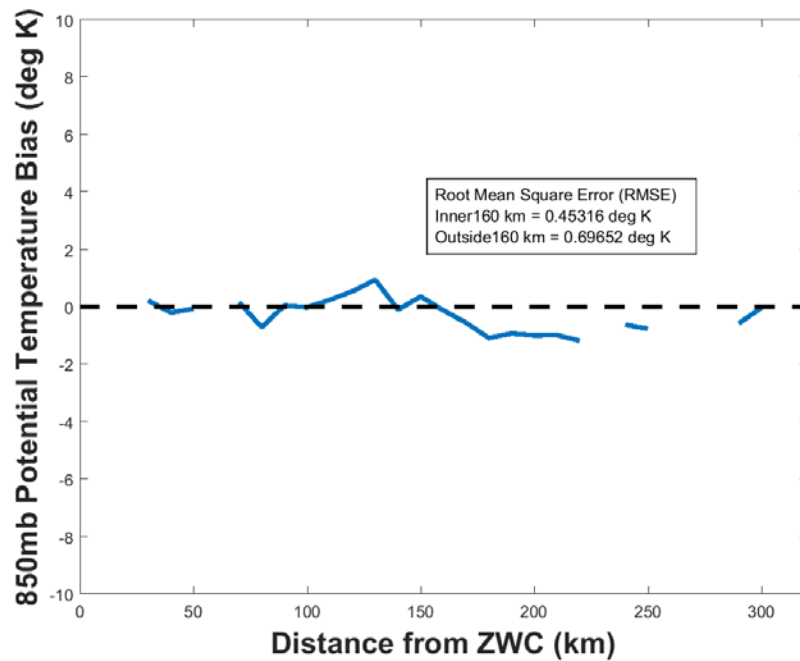


Figure 104. CTCX mean potential temperature bias as in Figure 96 except at 850 mb for 1800 UTC 21 October

The HDSS observations indicate that by 1800 UTC 21 October, Tropical Storm Patricia was already beginning to develop an upper-level warm core, a feature that is not represented in the CTCX model initialized at the same time.

The CTCX potential temperatures at 200 mb (Figures 95 and 96) are consistently about 5 K lower than the HDSS observations throughout the radial extent of the this analysis, and the smaller radial temperature gradient for the CTCX means it has a weaker warm core than is observed by the HDSS dropsondes. Assuming the tropopause is relatively flat at this TS stage, the flat CTCX temperature profile within 200 km radius is consistent with the flat 200 mb geopotential profile in Figure 64.

At 300 mb (Figure 97), the CTCX potential temperature field has a flat radial profile within 200 km radius and a separate linear gradient profile from 400 km radius to the central region. By contrast, the HDSS observations have a larger radial gradient and approximately 6 K warmer core, which is consistent with the lower 300 mb HDSS-observed geopotential heights in the inner region (Figure 66). The large cold bias of the CTCX model relative to the HDSS observations is shown in figure 98.

Although the radial profiles at 500 mb (Figure 99) have smaller gradients than at 300 mb, the HDSS observations continue to indicate a warmer inner core than the CTCX would. Therefore, the 500 mb geopotential heights are lower than in the CTCX model (Figure 68). A smaller 500 mb potential temperature bias of the CTCX relative to the HDSS observations is indicated in Figure 100.

At 700 mb and 850 mb (Figures 101 and 103), the CTCX model potential temperatures have rather similar values to the HDSS observations within 150 km radius, and only slightly lower temperatures beyond 200 km radius. Consequently, the CTCX model has a near-zero bias relative to the HDSS observations in the lower levels of the troposphere (Figures 102 and 104).

Recall from the comparison of storm-relative wind speeds on 21 October that the CTCX model was initialized too weak. These potential temperature comparisons support that same conclusion.

2. 22 October 2015

The same comparisons will now be made for 1800 UTC 22 October 2015 (Figures 105–115). The aircraft reconnaissance mission data used in the earlier storm-relative wind speed comparison for 22 October will be used again in the 700 mb plots for potential temperature.

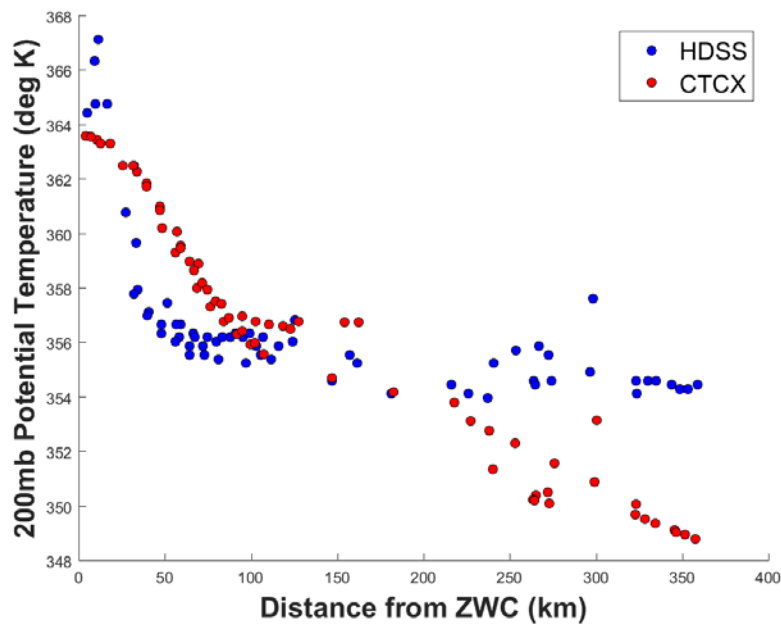


Figure 105. Potential temperatures as in Figure 95 except at 200 mb for 1800 UTC 22 October

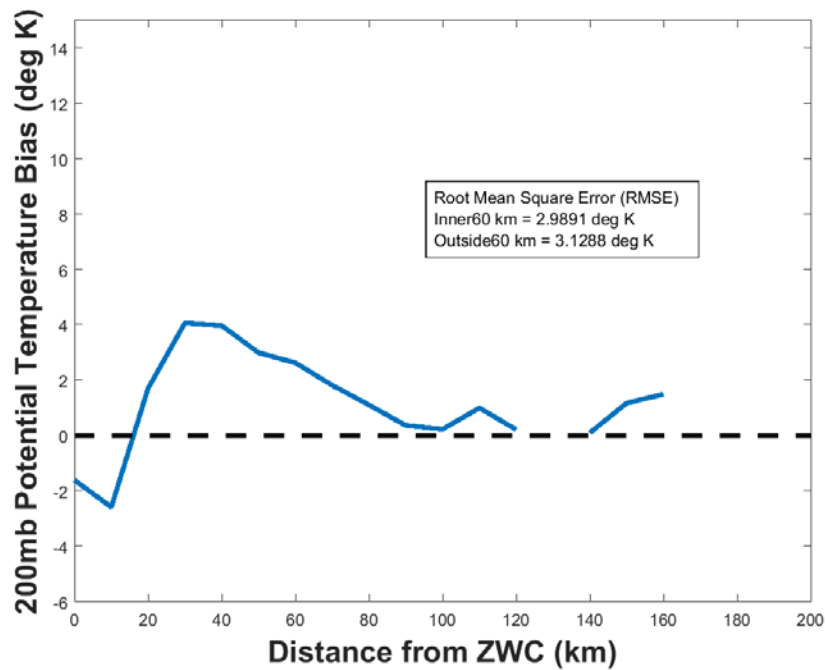


Figure 106. CTCX mean potential temperature bias as in Figure 96 except at 200 mb for 1800 UTC 22 October

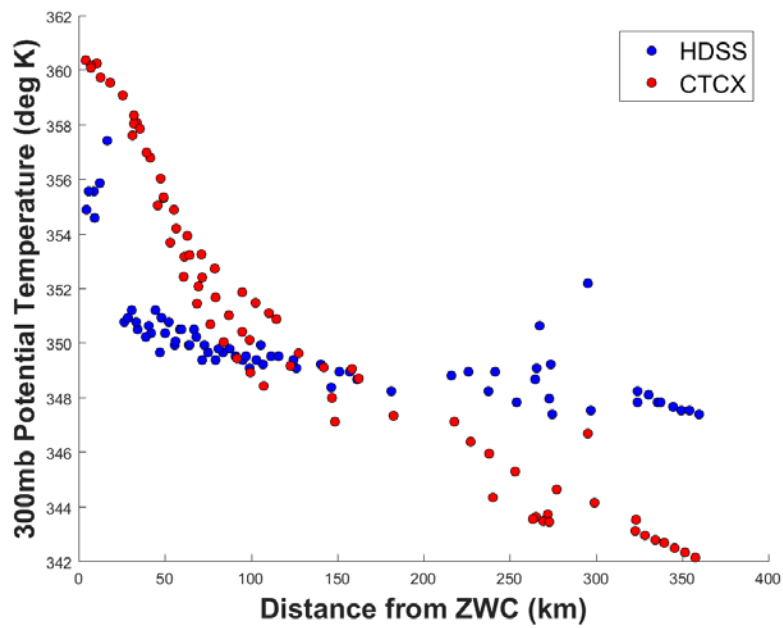


Figure 107. Potential temperatures as in Figure 95 except at 300 mb for 1800 UTC 22 October

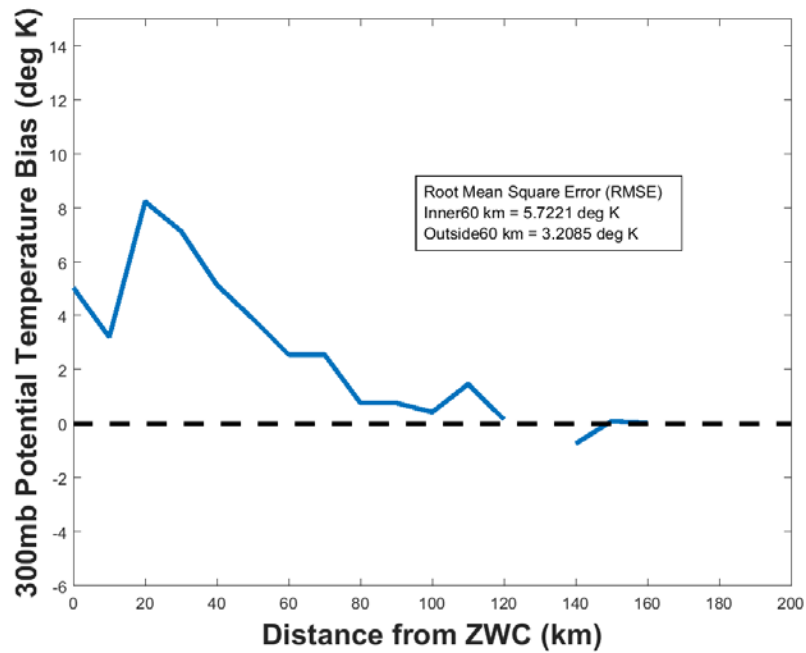


Figure 108. CTCX mean potential temperature bias as in Figure 96 except at 300 mb for 1800 UTC 22 October

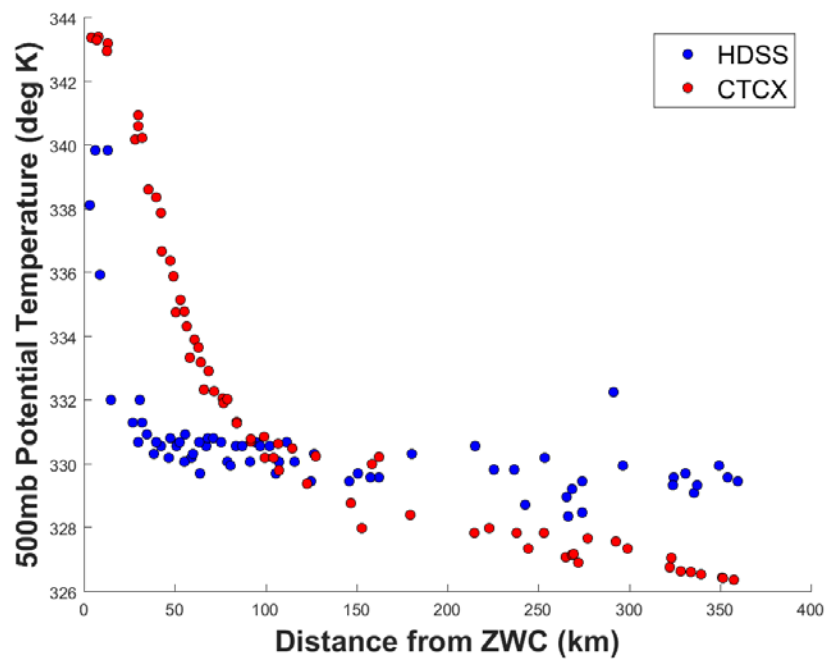


Figure 109. Potential temperatures as in Figure 95 except at 500 mb for 1800 UTC 22 October

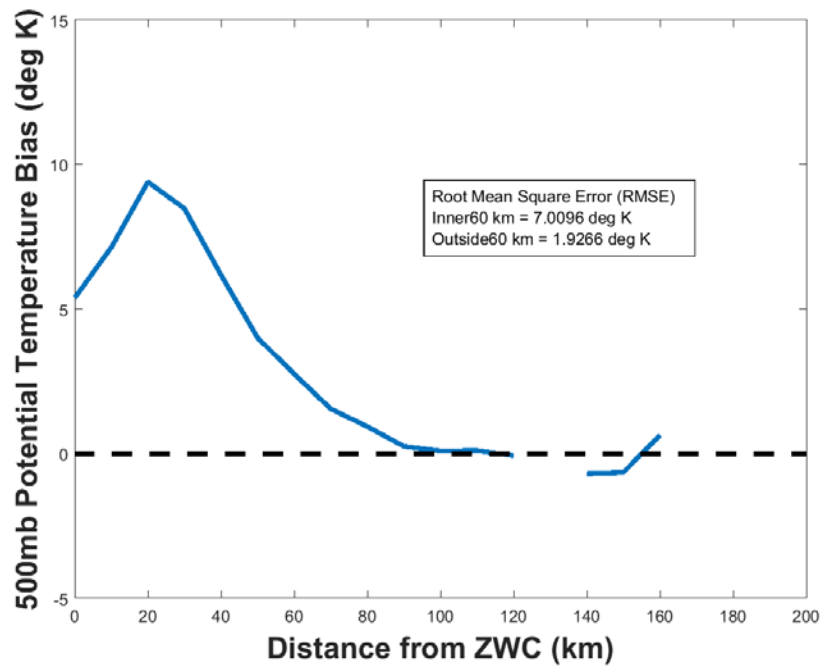


Figure 110. CTCX mean potential temperature bias as in Figure 96 except at 500 mb for 1800 UTC 22 October

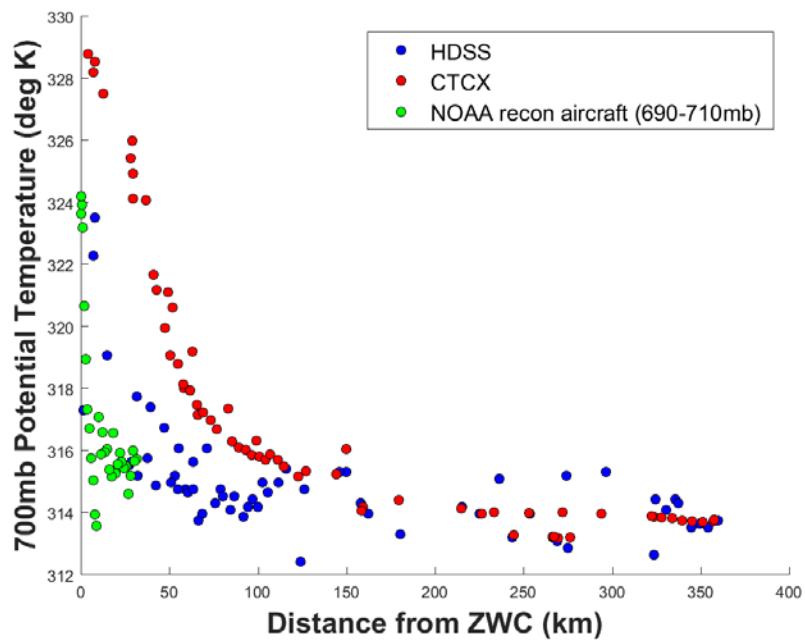


Figure 111. Potential temperatures as in Figure 95 except at 700 mb for 1800 UTC 22 October

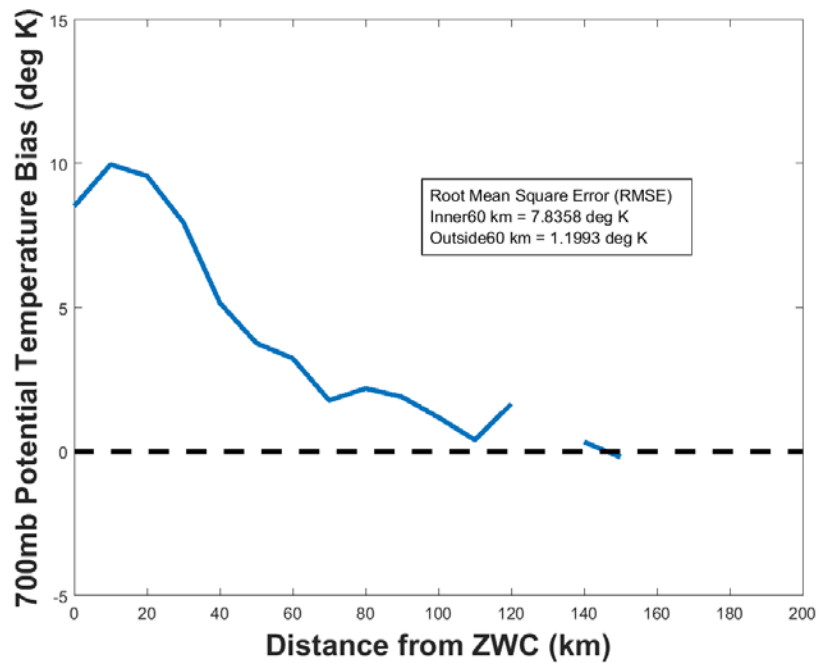


Figure 112. CTCX mean potential temperature bias as in Figure 96 except at 700 mb for 1800 UTC 22 October

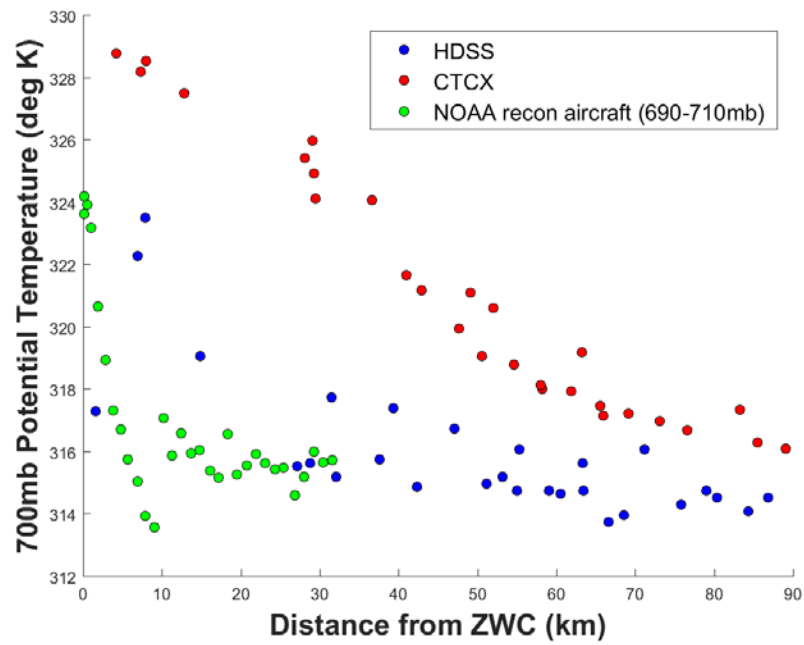
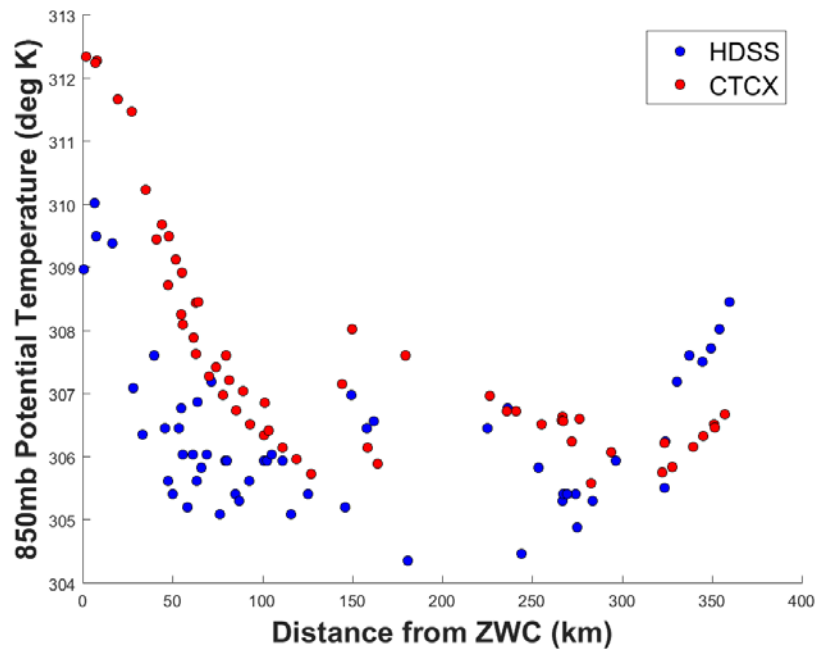


Figure 113. Potential temperatures in Figure 95 except at 700 mb for 1800 UTC 22 October (zoomed to display only the inner 90 km)



Note the smaller Y-axis temperature increments relative to plots at the other pressure levels.

Figure 114. Potential temperatures as in Figure 95 except at 850 mb for 1800 UTC 22 October

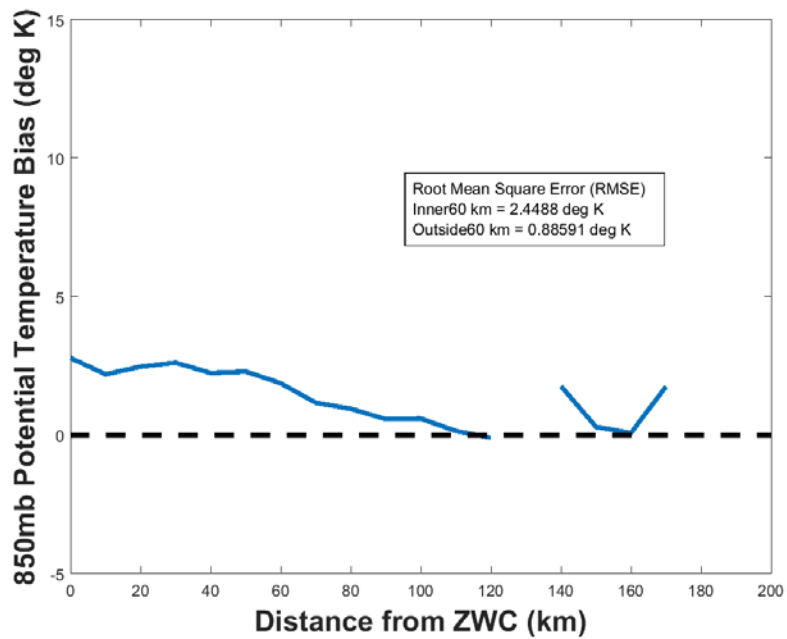


Figure 115. CTCX mean potential temperature bias as in Figure 96 except at 850 mb for 1800 UTC 22 October

At 200 mb, the CTCX initial potential temperature has a negative bias in Patricia's inner-core region and a positive bias outside the core. At all other pressure levels, the CTCX potential temperatures in the core are higher than the observed potential temperatures. After subtracting the Jordan annual mean tropical potential temperature sounding (Jordan, 1958), the observations indicate that the warmest potential temperature anomaly in the core is around 13 K near 300 mb, whereas the CTCX model initialized the warmest anomaly of 16 K near 500 mb. At this valid time, in-situ observations portray a more compact eye with a warm core near 300 mb, and the CTCX model initialized with a broader eye and a warm core located at 500 mb.

The potential temperature analysis is broadly consistent with the thermal wind balance equation (Figure 63), which states that the radial temperature gradient is proportional to two terms which are multiplied together. The first term involves the vertical derivative of the tangential wind velocity and the second term is directly proportional to the tangential velocity (and inversely proportional to the radius). Since the instantaneous vertical derivative of the tangential velocity at a pressure level is not known due to the coarse vertical resolution used in this study (only five pressure levels), the role of this term is not yet known. However, the second term is directly proportional to the tangential wind velocity and inversely proportional to the radius. Since the wind speed radial plots (as a proxy for the tangential velocity, particularly in the lower troposphere above the boundary layer where wind are mostly tangential) indicate stronger wind speeds in the CTCX initial conditions versus the HDSS observations outside the inner-core, the temperature should increase quicker when moving radially inward along a pressure surface solely due to this second term. Without precise knowledge of differences in the vertical derivative of the tangential velocity between CTCX and HDSS, it cannot be stated for certain that the potential temperature field is consistent with thermal wind balance. However, assuming minor differences exist in this instantaneous vertical derivative on a given pressure level between CTCX and HDSS, it is plausible that the differences in the radial structure of the warm core between CTCX and HDSS is mainly due to the differences in the radial structure of the winds (Stern and Nolan, 2012).

3. 23 October 2015

CTCX initial potential temperatures will not be compared to HDSS observations at 1800 UTC 23 October 2015 (Figures 116–126). As before, aircraft reconnaissance mission data will be used to supplement the HDSS data at 700 mb.

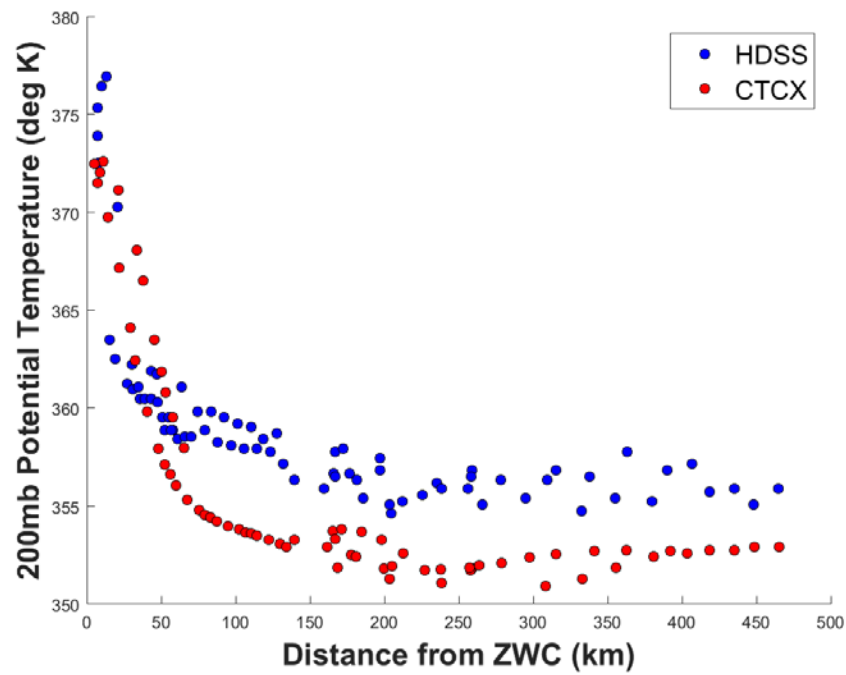


Figure 116. Potential temperatures as in Figure 95 except at 200 mb for 1800 UTC 23 October

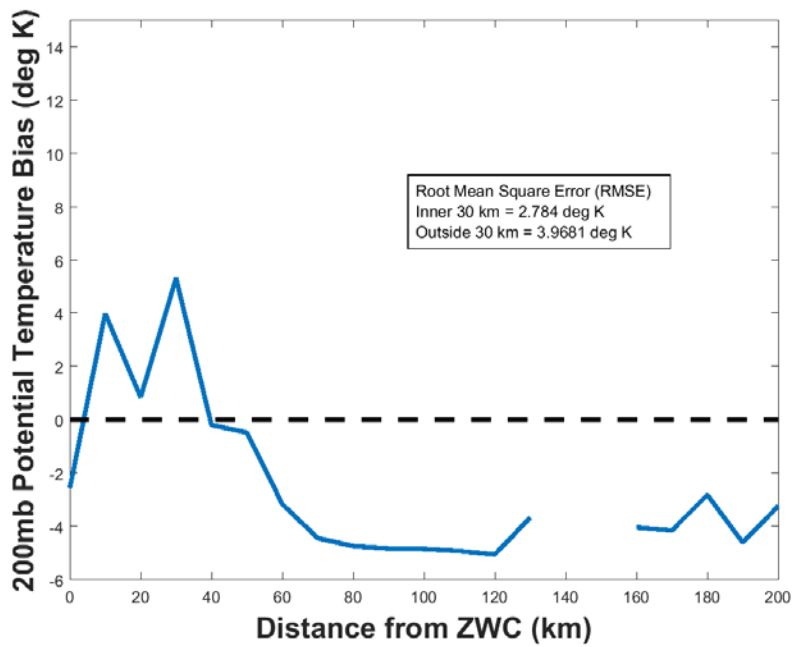


Figure 117. CTCX mean potential temperature bias as in Figure 96 except at 200 mb for 1800 UTC 23 October

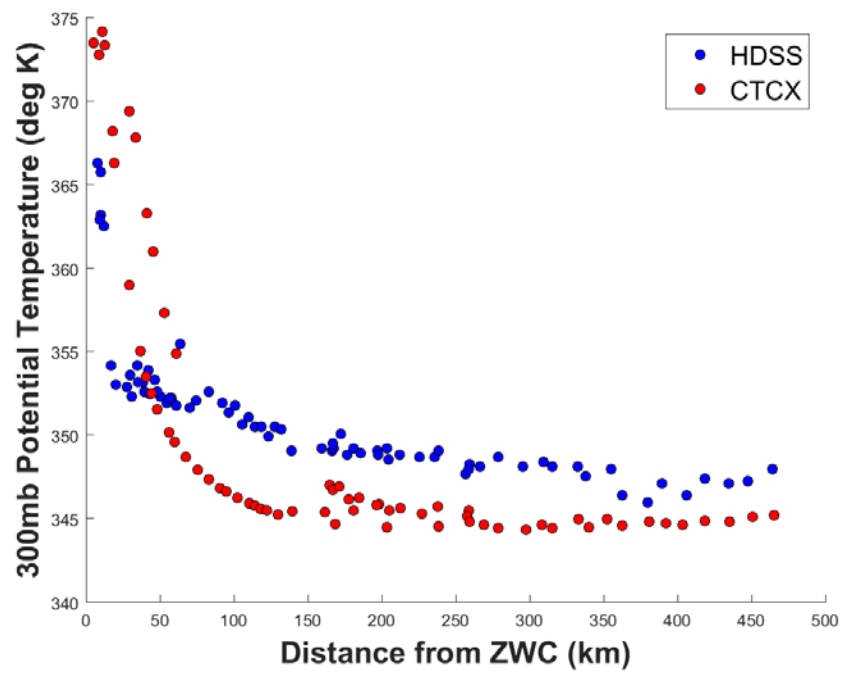


Figure 118. Potential temperatures as in Figure 95 except at 300 mb for 1800 UTC 23 October

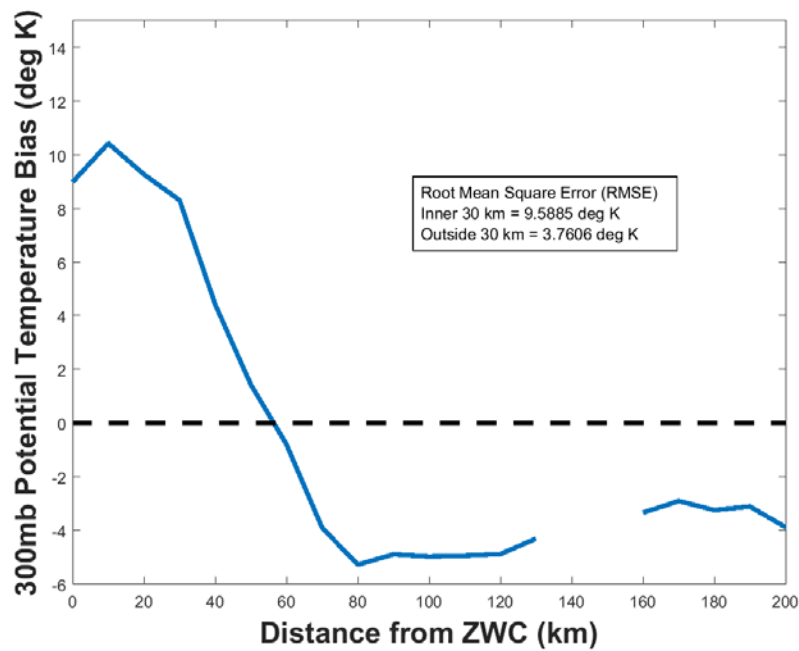


Figure 119. CTCX mean potential temperature bias as in Figure 96 except at 300 mb for 1800 UTC 23 October

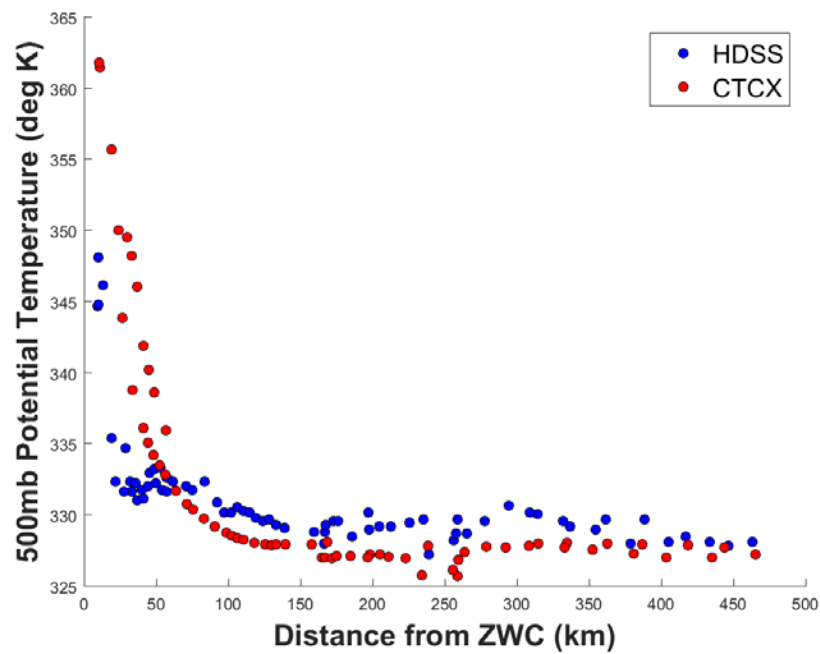


Figure 120. Potential temperatures as in Figure 95 except at 500 mb for 1800 UTC 23 October

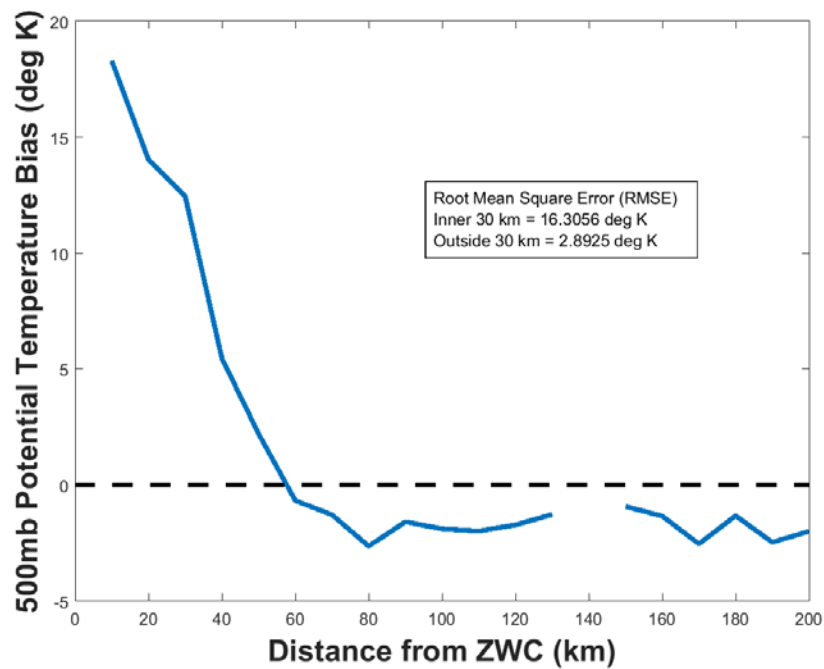


Figure 121. CTCX mean potential temperature bias as in Figure 96 except at 500 mb for 1800 UTC 23 October

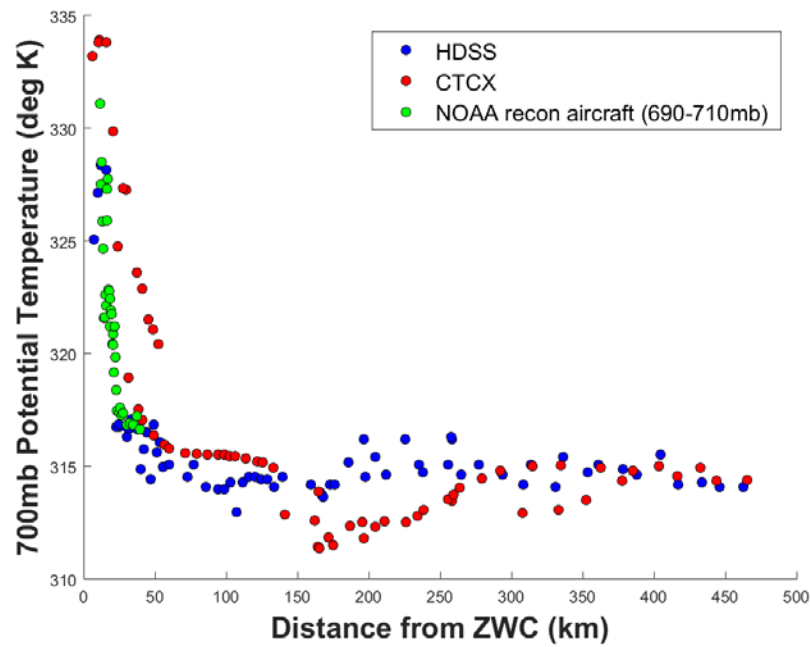


Figure 122. Potential temperatures as in Figure 95 except at 700 mb for 1800 UTC 23 October

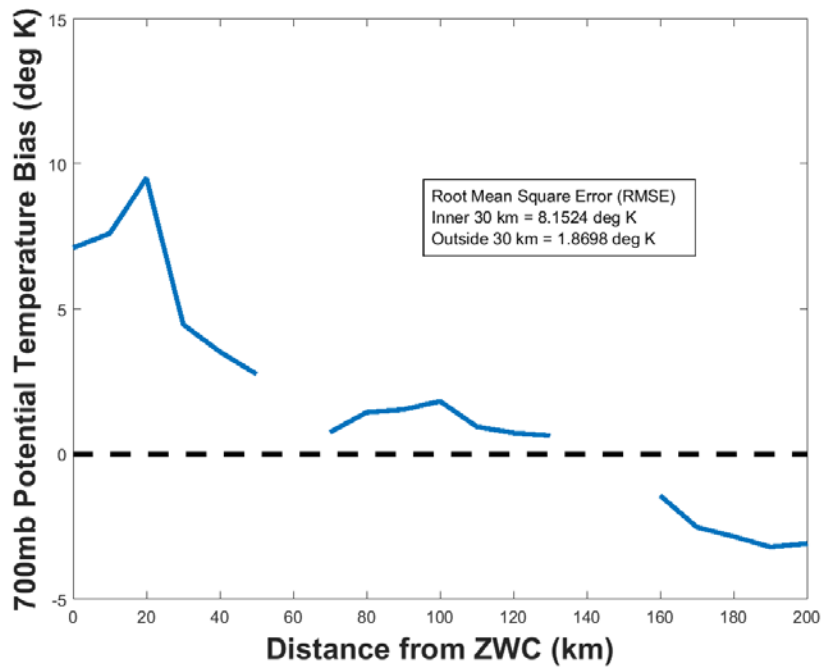


Figure 123. CTCX mean potential temperature bias as in Figure 96 except at 700 mb for 1800 UTC 23 October

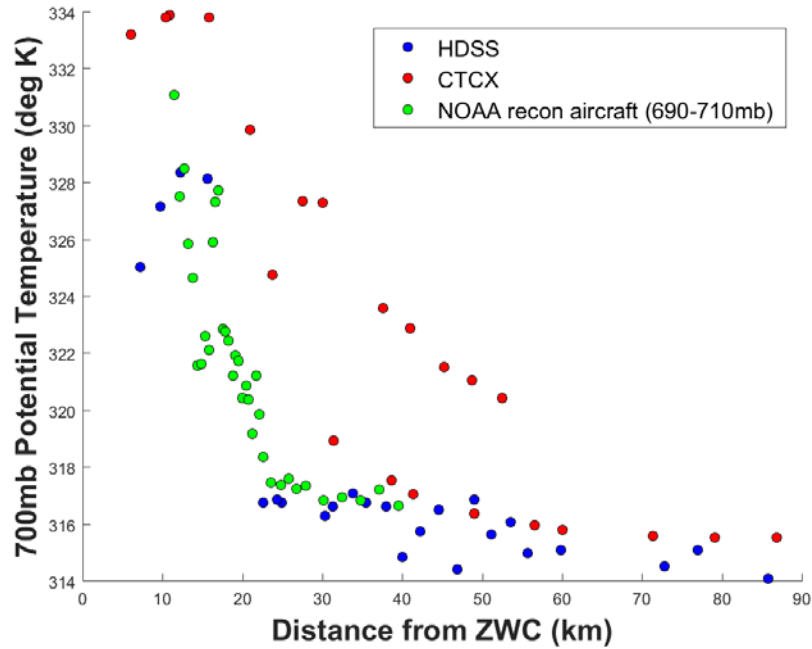
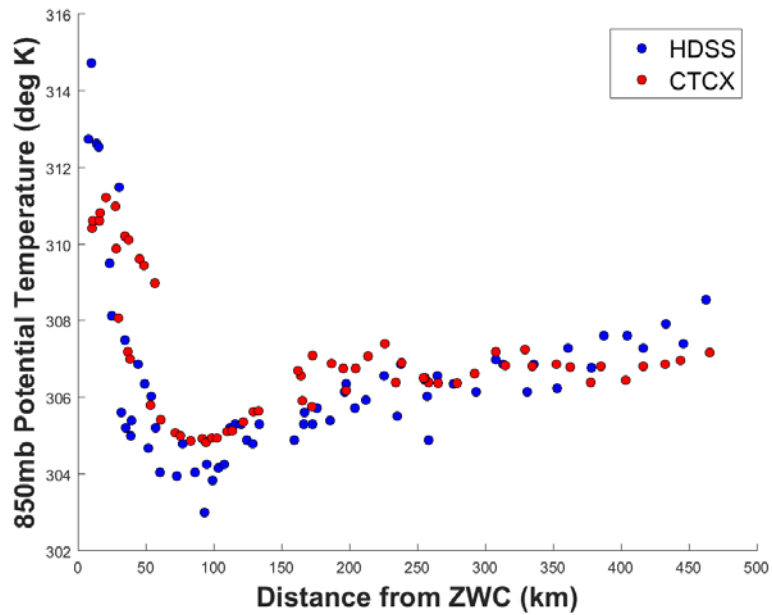


Figure 124. Potential temperatures as in Figure 95 except at 700 mb for 1800 UTC 23 October (zoomed to display only the inner 90 km)



Note the smaller Y-axis temperature increments relative to plots at the other pressure levels.

Figure 125. Potential temperatures as in Figure 95 except at 850 mb for 1800 UTC 23 October

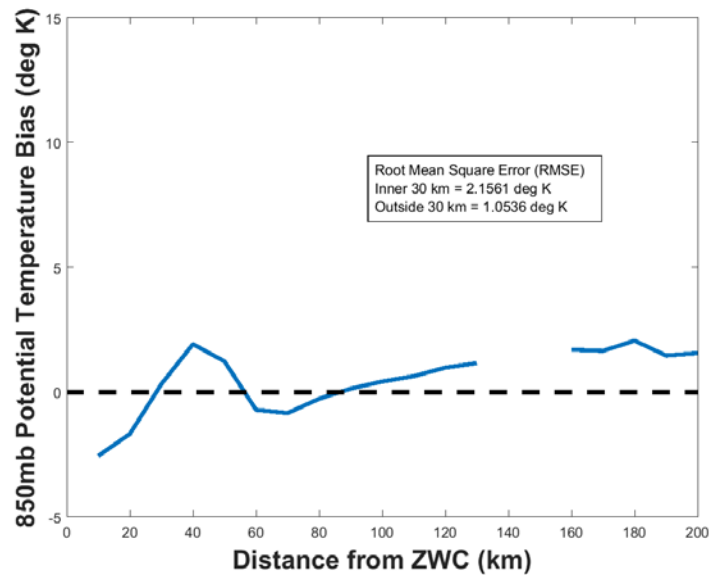


Figure 126. CTCX mean potential temperature bias as in Figure 96 except at 850 mb for 1800 UTC 23 October

At 1800 UTC 23 October the results are similar to those seen in the 22 October potential temperature comparisons. After subtracting the Jordan annual mean tropical potential temperature profile (Jordan, 1958), the HDSS observations indicate an elongated warm core anomaly from above 200 mb down to 700 mb, with the maximum of 22 K at 300 mb.

The CTCX initialization displays little bias at the 200 mb pressure level. However, moving down to 300 mb and 500 mb, the CTCX shows a strong positive bias from Patricia's center and past the eye-wall out to a radius of 60 km. Beyond 60 km, it then exhibits a negative bias. At the 700 mb inner core, the CTCX shows a positive bias similar to the 500 mb bias, but outside the core region the errors diminish. In the 850 mb comparison, the initial conditions in the CTCX and the HDSS observations are fairly coherent. Upon subtracting the Jordan annual mean profile, the CTCX depicts a warm core anomaly that is strongest at 500 mb (21 K), but does not extend up to 200 mb as the HDSS dropsondes observed.

The magnitude of the CTCX positive bias at 300 mb and especially 500 mb is significant. The HDSS observations reveal that the strongest warm core on 23 October is

at 300 mb, while the bogus vortex in the CTCX model has its warm core between near 500 mb.

E. ERROR SUMMARY AND ANALYSIS

Now that qualitative comparisons of Patricia's wind speed, potential temperature, and geopotential height radial plots have been conducted, this study will analyze a quantitative summary of the observed errors in the CTCX initial conditions at 1800 UTC from 21 to 23 October. Recall from section B.3 of this chapter that this study defines the inner core as three times the NHC RMW rounded to the nearest 10 km, resulting in radii of 160 km, 60 km, and 30 km for 21 October, 22 October, and 23 October, respectively. Also recall from the wind speed comparisons that the observed radius of maximum winds (RMW) slightly increased from 1800 UTC 22 October to 1800 UTC 23 October, whereas the NHC RMW decreased during the same time period. There is some sensitivity to this discrepancy in these error calculations. However, this study assumes that this inconsistency is not likely to change any conclusions drawn from the observed trends in error statistics from 22 October to 23 October.

1. Inner Core Region

First will be a summary of CTCX errors in the inner-core region (Tables 2–4). The summary of CTCX errors represents a vertical average across all five analyzed pressure levels. Equations for the error values are given in Chapter III.

Table 2. Inner 160 km CTCX error summary for 1800 UTC 21 October

Error	Potential Temperature (K)	Storm-Relative Wind Speed (m/s)	Geopotential Height (m)
ME	-2.4012	-7.5462	18.2616
MAE	2.5586	7.6381	28.2515
RMSE	2.6325	8.2366	32.5656

ME is the Mean Error. MAE is the Mean Absolute Error. RMSE is the Root Mean Square Error.

Table 3. Inner 60 km CTCX error summary for 1800 UTC 22 October

Error	Potential Temperature (K)	Storm-Relative Wind Speed (m/s)	Geopotential Height (m)
ME	4.7179	5.736	-171.7921
MAE	4.9963	15.9088	171.7921
RMSE	5.2011	18.2594	178.4161

ME is the Mean Error. MAE is the Mean Absolute Error. RMSE is the Root Mean Square Error.

Table 4. Inner 30 km CTCX error summary for 1800 UTC 23 October

Error	Potential Temperature (K)	Storm-Relative Wind Speed (m/s)	Geopotential Height (m)
ME	6.4946	5.0828	-220.2884
MAE	7.6802	21.2333	220.3016
RMSE	7.7973	24.0758	231.4558

ME is the Mean Error. MAE is the Mean Absolute Error. RMSE is the Root Mean Square Error.

Note the negative bias in potential temperature and wind speed, along with a positive bias in geopotential height, shown by the ME values from 21 October indicate the CTCX model was initialized too weak. After 21 October, these biases switch in sign, indicating that the CTCX initial conditions on 22 and 23 October describe a stronger core than observed by the HDSS dropsondes. However, the magnitude of these errors on 22 and 23 October is less significant than for 21 October when comparing their values to the intensity of Hurricane Patricia at all three times.

From 21 to 22 to 23 October, respectively, the CTCX initial condition RMSE values for potential temperature increase from 2.6325 K to 5.2011 K to 7.7973 K, RMSE values for storm-relative wind speed increase from 8.2366 m/s to 18.2594 m/s to 24.0758 m/s, and finally the RMSE values for geopotential height increase from 32.5656 m to 171.7921 m to 231.4558 m. This daily increase is expected due to the increase in potential temperature, wind speed, and geopotential height gradients as Patricia rapidly intensified from 21 to 23 October. Note that although the qualitative comparison of the inner-core structure between 22 and 23 October revealed that the CTCX bogus vortex structure was more accurate on 23 October than 22 October, the magnitude of the CTCX

bias is actually larger on 23 October. It is likely that there is some sensitivity in the error results to the objective definition of the inner core using NHC's RMW estimates.

2. Outer Region

Next is an examination of the CTCX error summary for the region outside of Patricia's core at 1800 UTC 21 to 23 October (Tables 5–7).

Table 5. CTCX error summary outside of a 160 km radius for 1800 UTC
21 October

Error	Potential Temperature (K)	Storm-Relative Wind Speed (m/s)	Geopotential Height (m)
ME	-2.4852	-5.0226	29.5447
MAE	2.513	5.3262	36.974
RMSE	2.5905	5.9561	42.6166

ME is the Mean Error. MAE is the Mean Absolute Error. RMSE is the Root Mean Square Error.

Table 6. CTCX error summary outside of a 60 km radius for 1800 UTC
22 October

Error	Potential Temperature (K)	Storm-Relative Wind Speed (m/s)	Geopotential Height (m)
ME	-0.6315	13.9191	-58.7652
MAE	1.6236	13.9798	72.9384
RMSE	2.0698	15.1036	86.4551

ME is the Mean Error. MAE is the Mean Absolute Error. RMSE is the Root Mean Square Error.

Table 7. CTCX error summary outside of a 30 km radius for 1800 UTC
23 October

Error	Potential Temperature (K)	Storm-Relative Wind Speed (m/s)	Geopotential Height (m)
ME	-1.3041	8.2179	-16.7271
MAE	2.3439	10.2397	54.5766
RMSE	2.7089	14.8108	77.1642

ME is the Mean Error. MAE is the Mean Absolute Error. RMSE is the Root Mean Square Error.

Unlike the inner-core region, the potential temperature mean bias indicated by the ME values never switch from negative values to positive values. However, the wind speed and geopotential height biases do switch sign between 21 and 22 October. This difference between the inner-core region and outer circulation is expected, as potential temperature and the warm core anomaly is solely a feature of the inner core in TCs.

From 21 to 22 to 23 October, respectively, the CTCX initial condition RMSE values for potential temperature vary from 2.5905 K to 2.0698 K to 2.7089 K, RMSE values for storm-relative wind speed vary from 5.9561 m/s to 15.1036 m/s to 14.8108 m/s, and finally the RMSE values for geopotential height vary from 42.6166 m to 86.4551 m to 77.1642 m.

As opposed to the inner-core region, CTCX errors in the outer region do not increase universally as Patricia rapidly intensified. The CTCX potential temperature bias is relatively constant, whereas there is a clear increase in the CTCX bias for the wind speed and geopotential height fields from 21 to 22 October. Then from 22 to 23 October, the errors CTCX wind and geopotential height slightly decrease. The increase in error from 21 to 22 October is expected as the overall TC strength intensifies. However, the 22 to 23 October decrease in error also occurred during intensification, and indicates that the CTCX model performed better in Patricia's outer region on 23 October despite the greater potential for error.

Also note that the CTCX errors in the outer circulation are generally smaller than the errors in the inner-core region for all days. Since the CTCX severely under-forecast Patricia's intensification, it is highly likely that the processes which created strong wind speed, geopotential height, and potential temperature gradients in Patricia's inner core structure were instrumental to the observed extreme rapid intensification.

THIS PAGE INTENTIONALLY LEFT BLANK

V. SUMMARY AND RECOMMENDATIONS

A. SUMMARY OF HURRICANE PATRICIA AS OBSERVED BY HDSS

Observations extending from the upper levels of the troposphere to the ocean surface are rarely available for TCs, and especially rare for rapidly intensifying hurricanes (Chen and Zhang, 2012). Therefore, the data collected in Patricia provides a valuable glimpse at the rapid intensification process. Between 1800 UTC 21 October and 1800 UTC 22 October, Patricia evolved from a typical Eastern Pacific Tropical Storm into an extremely small and intense Hurricane, with a compact eye-wall with a 10 to 15 km radius and a wind field that drastically diminished in its strength outside of the inner-core region. A strong warm core (13 K potential temperature anomaly) at 300 mb existed directly above the small eye. Patricia's structure at 1800 UTC 23 October was very similar to 22 October, but with an even more compact radius, stronger maximum winds, a larger wind speed gradient outside of the core, and a warmer core at 300 mb (22 K potential temperature anomaly). In order to improve future forecasts for rapidly intensifying TCs, understanding the processes that led to Patricia's small and intense structure will be vital.

B. CONCLUSIONS AND RECOMMENDATIONS

The evaluation of the comparisons between the CTCX initial conditions and observations reveals three significant conclusions.

The first conclusion is that the structure of the outflow layer in the CTCX initial conditions at 1800 UTC 22 and 23 October did not include the observed equatorward outflow jet. While the upper-level outflow layer is not a part of the initial bogus vortex and the GFS initial conditions are the primary cause for this discrepancy, it may have significantly impaired the ability of the CTCX to forecast Patricia's rapid intensification. This study recommends that further research be conducted to determine methods for including the outflow layer structure and linkage to storm secondary circulations in future CTCX bogus initializations.

Second, the bogus vortex inserted into the CTCX model initialized at 1800 UTC 21 October was too weak. The CTCX exhibited a negative bias in storm-relative wind speed at all levels, a negative bias in potential temperature from 200 mb down to 500 mb, and a positive bias in geopotential height from 700 mb down to 850 mb. The model was initialized at 1800 UTC based on NHC's 1500 UTC analysis of 35 kt maximum sustained winds. A reconnaissance mission did not conduct an over-pass of Tropical Storm Patricia until 2025 21 October, which revealed a Stepped Frequency Microwave Radiometer (SFMR) estimate of 50 kt maximum sustained winds (National Hurricane Center, 2017). Therefore the initial CTCX bogus vortex at 1800 UTC 21 October may have been too weak due to intensification that occurred between the 1500 UTC official analysis and the 1800 UTC model initialization time. The 1500 UTC analysis utilizing only satellite imagery and zero in-situ observations may have also contributed to the observed error. This study cannot provide a recommendation for this conclusion, other than more in-situ observations are required early in a TC's lifecycle in order for more accurate and timely analyses to be provided to CTCX.

The final conclusion obtained by examining the comparisons between observations and CTCX initial conditions is that the initial vortex in the CTCX model at 1800 UTC 22 October did not match Patricia's true structure. Patricia was undergoing rapid intensification at the CTCX initialization time and had developed an extremely compact eye with its strongest warm core anomaly near 300 mb and wind speeds that significantly decreased once outside of the inner-core region. However, the TC structure in the CTCX model depicted Patricia with a much less compact eye, its strongest warm core anomaly near 500 mb, and wind speeds that only slightly decreased outside of the inner-core region. At 1800 UTC 22 October, NHC's official analysis provided an eye-wall radius of 10 n mi (approximately 18.5 km; Kimberlain et al., 2016), which is larger than the 10 km indicated by the TCI field program's in-situ observations, but provided a much better estimate than the 50 km radius initialized in the CTCX model. However, it should be noted that the horizontal grid spacing of 5 km for the innermost nest of CTCX was too coarse to adequately represent the inner core. This study recommends that NHC's radius of maximum winds be given a heavier weight in the CTCX bogus vortex

initialization scheme. Also, smaller horizontal grid spacing of 1–2 km will ultimately be necessary in CTCX to resolve details of inner-core structure of future rapidly intensifying storms similar to Patricia. Finally, this conclusion illustrates the need for sophisticated data assimilation systems that can ingest high density observations instead of relying on the limited information provided by official TC forecasts to construct a balanced bogus vortex.

C. AREAS FOR FUTURE RESEARCH

Using the TCI data collected for Patricia, the CTCX bogus structure can be adjusted to match the observations at 1800 UTC for 21 and 22 October. Improvements need to be made to the RMW, radial decay of tangential winds, vertical structure of tangential winds, and warm core location. The model can then be re-run in order to discover if CTCX predicts rapid intensification with these improvements to the initial conditions.

This study observed specific characteristics of rapidly intensifying TC, such as a tight inner-core vortex and rapid radial decay of tangential velocity outside the RMW. Further research can be conducted to determine if these are standard characteristics of a rapidly intensifying TC and how vortex structure may pre-dispose a TC to experience rapid intensification. Further research is also needed on initializing vortices with secondary circulations (boundary layer inflow, upward motion, and upper-level outflow).

With a long-term goal of transitioning from bogus practices to utilizing TC-scale observations in future data assimilation systems, assimilation of new-generation satellite AMVs (high spatial and temporal resolution) should be researched in order for NWP models to include outflow jets in initial conditions. This is particularly important for TCs that exist far away coastal regions where no aircraft reconnaissance missions are available.

THIS PAGE INTENTIONALLY LEFT BLANK

LIST OF REFERENCES

- Bell, M.M., J. D. Doyle, M. Beaubien, T. Allen, B. R. Brown, J.P. Dunion, P. Duran, J. W. Feldmeier, L. C. Harrison, E. A. Hendricks, W. Jeffries, W. A. Komaromi, J. Martinez, J. Molinari, J. R. Moskaitis, D. P. Stern, and D. Vollaro, 2016: Tropical Cyclone Intensity (TCI), 2015: High Density Dropsonde Quality Assurance Summary. Sponsored by the Office of Naval Research.
- Black, P. G., L. Harrison, M. Beaubien, R. Bluth, R. Woods, A. Penny, R. W. Smith, and J. D. Doyle, 2017: High Definition Sounding System (HDSS) for atmospheric profiling, *Journal of Atmospheric and Oceanic Technology*, **34**, 777–796, doi: 10.1175/JTECH-D-14-00210.1.
- Braun, S. A., and coauthors, 2013: NASA’s Genesis and Rapid Intensification Processes (GRIP) Field Experiment. *Bull. Amer. Meteor. Soc.*, **94**, 345–363, doi: 10.1175/BAMS-D-11-00232.1.
- Braun, S. A., P. A. Newman, and G. M. Heymsfield, 2016: NASA’s Hurricane and Severe Storm Sentinel (HS3) Investigation. *Bull. Amer. Meteor. Soc.*, **97**, 2085–2102, doi: 10.1175/BAMS-D-15-00186.1.
- Brueske, K. F. and C. S. Velden, 2002: Satellite-Based Cyclone Intensity Estimation Using the NOAA-KLM Series Advanced Microwave Sounding Unit (AMSU). *Mon. Wea. Rev.*, **131**, 687–697, doi: 10.1175/1520-0493(2003)131<0687:SBTCIE>2.0.CO;2.
- Cecil, D. J., 2016: Hurricane Imaging Radiometer (HIRAD). [<https://airbornescience.nasa.gov/instrument/HIRAD>].
- Chen, H. and D. Zhang, 2012: On the Rapid Intensification of Hurricane Wilma (2005). Part II: Convective Bursts and the Upper-Level Warm Core. *J. Atmos. Sci.*, **70**, 146–162, doi: 10.1175/JAS-D-12-062.1.
- Creasey, R. L., and R. L. Elsberry, 2017: Tropical cyclone center positions from sequences of HDSS sondes deployed along high-altitude overpasses. *Wea. Forecasting*, **32**, 317–325, doi: 10.1175/WAF-D-16-0096.1.
- Cooperative Institute for Meteorological Satellite Studies (CIMSS), 2017: Tropical Cyclones: A Satellite Perspective, accessed 12 March 2017. [tropic.ssec.wisc.edu].
- Doyle, J. D., R.M. Hodur, S. Chen, Y. Jin, J. R. Moskaitis, S. Wang, E. A. Hendricks, H. Jin, and T. A. Smith, 2014: Tropical Cyclone Prediction Using COAMPS-TC. *Oceanography*, **27**(3), 104–115, doi: 10.5670/oceanog.2014.72.

- Doyle, J. D., R. Hodur, J. Moskaitis, S. Chen, P. Black, E. Hendricks, H. Jin, A. Reinecke, J. Schmidt, and S. Wang, 2015: Recent COAMPS-TC Development and Future Plans. 2015 Tropical Cyclone Research Forum, Jacksonville, FL. [<http://www.ofcm.gov/meetings/TCORF/ihc15/presentations/Session5b/>].
- Doyle, J. D. and coauthors, 2017: A View of Tropical Cyclones from Above: The Tropical Cyclone Intensity (TCI) Experiment. *Bull. Amer. Meteor. Soc.*, **In Press**, doi: 10.1175/BAMS-D-16-0055.1.
- Halverson, J. and coauthors, 2007: NASA's Tropical Cloud Systems and Processes Experiment: Investigating Tropical Cyclogenesis and Hurricane Intensity Change. *Bull. Amer. Meteor. Soc.*, **88**, 867–882, doi: 10.1175/BAMS-88-6-867.
- Hodur, R. M., 1997: The Naval Research Laboratory's Coupled Ocean/Atmosphere Mesoscale Prediction System (COAMPS). *Mon. Wea. Rev.*, **125**, 1414–1430, doi: 10.1175/1520-0493(1997)125<1414:TNRLSC>2.0.CO;2.
- Hendricks, E. A., M.S. Peng, B. Fu, and T. Li, 2010: Quantifying Environmental Control on Tropical Cyclone Intensity Change. *Mon. Wea. Rev.*, **138**, 3243–3271, doi: 10.1175/2010MWR3185.1.
- Hendricks, E.A. and M.S. Peng, 2012. Initialization of Tropical Cyclones in Numerical Prediction Systems, Advances in Hurricane Research. *Modelling, Meteorology, Preparedness and Impacts*, K. Hickey, Ed., InTech. [<https://www.intechopen.com/books/advances-in-hurricane-research-modelling-meteorology-preparedness-and-impacts/initialization-of-tropical-cyclones-in-numerical-prediction-systems>].
- Jin, Y., W. T. Thompson, S. Wang, and C. Liou, 2007: A Numerical Study of the Effect of Dissipative Heating on Tropical Cyclone Intensity. *Wea. Forecasting*, **22**, 950–966, doi: 10.1175/WAF1028.1.
- Jordan, C. L., 1958: Mean Soundings for the West Indies Area. *Journal of Meteorology*, **15**, 91–97, doi: 10.1175/1520-0469(1958)015<0091:MSFTWI>2.0.CO;2.
- Knaff, J.A. and R.M. Zehr, 2007: Reexamination of Tropical Cyclone Wind-Pressure Relationships. *Wea. Forecasting*, **22**, 71–88, doi: doi.org/10.1175/WAF965.1.
- Kaplan, J., and M. DeMaria, 2003: Large-scale Characteristics of Rapidly Intensifying Tropical Cyclones in the North Atlantic Basin. *Wea. Forecasting*, **18**, 1093–1108, doi:
- Kimberlain, T.B, E. S. Blake, and J. P. Cangialosi, 2016: National Hurricane Center Tropical Cyclone Report: Hurricane Patricia (EP202015). [http://www.nhc.noaa.gov/data/tcr/EP202015_Patricia.pdf]

- Komaromi, W. A. and J. D. Doyle, 2016: Tropical Cyclone Outflow and Warm Core Structure as Revealed by HS3 Dropsonde Data. *Mon. Wea. Rev.*, **145**, 1339–1359, doi: 10.1175/MWR-D-16-0172.1.
- Leroux, M., N. E. Davidson, Y. Ma, and J. D. Kepert, 2012: Prediction and Diagnosis of the Motion and Rapid Intensification of Typhoon Sinlaku during Tropical Cyclone Structure Experiment 2008 (TCS08). *Mon. Wea. Rev.*, **141**, 1413–1436, doi: 10.1175/MWR-D-11-00346.1.
- Liou, C.-S., and K.D. Sashegyi, 2012: On the Initialization of Tropical Cyclones with a Three-dimensional Variational Analysis. *Natural Hazards*, **63**(1), 1375–1391, doi: 10.1007/s11069-011-9838-0.
- Merrill, R. T., 1988: Characteristics of the Upper-tropospheric environmental flow around hurricanes. *J. Atmos. Sci.*, **45**, 1665–1677, doi: 10.1175/1520-0469(1988)045<1665:COTUTE>2.0.CO;2
- Montgomery, M. T. and Smith, Roger K., 2014: Paradigms for Tropical Cyclone Intensification. *Australian Meteorological and Oceanographic Journal*, **64**, 37–66, doi:
- National Hurricane Center, 2017: Hurricane Patricia Advisory Archive, accessed 20 April 2017. [<http://www.nhc.noaa.gov/archive/2015/PATRICIA.shtml?>].
- Naval Research Laboratory, 2017: 20E.Patricia Archive, accessed 25 April 2017. [<https://www.nrlmry.navy.mil/TC.html>].
- Rappin, E. D., M. C. Morgan, and G. J. Tripoli, 2011: The Impact of Outflow Environment on Tropical Cyclone Intensification and Structure. *J. Atmos. Sci.*, **68**, 177–194, doi: 10.1175/2009JAS2970.1.
- Rogers, R., S. Aberson, J. Kaplan, and S. Goldberg, 2001: A Pronounced Upper-Tropospheric Warm Anomaly Encountered by the NOAA G-IV Aircraft in the Vicinity of Deep Convection. *Mon. Wea. Rev.*, **130**, 180–187, doi: doi.org/10.1175/1520-0493(2002)130<0180:APUTWA>2.0.CO;2.
- Rogers, R. and coauthors, 2006: The Intensity Forecasting Experiment. *Bull. Amer. Meteor. Soc.*, **94**, 859–882, doi: 10.1175/BAMS-87-11-1523.
- Rogers, R. F., S. Aberson, M. M. Bell, D. J. Cecil, J. D. Doyle, T. B. Kimberlain, J. Morgerman, L. K. Shay, and C. Velden, 2017: Re-Writing the Tropical Record Books: The Extraordinary Intensification of Hurricane Patricia (2015). *Bull. Amer. Meteor. Soc.*, **In Press**, doi:10.1175/BAMS-D-16-0039.1.
- Stern, P. S. and D. S. Nolan, 2011: On the Vertical Decay Rate of the Maximum Tangential Winds in Tropical Cyclones. *J. Atmos. Sci.*, **68**, 2073–2094, doi: 10.1175/2011JAS3682.1.

- Stern, P.S. and D.S. Nolan, 2012: On the Height of the Warm Core in Tropical Cyclones. *J. Atmos. Sci.*, **69**, 1657–1680, doi: 10.1175/JAS-D-11-010.1.
- Uhlhorn, E. W., P. G. Black, J. L. Franklin, M. Goodberlet, J. Carswell, and A. S. Goldstein: 2007: Hurricane Surface Wind Measurements from an Operational Stepped Frequency Microwave Radiometer. *Mon. Wea. Rev.*, **135**, 3070–3085, doi: 10.1175/MWR3454.1.
- United States Department of Commerce, 2017: National Hurricane Operations Plan, accessed 25 April 2017. [<http://www.ofcm.gov/publications/nhop/nhop2.htm>].
- Wang, Y., 2002: An Explicit Simulation of Tropical Cyclones with a Triply Nested Movable Mesh Primitive Equation Model: TCM3. Part II: Model Refinements and Sensitivity to Cloud Microphysics Parameterization. *Mon. Wea. Rev.*, **130**, 3022–3036, doi: 10.1175/1520-0493(2002)130<3022:AESOTC>2.0.CO;2.
- Willoughby, H.E., and M.B. Chelmow, 1982: Objective Determination of Hurricane Tracks from Aircraft Observations. *Mon. Wea. Rev.*, **110**, 1298–1305, doi: 10.1175/1520-0493(1982)110<1298:ODOHTF>2.0.CO;2.
- Willoughby, H.E., 1990: Gradient Balance in Tropical Cyclones. *Notes and Correspondence*, **47**(2), 265–274, doi: 10.1175/1520-0469(1990)047<0265:GBITC>2.0.CO;2.
- Willoughby, H.E., R.W.R. Darling, and M.E. Rahn, 2006: Parametric Representation of the Primary Hurricane Vortex. Part II: A New Family of Sectionally Continuous Profiles. *Mon. Wea. Rev.*, **134**, 1102–1120, doi: 10.1175/MWR3106.1.

INITIAL DISTRIBUTION LIST

1. Defense Technical Information Center
Ft. Belvoir, Virginia
2. Dudley Knox Library
Naval Postgraduate School
Monterey, California